PHASE-ENCODED MRI

FOR GEOMETRICALLY UNDISTORTED IMAGING

AND SIGNAL CHARACTERIZATION

FASEGECODEERDE MRI VOOR GEOMETRISCH ONVERSTOORDE

BEELDVORMING EN SIGNAALKARAKTERISERING

(met een samenvatting in het Nederlands)

PROEFSCHRIFT

ter verkrijging van de graad van doctor aan de Universiteit Utrecht op gezag
van de rector magnificus, prof. dr. G.J. van der Zwaan, ingevolge het besluit
van het college voor promoties in het openbaar te verdedigen op
dinsdag 21 juni 2016 des middags te 4.15 uur

door

JETSE SIGIWARD VAN GORP

geboren op 18 augustus 1985
te Eindhoven

Promotor: Prof. dr. ir. M.A. Viergever

Copromotor: Dr. ir. P.R. Seevinck

CONTENTS

INTRODUCTION

1.1 GENERAL INTRODUCTION

In the last decades Magnetic Resonance Imaging (MRI) has greatly improved the possibilities for non-invasive diagnosis of disease. MRI has earned its place in the clinical decision making process due to its excellent soft-tissue contrast, the lack of radiation and the possibility to measure a wide range of physiological properties (i.e. diffusion, perfusion, metabolism, oxygenation). In recent years the development of high-field strength scanners, improved transmit-receive systems, new acquisition strategies and increased computational power have further improved the diagnostic capabilities of MRI.

Many of these developments have focused on improving the imaging efficiency, due to the limited available scan time for clinical protocols. In MRI sequence design, a trade-off has to be made between image quality and scan time, which is related to the process of spatial encoding. Adjusting the sampling schemes to the clinical research question often results in an efficient method with sufficient image quality to answer the questions at hand. If for example, we would like to detect microbleeds in the brain, it is essential that we acquire images of the brain with the highest possible resolution, while a functional study of the heart would require multiple images within a single heartbeat to assess its function. In both these examples fast and efficient sampling schemes are necessary to acquire sufficient spatial or dynamic resolution.

These efficient MRI methods require a homogeneous magnetic field (B_0) and linear spatial encoding gradients (G_x, G_y, G_z) for accurate spatial encoding of the MR signal. In practice, however, many variations in the magnetic field can exist, such as differences in the chemical environment (e.g. chemical shift), magnetic susceptibility effects (e.g. air-tissue interfaces, metal prostheses) or system imperfections (e.g. inhomogeneous B_0, non-linear gradients). In conventional MRI methods these field inhomogeneities result in severe image distortions, such as geometrical distortions, signal voids and signal hyperintensities. In this thesis, the goal was to develop MRI methods for geometrically undistorted imaging and accurate signal characterization in the presence of field inhomogeneities and chemical shift. MRI techniques with these properties are so-called fully phase-encoded sequences that have been used extensively in the laboratory setting for solid state imaging and for pre-clinical investigations. The main disadvantage of phase-encoded MRI is the long scan time requirement, which has prevented adaptation in the clinic. In this thesis, phase-encoded sequences were used to address existing challenges on clinical MRI systems, where the excellent data quality might outweigh the scan time limitations (i.e. imaging near metal, low sensitivity, accurate signal characterization).

In this introduction a step-by-step explanation is given of important concepts in MRI (i.e. signal formation, spatial encoding, magnetic susceptibility, chemical shift) that are relevant for the investigated research topics, followed by a thesis outline.

1.2 MR SIGNAL FORMATION

The signal in a MR experiment originates from the magnetic properties of non-zero spin nuclei (1,2), such as proton, sodium and fluorine nuclei that were studied in this thesis. In the case of spin ½ nuclei (i.e. proton and fluorine) a net magnetic moment originates from an energy difference between two energy states, where the difference between the two energy levels can be described by:

$$\Delta E = \gamma \left(\frac{h}{2\pi}\right) B_0 \qquad [1.1]$$

with γ the gyromagnetic ratio of the nucleus, h is Planck's constant and B_0 is the main magnetic field. Eq 1.1 can also be written as:

$$\Delta E = h\, v_0 \qquad [1.2]$$

where v_0 is the Larmor frequency, which is the precession frequency where the resonance condition for MR excitation is fulfilled:

$$v_0 = \frac{\gamma}{2\pi} B_0 \qquad [1.3]$$

After placing an ensemble of non-zero spin nuclei in a strong magnetic field the population difference between the two energy states increases according to the Boltzmann equation, causing an increase in the net magnetic moment. This net magnetic moment is the sum of all individual magnetic moments and is often described as a magnetization vector, which can be used to describe most of the MR signal behavior using classical physics (3,4) instead of quantum mechanics (5). The net magnetization vector is oriented parallel with B_0 where the amplitude in thermal equilibrium is given by:

$$M_0 = \left(\frac{\gamma h}{2\pi}\right)^2 \frac{n B_0}{4kT} \qquad [1.4]$$

where n is the total number of spins in the ensemble, k is the Boltzmann constant and T is the absolute temperature. From Eq 4 it can be seen that the observable magnetization vector M_0 increases quadratic with the gyromagnetic ratio and linearly with B_0, which implies a higher SNR for high gyromagnetic ratios and higher field strengths, respectively. This relation also explains the trend towards higher field strengths for human MRI systems in recent years, which has improved the applicability for i.e. spectroscopy and non-proton MRI investigations that have traditionally been impeded by low sensitivity. Before a MR signal can be detected the magnetization vector M_0 has to be rotated to the plane perpendicular to B_0, known as the transverse plane.

This rotation is achieved by applying a second magnetic field B_1 perpendicular to the main magnetic field B_0, with the same precession frequency (Eq 1.3) as the net magnetic moment. This process is referred to as rf excitation. After the rotation of the net magnetic moment

M_0 from the z axis towards the x-y plane the precession of the transverse components of M_0 through a receive coil will create a loop current. This current translates to the MR signal, which can be described using complex numbers.

To simplify the description of the behavior of the magnetization vector through time the x, y and z world coordinates are replaced by x', y' and z' coordinates that rotate around B_0 with the Larmor frequency. Conventionally the x, y and z coordinates in MR signal equations refer to the x', y' and z' rotating frame of reference instead of Cartesian coordinates. From this point we will also refer to the rotating frame of reference when using x, y and z. The behavior of the x, y and z components of the magnetization vector through time can be described by the Bloch equations. For the simple case without B_0 inhomogeneities after B_1 excitation the Bloch equations for the magnetization in the rotating frame of reference are given by:

$$\frac{dM_x}{dt} = -\frac{M_x}{T_2}$$ [1.5]

$$\frac{dM_y}{dt} = -\frac{M_y}{T_2}$$ [1.6]

$$\frac{dM_z}{dt} = -\frac{M_z - M_0}{T_1}$$ [1.7]

where $M_{x,y,z}$ are the individual magnetization vectors in each spatial direction, T_2 is the transversal relaxation time and T_1 is the longitudinal relaxation time, which influence the size of the magnetization vector and therefore the available signal present in a MR experiment.

1.3 T_1 AND T_2 RELAXATION

T_1 and T_2 relaxation originate from interactions between nuclear magnetic spins and with their environment. The relaxation times vary substantially between biological tissues and metabolites, which can provide useful information for the detection of disease (6). An example is given (Figure 1.1) for three different tissues that are encountered when imaging the knee (Fat, Muscle, Tendon). The available signal in the transversal plane (M_{xy}) decreases exponentially over time for all tissue types with different T_2 relaxation rates. If data is acquired 20 ms after excitation the signal of the tendons has almost disappeared, while fat and muscle show similar signal amplitudes. However, when acquiring data 1 ms after excitation the tendons will contribute almost equally to the total measured magnetization. When repeating the experiment after a certain time the maximum signal that can be excited is determined by the longitudinal T_1 relaxation (Figure 1.1b). It can be seen that the difference in T_1 relaxation between muscle and fat is more pronounced than the T_2 relaxation. The differences in relaxation behavior are used in clinical practice to weight the signal in the images according to T_1 and T_2 parameters, to achieve the desired soft-tissue

contrast for anatomical imaging and/or disease detection. However, in relaxation weighted imaging the contrast between healthy and diseased tissue may be low when the disease is still in an early stage or when it is diffuse throughout the tissue (i.e. osteoarthritis, myocardial infarction)(7,8). In such cases quantitative mapping of the relaxation parameters might be preferable to detect alterations in diseased tissue, despite the low contrast in relaxation weighted images.
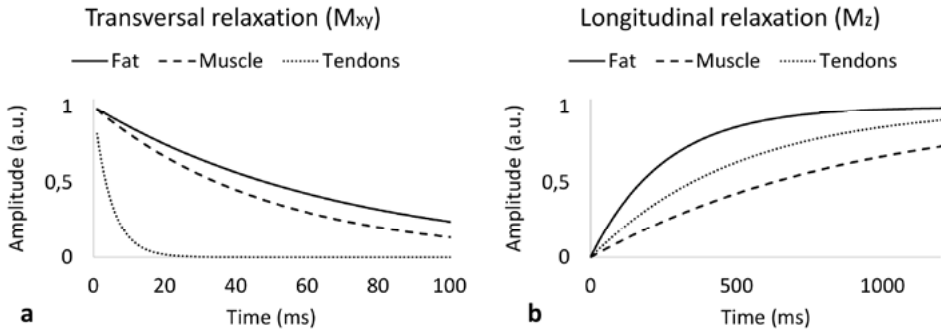

Figure 1.1: Transversal (T_2) relaxation (a) and longitudinal (T_1) relaxation (b) for different biological tissues after full excitation of the MR signal. The transversal magnetization M_{xy} is the measured signal after excitation and the longitudinal magnetization M_z is the available magnetization for the following repetition of the MR experiment.

1.4 MR IMAGING

To obtain MR images the MR signal is modified locally using magnetic field gradients (9,10). The application of a magnetic field gradient that linearly varies with the position in an object leads to a spatial dependency of the magnetic field with respect to the location:

$$B(x) = B_0 + x\,G_x \qquad [1.8]$$

with G_x the gradient strength and x the position in 1 dimension. The varying magnetic field will also lead to a spatially varying resonance condition:

$$\omega(x) = \gamma B_0 + \gamma\,x\,G_x \qquad [1.9]$$

To be able to retrieve the spatial information from all combined frequencies present in the object numerous data points with varying phase accumulation are required. These data points are referred to as k-space coordinates (or frequency space) in MRI and the signal can be described with:

$$s(k) = \int \rho(x)e^{-i\,2\pi kx}dx \qquad [1.10]$$

with k the step size in k-space defined as $(\gamma/2\pi)G_x$ t, with t defined as the time that the gradient has been turned on and $\rho(x)$ the effective 1D proton density that includes relaxation behavior and other factors.

1.4.1 FREQUENCY AND PHASE ENCODING

The spin distribution in the excited volume can be spatially encoded by applying gradients in 1, 2 or 3 dimensions of interest after signal excitation. The k-space coordinates (k = $(\gamma/2\pi)$ G_x t) can either be acquired during the application of a constant gradient (constant G_x with varying t) or by applying a gradient for a constant time followed by data acquisition (varying G_x with constant t). The first process is known as frequency encoding (Figure 1.2a) and the second is known as phase encoding (Figure 1.2b). In the frequency encoding process multiple k-space coordinates can be measured in a single acquisition, while the phase encoding process requires multiple repetitions to cover the same part of k-space. This makes phase-encoded imaging a slow process that is less efficient than frequency-encoded imaging in many clinical situations. This is the major limitation of phase-encoded imaging that has to be considered when competing with other MR imaging methods.
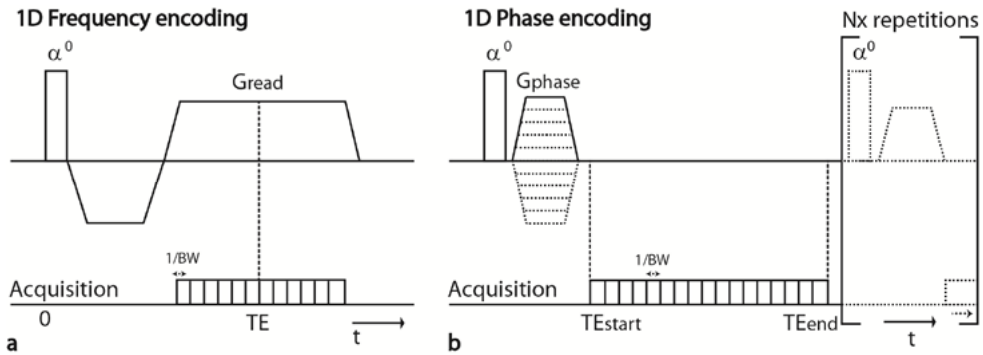

Figure 1.2: A 1D MR imaging experiment using either frequency encoding (a) or phase encoding (b) gradients. In a 1D experiment the frequency encoding acquisition is performed once to obtain a single image at a specific TE. The phase-encoded experiment is repeated N_x times to obtain a multitude of images with slightly varying TE's.

In a typical gradient echo frequency encoding experiment, first a negative gradient with half the area of the final readout gradient is switched on to obtain symmetrical sampling around the center of k-space. When the readout gradient is switched on the net induced phase is 0 at the center of k-space causing the formation of an echo. This time is called the echo time (TE) and is an important parameter in MR imaging because it is the dominant factor in the determination of the contrast of the image. In case of phase encoding there is no net gradient during the data readout, which is less efficient with respect to spatial encoding. To fully encode the x dimension N_x repetitions are required instead of a single repetition, with N_x the number of required points in the x dimension. However, despite this major disadvantage the separation of the acquisition window from the spatial encoding process leads to advantages with respect to temporally resolved MRI signal, image quality (sect 1.5) and sensitivity (sect 1.6), aspects which are explored in this thesis. The first major difference

12

between both encoding strategies is the effect of the TE and T_2 on the MR signal, which can be described by extending Eq 1.10 to include an exponential factor that describes the T_2 relaxation decay. The use of rectangular gradients is assumed in these equations.

For a 1D frequency encoded experiment Eq 1.10 becomes:

$$s(k) = \int \rho(x) e^{-i\, 2\pi kx} e^{\frac{-TE + p_x \tau}{T_2(x)}} dx \qquad [1.11]$$

with $k = \frac{\gamma}{2\pi} G_{read,x}\, \tau\, p_x$ with $G_{read,x}$ the constant strength of the readout gradient, τ the time per measurement point (1/bandwidth (BW)) and p_x the p-th sample of the signal readout defined as $-N_x/2 \le p_x \le N_x/2$ with Nx the number of samples. Here, the acquired k-space signal changes due to T_2 relaxation during the readout of the k-space line, which acts as a filter that causes blurring and imposes a lower limit on the spatial resolution. However, this effect is only pronounced for very short T_2 values or very long readout durations.

For a 1D phase-encoded experiment Eq 1.10 becomes:

$$s(k) = \int \rho(x) e^{-i\, 2\pi kx} e^{\frac{-TE + n_t \tau}{T_2(x)}} dx \qquad [1.12]$$

with $k = \frac{\gamma}{2\pi} \Delta G_{phase,x}\, t_p\, p_x$ with $\Delta G_{phase,x}$ the step-size of the phase encoding gradient, t_p the fixed time of the phase encoding gradient and p_x the p-th sample of the acquired k-space data with $-N_x/2 \le p_x \le N_x/2$. The effective TE is defined as $TE(n_t)=TE(1)+n_t\tau$ with TE(1) the echo time of the first time point, n_t the n-th acquired time point during the acquisition interval and τ the time per measurement point. This results in a series of time points where the relaxation term is independent of the spatial encoding term. Therefore, the signal can be used to directly study the relaxation behavior, frequency differences between biological compounds (sect 1.5.4) or retrospectively adjust the bandwidth by averaging multiple time points (sect 1.6). After acquisition of the full k-space data using either frequency or phase encoding a Fourier transformation can be applied (11) to obtain spatially resolved clinical images (10).

The presented 1D sequences and equations can be easily expanded to describe 3D spatial encoding. In the majority of clinical 3D MRI sequences two spatial dimensions are encoded using phase encoding, thereby increasing the acquisition time a factor N_yN_z.

1.4.2 SLICE SELECTION

In clinical practice the 3D volume of interest is often divided in a 2D slices, by a process called slice selection (Figure 1.3). This is achieved by applying a gradient during the excitation pulse (G_z) with a specific frequency range ($\Delta\omega$) and frequency offset (f_0). Only the region that fulfills the MR resonance condition ($z_0 \pm 0.5\Delta z$) will be excited by the excitation pulse and therefore measured in the MRI experiment. This center of the excited slice (z_0)

with respect to the isocenter of the magnet and the slice thickness (Δz) for on-resonance spins are described by:

$$z_0 = \frac{2\pi}{\gamma G_z} \Delta\omega \qquad\qquad [1.13]$$

and

$$\Delta z = \frac{2\pi}{\gamma G_z} \; \Delta\omega \qquad\qquad [1.14]$$

Slice excitation is often repeated multiple times with different frequency offsets to obtain information of multiple slices in the anatomic region of interest. The process of slice excitation is illustrated schematically below:
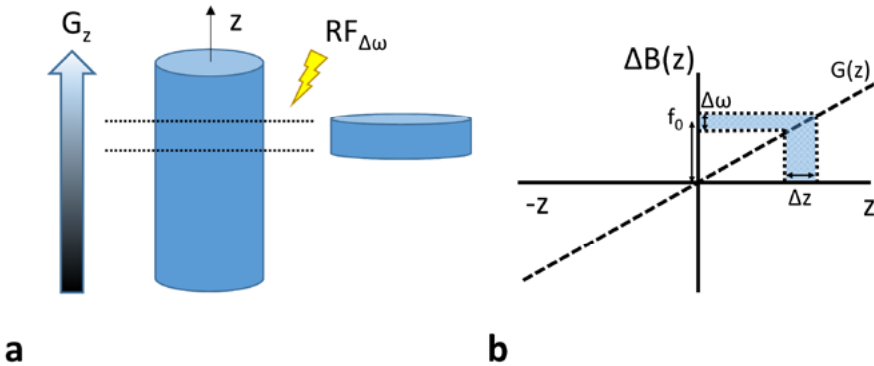

Figure 1.3: The slice selection in an MR imaging experiment using gradients during excitation is illustrated schematically in (a) showing the gradient, object and selected slice. The same process is shown in (b) as a function of the position z and the induced field offset ΔB(z) caused by the slice selection gradient G(z). The final excited slice Δz is determined by the excitation bandwidth Δω and the resonance offset frequency f_0.

1.5 MRI IN THE PRESENCE OF FIELD INHOMOGENEITIES

In the previous sections the main magnetic field B_0 was assumed to be perfectly homogeneous, which leads to perfect spatial localization in conventional frequency-encoded MRI sequences. In practice, however, substantial field deviations can be present due to imperfections in the magnetic field, non-linearities in the encoding gradients, differences in magnetic properties of tissues or implant material (e.g. magnetic susceptibility) and differences in the resonance frequency of metabolites (e.g chemical shift). In this section the impact of magnetic susceptibility differences and chemical shift on the spatial encoding and signal decay will be discussed to gain an understanding of the underlying causes of MR image distortions, and the potential solutions that are proposed in this thesis.

1.5.1 MAGNETIC SUSCEPTIBILITY

Magnetic susceptibility (χ) is a property of materials representing the tendency of a material to become magnetized when placed in an external magnetic field. In most applications this effect is minor and therefore not considered as an important property of the materials. However, in MRI the applied magnetic fields are very strong, making the χ of a chosen material considerably more important (12). In MRI, χ-effects are a source of image artifacts, decreased spatial accuracy and safety concerns due to the induced magnetic forces and electric conductivity of implanted devices. External devices are common in the field of orthopedics and MRI guided interventions where the χ of the material has to be taken into consideration. Materials that experience strong magnetic torque in a MRI scanner are considered incompatible (i.e. iron, steel), due to safety issues. Other metallic materials that are often used in orthopedic and spinal implants can include MR compatible stainless steel, cobalt-chromium alloys and titanium. These materials are often regarded MR compatible with respect to safety, but induce significant field inhomogeneities that cause image artifacts. Note that the safety of an implant is dependent on its composition, size and the applied magnetic field, which have to be taken into consideration before MRI investigations can be conducted. For more information on MRI compatibility a database of devices can be consulted (www.MRIsafety.com). In addition to external implanted devices, more modest dχ differences can exist within biological tissue (i.e. air-tissue interfaces, small iron deposits in the brain, calcifications) that can also be exploited as a base for image contrast (13). In this thesis a fundamental solution for imaging in the presence of extreme dχ gradients was explored to address unmet medical needs for post-operative orthopedic imaging.

1.5.2 CHEMICAL SHIFT

In addition to macroscopic field effects, the spin nucleus can interact on the molecular level with surrounding nuclear spins, which can cause shifts in the resonance frequency v_0 (14). The electrons in a molecule can shield the spin nucleus from the main magnetic field, causing a lower effective magnetic field $B_{local} = B_0(1-\sigma)$ where σ is a shielding constant that depends on the environment. The new resonance frequency v_{local} can be calculated by substituting B_{local} for B_0 in Eq 1.3. The difference between the on-resonance Larmor frequency v_0 and shielded frequency v_{local} is referred to as the chemical shift:

$$\delta = \frac{v_{local} - v_0}{v_0} 10^6 \qquad [1.15]$$

The chemical shift δ is expressed in parts per million (ppm) to enable direct comparisons between the resonance frequencies at different field strengths. This enables an easy comparison between studies where resonances are located at specific ppm values. In frequency-encoded imaging the differences in chemical shift causes a relative shift of the two chemical shift species in a medical image, which is known as the chemical shift artifact.

In this case the chemical shift is a problem. In phase-encoded imaging, where the encoding gradient is separated from the acquisition interval, the chemical shift artifact is prevented. More interestingly, it is possible to spectrally resolve the different chemical shift values to study the molecular environment, which is the basis of the field of MR spectroscopy (4). MR spectroscopy can be used to study underlying molecular pathways of diseases that may help to find potential diagnostic biomarkers (i.e. neurotransmitter concentrations, cancer metabolism rates)(15-18) or perform chemotherapy monitoring as was done in this thesis.

1.5.3 THE INFLUENCE OF FIELD INHOMOGENEITIES ON FREQUENCY AND PHASE ENCODING

The influence of dχ and chemical shift induced field offsets (ΔB) can be described by an additional term in the MRI signal equations. The field offset causes an additional phase development over time that impacts the image quality and MR signal behavior.

In the case of the 1D frequency encoding Eq 1.11 becomes:

$$s(k) = \int \rho(x)e^{-i\,2\pi kx}e^{\frac{-TE+p_x\tau}{T_2(x)}}e^{-i\gamma\Delta B(x)p_x\tau}dx$$

$$= \int \rho(x)e^{-i\,2\pi k\left(x+\frac{\Delta B(x)}{G}\right)}e^{\frac{-TE+p_x\tau}{T_2(x)}}dx \qquad [1.16]$$

In the frequency-encoded signal the influence of ΔB(x) is scaled with the k-space coordinate number. The scaling of the field induced phase offset during the readout gradient has implications for the geometrical accuracy in the reconstructed image (3). From the Fourier shift theorem it can be derived that the spin density at location x is reconstructed at location x' in the presence of a field offset according to:

$$\rho(x') = \rho\left(x - \frac{\Delta B(x)}{G_{read,x}}\right) \qquad [1.17]$$

Similar processes influence the slice selection procedure (Figure 1.4a) where a resonance offset causes a shift of the selected slice locations (Figure 1.4b). The range of excited spins is described by:

$$z_0 - \frac{\Delta z}{2} < z' < z_0 + \frac{\Delta z}{2} \qquad [1.18]$$

with

$$z' = z + \frac{2\pi}{\gamma G_s}\Delta B_0(z) \qquad [1.19]$$

where z' is the excited location in the presence of field inhomogeneities, which is shifted compared to the original location z.

In the case of dχ induced gradients during slice selection (Figure 1.4c) local thinning or thickening of the slice profile can occur in addition to a shift of the center of the slice, due

to variations in the frequency range in each location. In the readout direction, the local field gradients cause signal from multiple x locations to be mapped to a single location x'. This can cause signal hyperintensities on location x' and signal voids on the original x locations (Figure 1.4d). These effects are especially pronounced in the case of strong dχ effects, such as in the presence orthopedic implants (19).
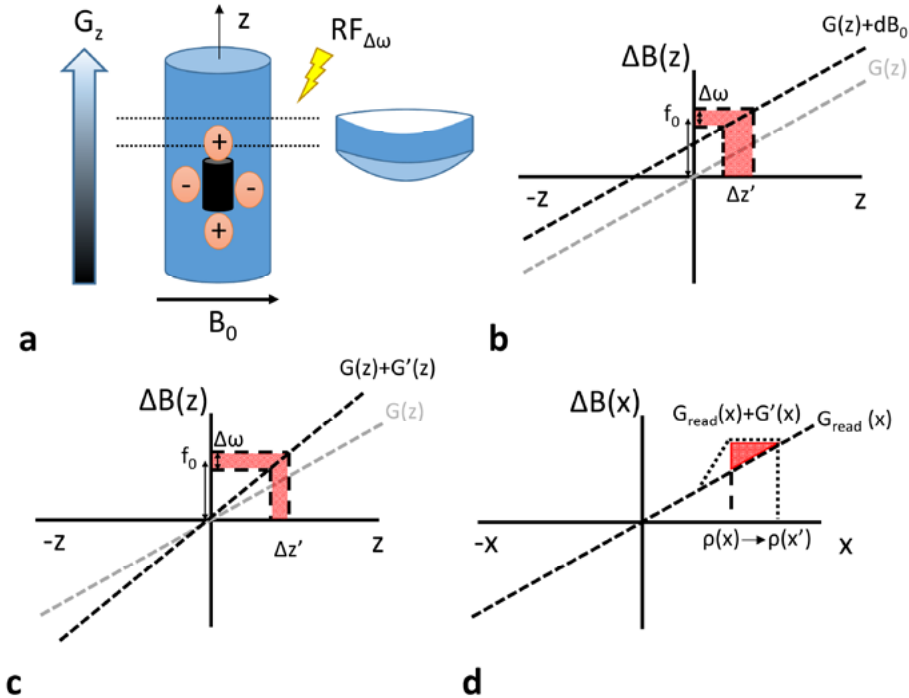

Figure 1.4: Schematic representation of slice (a-c) and frequency encoding distortions (d) due the susceptibility differences. After placing a cylinder with a susceptibility perpendicular to B_0 field inhomogeneities will be present. A constant offset in the frequency will cause a shift in the selected slice location (b), while additional field gradients will cause thinning or thickening of the slice (c). A local field gradient in the frequency encoding direction leads to a shift of the signal (d). All x locations under the red area will be mapped to x' causing signal hyper-intensities and signal voids.

For the case of 1D phase encoding Eq 1.12 becomes:

$$s(k) = \int \rho(x) e^{-i\,2\pi k x} e^{\frac{-TE+n_t\Delta t}{T_2(x)}} e^{-i\gamma\Delta B(x)n_t\Delta t} dx \qquad [1.20]$$

It can be seen that in the 1D phase-encoded experiment the inhomogeneity induced term is independent of the k-space coordinates and contributes equally to each measurement point in time, after phase encoding of the signal. By disentangling the field inhomogeneity induced phase term from the spatial encoding term it is possible to reconstruct geometrically undistorted images at multiple time points.

The 1D phase-encoded experiment described in the previous sections is known as chemical shift imaging or spectroscopic imaging (20), because the spatially localized signal can also be used to spectrally resolve metabolites with a different chemical shift. A Fourier transformation of the measured decay curve (e.g free induction decay) yields a frequency spectrum (Figure 1.5a), showing the dominant frequencies in the signal. The spatial encoding of the signal is not affected by chemical shift differences in the phase encoding directions. Instead of causing a shift in the spatial position, a modulation of the time signal is present, due to the presence of the different frequencies. In the spectral domain the different frequencies can be easily separated from each other (Figure 1.5b). In a spectroscopic investigation the detected frequencies can be used to differentiate between metabolites *in vivo* to non-invasively study the biochemistry (21). Therefore, the chemical shift property is actually a useful property in spectroscopic imaging, while it is often seen as an artifact in frequency-encoded imaging. However, the presence of ΔB_0 inhomogeneities caused by macroscopic dχ gradients is also regarded disadvantageous in spectroscopic imaging, because ΔB_0 effects decrease the peak amplitude and the spectral resolution, due to peak broadening (Figure 1.5c).
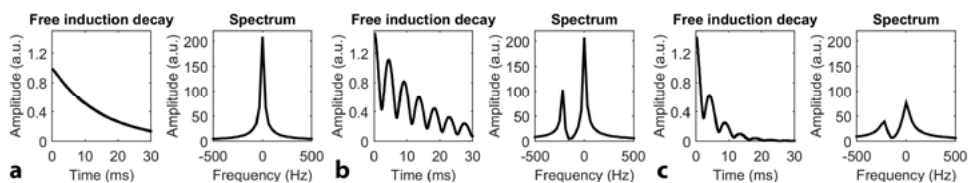

Figure 1.5: Free induction decay (FID) curves and the corresponding spectra obtained with spectroscopic imaging. The examples shown correspond to an on-resonance signal (a), an on-resonance signal (water) combined with another signal with a chemical shift difference of 3.4 ppm (fat) (b) and the spectra as in (b) affected by additional dephasing due to field inhomogeneities (c).

1.5.4 T_2^* DEPHASING AND SPIN-ECHOES

In both frequency- and phase-encoded sequences the presence of field inhomogeneities causes additional phase evolution, leading to a decrease of the MR signal over time. The transversal decay constant T_2, a tissue specific property, is therefore difficult to measure with the previously described gradient-echo techniques. For static field inhomogeneities within a voxel, such as static local dipole fields induced by local dχ effects (i.e. iron deposits, Holmium microspheres)(22-24) the signal can decay very rapidly. The decay constant that is measured with gradient-echo experiments is called the T_2^* relaxation time and is defined as:

$$\frac{1}{T_2^*} = \frac{1}{T_2} + \frac{1}{T_2'}$$

[1.21]

The term T_2' includes static dephasing effects, while the T_2 decay describes dynamic interactions on the molecular level. This has important implications for MRI near field inhomogeneities. The non-zero TE of gradient-echo sequences can cause substantial T_2' dephasing of the signal in the case of strong dχ gradients, such as in the presence of orthopedic implants. For static field inhomogeneities, the dephasing term can be reversed by applying a refocusing pulse of 180^0 between the 90^0 rf excitation pulse and the acquisition interval (Figure 1.6). The refocusing pulse is placed exactly TE/2 ms after the excitation time to achieve full refocusing of the T_2' effects at the center of the acquisition interval (TE). The experiment described here is called a spin-echo (SE) experiment (25), which is the basis of many sequences that are currently applied in the clinic. The SE images are unaffected by static dephasing, significantly decreasing signal voids in the images. Frequency-encoded SE images, however, are still affected by geometrical distortions, which can only be prevented with fully phase-encoded sequences.
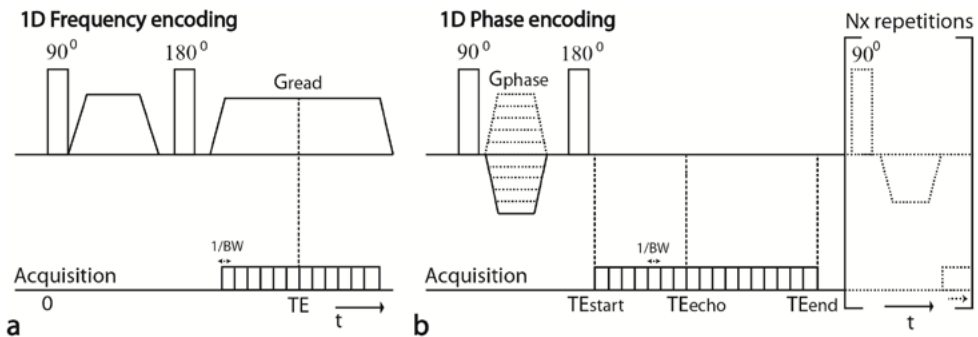

Figure 1.6: 1D spin-echo sequences with a frequency encoded gradient (a) and a phase encoding gradients (b). An additional 180^0 pulse is placed between the spatial encoding gradients and the acquisition interval and the polarity of the gradients before the 180^0 pulse is reversed. Full refocusing of static dephasing effects occurs at the TE in (a) and at the TE_{echo} in (b).

In the case of strong field offsets, such as when imaging near metal, image artifacts still occur in spin-echo imaging. This is illustrated in a knee of a volunteer that has undergone a posterior ligament reconstruction in the past (Figure 1.7). The posterior ligament was fixated with titanium screws, which induces multi-kHz off-resonance effects. The position of the screws can be seen in a sequence with an ultra-short TE (UTE), where all the tissue is relatively unaffected by T_2 relaxation and signal voids appear close to the screws (Figure 1.7a). The screws that were fixed at both ends of the graft, caused incomplete suppression of fat and signal hyper-intensities (Figure 1.7b). The metal artifacts were prevented in the two phase-encoded dimensions (Figure 1.7c), but were still affected by distortions in the slice direction. To also apply phase encoding in the third dimension for a phase-encoded spin-echo sequence would require hours of acquisition time that would be clearly unfeasible for an *in vivo* setting.

19

Figure 1.7: Images of the knee with a proton density weighted 3D ultra-short TE gradient-echo sequence (a), a fat-suppressed T_2 weighted turbo-spin echo sequence (b) and a 2D phase-encoded spin-echo sequence (c-d). The slice location of the 2D-PE-SE images is indicated in (a-b).

1.5.5 EXAMPLES OF GEOMETRICAL DISTORTIONS DUE TO FIELD INHOMOGENEITIES

In this section two spin-echo MRI experiments demonstrate image artifacts that can arise from field inhomogeneities and chemical shift. First, the effect of geometrical distortions in the frequency encoding direction are demonstrated for dχ-effects between air and gel (Δχ = 9 ppm) embedded in a rectangular grid (Figure 1.8). When observing the grid and the shape of the air containing sphere in the center of the phantom image distortions can be observed (Figure 1.8a-b). The bending of the gridlines (Figure 1.8a-b) and formation of an arrow-like pattern (Figure 1.8b) are typical geometrical distortions that can arise in frequency-encoded imaging. These distortions can be decreased by increasing the readout gradient strength (Figure 1.8a) at the cost of SNR (sect 1.6). These image distortions occur at the spatial locations with the highest frequency offsets (Figure 1.8d), as can be expected from Eq 1.17. In the case of a 3D phase-encoded (PE-)SE acquisition a lower bandwidth can be used without introducing geometrical distortions in the gridlines or distorting the shape of the sphere (Figure 1.8c).
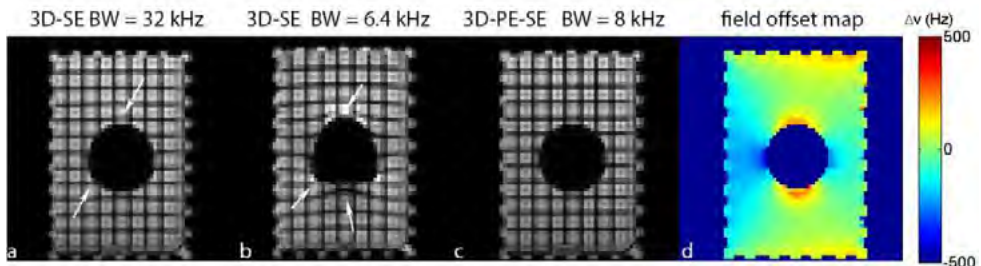

Figure 1.8: Coronal MR images of geometrical distortions caused by an air sphere embedded in a gel phantom with a rectangular grid. 3D-SE magnitude images obtained with a readout bandwidth of 32 kHz (a) and 6.4 kHz (b), a 3D phase-encoded (PE)-SE image at the TE_{echo} point (c) and the derived field offset map (d) are shown. Geometrical distortions are indicated by arrows.

Second, the formation of slice distortions due to dχ induced gradients and chemical shift are demonstrated for an object with a rectangular grid at the top of a phantom with two spheres containing air and oil in the middle (Figure 1.9). When selecting a slice in the absence of off-resonance frequencies, such as a uniform gel (Figure 1.9a), no distortions are observed. In the case of the presence of air in the selected slice local bending of the slice profile occurs, due to dχ differences between air and gel (Figure 1.9b), while chemical shift differences between oil and gel lead to a shift in the selected slice location (Figure 1.9b), as both described by Figure 1.4. The experiment was repeated after placing a titanium rod (Δχ =180 ppm) on top of the phantom. In doing so, dχ-induced gradients were present in the selected slices, leading to slice distortions in the previously undistorted slice (Figure 1.9ci) and in-plane signal shifts in in the frequency-encoded dimension (from top to bottom). Increasing the slice selection gradient strength decreased the slice distortions (Eq 1.19), but was unable to fully correct the selected slice profile (Figure 1.9ii). By omitting the slice selection and frequency encoding gradients a completely geometrically undistorted 3D dataset was acquired (Figure 1.9iii). The decrease in signal at the center of the phase-encoded image (Figure 1.9c,iii) arises from partial excitation of the total signal, which occurs when the offset ΔB is larger than the RF bandwidth Δω$_{rf}$.
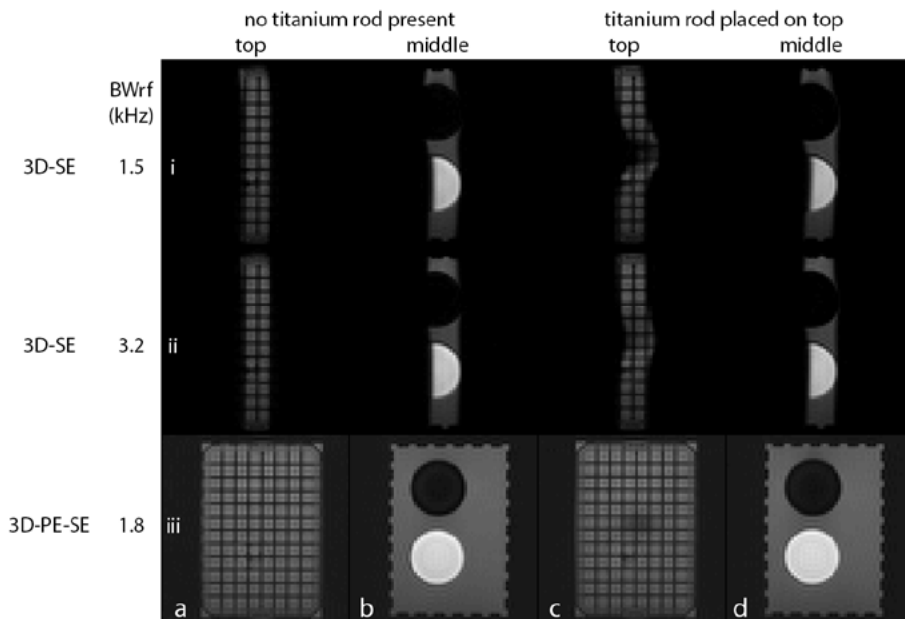
Figure 1.9: Visualization of slab distortions caused by air, oil and titanium induced field differences. Slices from the top (a,c) and the middle of phantom (b,d) are shown before (a,b) and after (c,d) the placement of a titanium rod near the top of the phantom. The rod was placed perpendicular to B0 and parallel to the presented slice profiles. Selected slab profiles are shown for two different excitation bandwidths (i,ii), thereby adjusting the slab selection gradient strength with a similar factor. Non-selective 3D PE-SE images are shown for comparison (iii).

1.6 SENSITIVITY

The sensitivity of MRI is defined as the signal to noise ratio (SNR) per unit time, which is dependent on the gyromagnetic ratio of the measured spin nucleus, readout bandwidth, noise characteristics, relaxation time and spin density of the object of interest (3). The transversal relaxation time (T_2/T_2^*) puts a lower limit on the acquisition window where signal still contributes to an increase in the SNR, because the MR signal decreases over time. From the literature it is known that the optimal sensitivity for gradient and spin-echo based acquisitions is achieved for an acquisition window of 1.26 T_2^* and 2.52 T_2^* (26), respectively, followed by the shortest achievable repetition time (TR) with the optimal flip angle. In frequency- and phase-encoded sequences the bandwidth can be adjusted to optimize the sensitivity of the MRI experiment. In the case of frequency-encoded experiments, however, this will require a reduced readout gradient strength, thereby increasing the geometrical distortions related to off-resonance effects (Figure 1.8, Eq 1.17). In the case of phase-encoded MRI, no geometrical distortions occur when changing the bandwidth. This allows long acquisition intervals that can take up to 80% of the total time in a single repetition, which is very efficient with respect to the total signal measured per repetition time. This leads to excellent SNR properties of phase-encoded sequences (3,26) that are especially useful for studies aiming to detect low concentration metabolites. The high sensitivity of phase-encoded MRI was used in this thesis to determine sodium concentrations and chemotherapeutic drugs in the human body that are present in very low concentrations.

1.7 NON-PROTON MRI AND SPECTROSCOPY

In current clinical practice the vast majority of MRI investigations focus on imaging of the anatomy by measuring the water and fat signal at the proton resonance frequency. Contrast is generated from differences in relaxation behavior, diffusion, perfusion, functional imaging etc., providing an indirect measure for tissue integrity or disease detection. The signal intensity variations can be difficult to relate to the actual disease state or can even be undetectable if the disease is very diffuse. More direct measures of the underlying biochemistry can be obtained by measuring multiple low concentration metabolites after suppression of the water and fat signal. In this way alterations can be detected in, for example, the metabolite profile in tumor metabolism (27) or brain disease (28,29). While proton spectroscopy can be used to detect metabolites with low concentrations it can be hard to detect disease related changes in the resonances due to background contamination caused by signal leakage from neighboring voxels, incomplete water and fat suppression and contributions of macromolecular structures. Furthermore, the chemical shift differences between spectral peaks can be small, causing overlap of multiple metabolites at a single frequency (15,30).

The field of non-proton imaging and spectroscopy is less well known and covers detection of spin nuclei such as ^{23}Na, ^{31}P, ^{13}C, ^{19}F, and others (4). Detection of these nuclei requires specific hardware that can measure the resonances at the corresponding Larmor frequency of the non-proton nuclei. Measuring at a different Larmor resonance frequency eliminates background signals from protons that are present in almost all biological molecules. This makes non-proton measurements a very specific method for biochemical investigations. Non-proton nuclei are involved in different biochemical processes and have been used to study cancer metabolism (i.e. glycolytic pathway, ATP consumption) (31,32), cellular integrity (33), drug metabolism in the body (16,34) and energy utilization in the muscles (35,36).

Despite the diagnostic potential of non-proton MR investigations there has been no widespread adaptation of these techniques to date. The main limitations for *in vivo* measurements are 1) the extremely low sensitivity caused by concentrations in the μM to mM range, 2) the low gyromagnetic ratios which can be 3-4x lower than for proton and 3) the lack of readily available hardware. Despite these obstacles, promising initial clinical results of non-proton imaging and spectroscopy have been reported in recent years (37-39). In this thesis, the advantageous signal characterization and sensitivity properties of phase-encoded MRI were explored in combination with recent hardware improvements to enable sodium and fluorine investigations with potential applications in early disease detection and drug efficacy assessment.

1.8 THESIS OUTLINE

The aim of this thesis was to develop phase-encoded MRI methods for geometrically undistorted imaging and signal characterization in the presence of field inhomogeneities, such as caused by susceptibility induced off-resonance effects and chemical shift. The initial experiments in this chapter demonstrated the advantageous geometrical properties of phase-encoded imaging for modest off-resonance effects (~1 kHz), without worrying about scan time limitations. To provide a solution for accurate post-operative imaging near metal orthopedic implants, however, it will be necessary to address the scan time limitations of phase-encoded MRI. Furthermore, the strong susceptibility induced field inhomogeneities (~16 - 40 kHz) surpass the achievable excitation bandwidths at clinical systems, thereby limiting the use of standard available phase-encoded MRI sequences.

In Chapters 2 and 3 the geometrical accuracy, acquisition times and excitation bandwidths of phase-encoded spin-echo sequences were investigated for imaging near orthopedic implants. In Chapter 2, a conventional 3D phase-encoded spin-echo (3D-PE-SE) approach was used as a starting point to investigate the geometrical accuracy of frequency and phase-encoded sequences near titanium. To reduce the acquisition time to acceptable levels, turbo spin-echo (TSE) and compressed sensing acceleration methods were explored for fast

3D-PE-TSE imaging. In Chapter 3 a method was implemented for more demanding metal alloys, such as cobalt-chromium or stainless steel, by adding a multispectral excitation scheme to the 3D-PE-TSE sequence. The resulting multispectral 3D-PE-TSE method was used to investigate the trade-off between acquisition time and image quality near strong paramagnetic materials.

In Chapters 4 to 6 the temporally resolved signal of phase-encoded free-induction decay (FID) sequences was exploited to accurately investigate the behavior of the MR signal with a sub-ms sampling rate. In Chapter 4, a 2D multiple single-point sequence was presented to measure repetitive field disturbances that are triggered simultaneously with the MR acquisition. In this way it might be possible to evaluate the MR system performance or detect dephasing effects from induced currents, such as induced in transcranial magnetic stimulation (TMS) therapies for example. In Chapter 5, a phase-encoded ultra-short echo-time (UTE) method was presented to accurately perform bi-exponential transverse relaxation mapping of sodium that is hard to achieve with existing MRI techniques. The transverse relaxation behavior of sodium has been related to early disease onset of degenerative diseases, such as osteoarthritis, and can potentially enable early treatment to improve patient outcome. In Chapter 6, an advanced technical setup is presented for detection of fluorine containing chemotherapy and its metabolism. The direct detection of chemotherapeutic drugs holds potential to determine the efficacy in an early stage of the treatment, which may improve treatment planning and reduce toxicity effects in non-responding patients.

In Chapter 7 we discuss the presented findings and provide a perspective for future and ongoing work followed by a Summary in English and Dutch.

REFERENCES

1.   Bloch F. Nuclear induction. Physical review 1946;70(7-8):460.
2.   Purcell EM, Torrey H, Pound RV. Resonance absorption by nuclear magnetic moments in a solid. Physical review 1946;69(1-2):37.
3.   Haacke EM, Brown RW, Thompson MR, Venkatesan R. Magnetic resonance imaging: Wiley-Liss New York:; 1999.
4.   De Graaf RA. In vivo NMR spectroscopy: principles and techniques: John Wiley & Sons; 2008.
5.   Levitt MH. Spin dynamics: basics of nuclear magnetic resonance: John Wiley & Sons; 2001.
6.   Damadian R. Tumor detection by nuclear magnetic resonance. Science 1971;171(3976):1151-1153.
7.   Mamisch TC, Dudda M, Hughes T, Burstein D, Kim YJ. Comparison of delayed gadolinium enhanced MRI of cartilage (dGEMRIC) using inversion recovery and fast T1 mapping sequences. Magn Reson Med 2008;60(4):768-773.
8.   Puntmann VO, Voigt T, Chen Z, Mayr M, Karim R, Rhode K, Pastor A, Carr-White G, Razavi R, Schaeffter T. Native T1 mapping in differentiation of normal myocardium from diffuse disease in hypertrophic and dilated cardiomyopathy. JACC Cardiovasc Imaging 2013;6(4):475-484.
9.   Lauterbur PC. Image formation by induced local interactions: examples employing nuclear magnetic resonance. Nature 1973;242(5394):190-191.
10. Mansfield P, Grannell PK. NMR'diffraction'in solids? Journal of Physics C: solid state physics 1973;6(22):L422.
11. Ernst RR, Anderson W. Application of Fourier transform spectroscopy to magnetic resonance. Rev Sci Instrum 1966;37(1):93-102.
12. Schenck JF. The role of magnetic susceptibility in magnetic resonance imaging: MRI magnetic compatibility of the first and second kinds. Med Phys 1996;23(6):815-850.
13. Haacke EM, Xu Y, Cheng YCN, Reichenbach JR. Susceptibility weighted imaging (SWI). Magn Reson Med 2004;52(3):612-618.
14. Proctor W, Yu F. The dependence of a nuclear magnetic resonance frequency upon chemical compound. Physical Review 1950;77(5):717.
15. Boer VO, Siero JC, Hoogduin H, van Gorp JS, Luijten PR, Klomp DW. High-field MRS of the human brain at short TE and TR. NMR Biomed 2011;24(9):1081-1088.
16. Stevens A, Morris P, Iles R, Sheldon P, Griffiths J. 5-fluorouracil metabolism monitored in vivo by 19F NMR. Br J Cancer 1984;50(1):113.
17. Rothman DL, Behar KL, Hyder F, Shulman RG. In vivo NMR studies of the glutamate neurotransmitter flux and neuroenergetics: implications for brain function. Annu Rev Physiol 2003;65(1):401-427.
18. Golman K, Lerche M, Pehrson R, Ardenkjaer-Larsen JH. Metabolic imaging by hyperpolarized 13C magnetic resonance imaging for in vivo tumor diagnosis. Cancer Res 2006;66(22):10855-10860.
19. Koch K, Hargreaves B, Pauly KB, Chen W, Gold G, King K. Magnetic resonance imaging near metal implants. J Magn Reson Imaging 2010;32(4):773-787.
20. Dixon WT. Simple proton spectroscopic imaging. Radiology 1984;153(1):189-194.
21. Posse S, Otazo R, Dager SR, Alger J. MR spectroscopic imaging: principles and recent advances. J Magn Reson Imaging 2013;37(6):1301-1325.
22. Wang Y-XJ, Hussain SM, Krestin GP. Superparamagnetic iron oxide contrast agents: physicochemical characteristics and applications in MR imaging. Eur Radiol 2001;11(11):2319-2331.
23. Gandon Y, Olivie D, Guyader D, Aube C, Oberti F, Sebille V, Deugnier Y. Non-invasive assessment of hepatic iron stores by MRI. The Lancet 2004;363(9406):357-362.

24. Nijsen JF, Seppenwoolde JH, Havenith T, Bos C, Bakker CJ, van het Schip AD. Liver tumors: MR imaging of radioactive holmium microspheres--phantom and rabbit study. Radiology 2004;231(2):491-499.

25. Hahn EL. Spin echoes. Physical review 1950;80(4):580.

26. Pohmann R, Von Kienlin M, Haase A. Theoretical evaluation and comparison of fast chemical shift imaging methods. J Magn Reson 1997;129(2):145-160.

27. Sijens PE, Levendag PC, Vecht CJ, Dijk Pv, Oudkerk M. 1H MR spectroscopy detection of lipids and lactate in metastatic brain tumors. NMR Biomed 1996;9(2):65-71.

28. Harada M, Taki MM, Nose A, Kubo H, Mori K, Nishitani H, Matsuda T. Non-invasive evaluation of the GABAergic/glutamatergic system in autistic patients observed by MEGA-editing proton MR spectroscopy using a clinical 3 tesla instrument. J Autism Dev Disord 2011;41(4):447-454.

29. Buckley PF, Moore C, Long H, Larkin C, Thompson P, Mulvany F, Redmond O, Stack JP, Ennis JT, Waddington JL. 1 H-magnetic resonance spectroscopy of the left temporal and frontal lobes in schizophrenia: Clinical, neurodevelopmental, and cognitive correlates. Biol Psychiatry 1994;36(12):792-800.

30. Tkáč I, Öz G, Adriany G, Uğurbil K, Gruetter R. In vivo 1H NMR spectroscopy of the human brain at high magnetic fields: metabolite quantification at 4T vs. 7T. Magn Reson Med 2009;62(4):868-879.

31. Singer S, Souza K, Thilly WG. Pyruvate utilization, phosphocholine and adenosine triphosphate (ATP) are markers of human breast tumor progression: a 31P-and 13C-nuclear magnetic resonance (NMR) spectroscopy study. Cancer Res 1995;55(22):5140-5145.

32. Artemov D, Bhujwalla ZM, Pilatus U, Glickson JD. Two-compartment model for determination of glycolytic rates of solid tumors by in vivo13C NMR spectroscopy. NMR Biomed 1998;11(8):395-404.

33. Kim RJ, Judd RM, Chen E-L, Fieno DS, Parrish TB, Lima JA. Relationship of elevated 23Na magnetic resonance image intensity to infarct size after acute reperfused myocardial infarction. Circulation 1999;100(2):185-192.

34. El-Tahtawy A, Wolf W. In vivo measurements of intratumoral metabolism, modulation, and pharmacokinetics of 5-fluorouracil, using 19F nuclear magnetic resonance spectroscopy. Cancer Res 1991;51(21):5806-5812.

35. Iotti S, Lodi R, Frassineti C, Zaniol P, Barbiroli B. In vivo assessment of mitochondrial functionality in human gastrocnemius muscle by 31P MRS. The role of pH in the evaluation of phosphocreatine and inorganic phosphate recoveries from exercise. NMR Biomed 1993;6(4):248-253.

36. Kemp GJ, Meyerspeer M, Moser E. Absolute quantification of phosphorus metabolite concentrations in human muscle in vivo by 31P MRS: a quantitative review. NMR Biomed 2007;20(6):555.

37. Van Laarhoven H, Klomp D, Rijpkema M, Kamm Y, Wagener D, Barentsz J, Punt C, Heerschap A. Prediction of chemotherapeutic response of colorectal liver metastases with dynamic gadolinium-DTPA-enhanced MRI and localized 19F MRS pharmacokinetic studies of 5-fluorouracil. NMR Biomed 2007;20(2):128-140.

38. van der Kemp WJ, Stehouwer BL, Luijten PR, van den Bosch MA, Klomp DW. Detection of alterations in membrane metabolism during neoadjuvant chemotherapy in patients with breast cancer using phosphorus magnetic resonance spectroscopy at 7 Tesla. SpringerPlus 2014;3(1):634.

39. Qian Y, Laymon C, Oborski M, Drappatz J, Lieberman F, Mountz J. PET ML-10 Uptake Correlates with MRI Bound Sodium Change in Early Assessment of Response to Cancer Therapy of Brain Tumors. J Nucl Med 2015;56(supplement 3):1180-1180.

GEOMETRICALLY UNDISTORTED IMAGING

GEOMETRICALLY UNDISTORTED MRI IN THE PRESENCE OF FIELD INHOMOGENEITIES USING COMPRESSED SENSING ACCELERATED BROADBAND 3D PHASE-ENCODED TURBO SPIN-ECHO IMAGING

ABSTRACT

In this study, we explore the potential of compressed sensing (CS) accelerated broadband 3D phase-encoded turbo spin-echo (3D-PE-TSE) for the purpose of geometrically undistorted imaging in the presence of field inhomogeneities. To achieve this goal 3D-PE-SE and 3D-PE-TSE sequences with broadband rf pulses and dedicated undersampling patterns were implemented on a clinical scanner. Additionally, a 3D multispectral spin-echo (ms3D-SE) sequence was implemented for reference purposes. First, we demonstrated the influence of susceptibility induced off-resonance effects on the spatial encoding of broadband 3D-SE, ms3D-SE, 3D-PE-SE and 3D-PE-TSE using a grid phantom containing a titanium implant ($\Delta\chi$=182ppm) with X-ray CT as a gold standard. These experiments showed that the spatial encoding of 3D-PE-(T)SE was unaffected by susceptibility induced off-resonance effects, which caused geometrical distortions and/or signal hyper-intensities in broadband 3D-SE and, to a lesser extent, in ms3D-SE frequency encoded methods. Additionally, an SNR analysis was performed and the temporally resolved signal of 3D-PE-(T)SE sequences was exploited to retrospectively decrease the acquisition bandwidth and obtain field offset maps. The feasibility of CS acceleration was studied retrospectively and prospectively for the 3D-PE-SE sequence using an existing CS algorithm adapted for the reconstruction of 3D data with undersampling in all three phase-encoded dimensions. CS was combined with turbo-acceleration by variable density undersampling and spherical stepwise T2 weighting by randomly sorting consecutive echoes in predefined spherical k-space layers. The CS-TSE combination resulted in an overall acceleration factor of 60, decreasing the original 3D-PE-SE scan time from 7 hours to 7 minutes. Finally, CS accelerated 3D-PE-TSE *in vivo* images of a titanium screw were obtained within 10 minutes using a micro-coil demonstrating the feasibility of geometrically undistorted MRI near severe field inhomogeneities.

2.1 Introduction

Field inhomogeneities have detrimental effects in conventional magnetic resonance imaging (MRI) and can degrade the image quality by geometric distortions, signal misregistration, signal dephasing and incomplete excitation. These off-resonance effects are the result of background field variations of the main magnetic field and magnetic susceptibility differences within the subject, for example originating from the presence of external sources (e.g. interventional devices, orthopedic implants, contrast agents). The resultant susceptibility artifacts constitute a serious obstacle when accurate spatial localization is required, such as in MR guided radiotherapy (1-3), image guided interventions (4-6), stereotactic neurosurgery (7,8) and imaging near metal implants (9,10).

With regard to the suppression of susceptibility artifacts, it can readily be inferred from the abundant literature (11) that spin-echo techniques are usually to be preferred over gradient-echo techniques, that 3D techniques are preferable to 2D techniques, and that localization errors can be minimized by maximizing the readout and slice/slab selection gradients. In practice, however, the capability of the currently used gradient systems is often insufficient to fully suppress geometrical distortions in the presence of severe inhomogeneities. Aside from that, the use of strong gradients is known to compromise SNR (SNR~$1/\sqrt{G_{read}}$) and to invoke safety issues.

In the past decades, many acquisition (12-14) and processing based methods (15) have been proposed to diminish susceptibility artifacts in MRI. However, all the proposed methods are in principle still affected by geometrical distortions and/or signal pile up related to frequency encoding processes (16). The most promising clinical results so far, in our view, have been achieved with so-called multispectral approaches (i.e. MAVRIC, SEMAC). In such approaches, images are composed of multiple acquisitions, either by adding additional phase encodings in the slice direction (SEMAC) or by decomposing the excitation BW in multiple narrow bands to limit signal mismapping and to overcome excitation bandwidth limitations (MAVRIC). It should be emphasized that multispectral methods themselves are still under development with respect to processing and acquisition optimization (17,18).

In our group, we recently started to explore a more fundamental solution to prevent off-resonance-related artifacts, namely the use of purely phase-encoded sequences, such as practiced in single-point imaging (SPI) (19). As spatial encoding in the phase-encoded dimensions is by definition unaffected by field inhomogeneities and chemical shift differences, these sequences can be exploited to obtain geometrically undistorted MR images. Additional advantages of this approach, as opposed to conventional frequency encoded and multispectral sequences, are the acquisition of a temporally resolved signal due to the absence of a readout gradient and the possibility to exploit a large excitation bandwidth without increasing the in-plane spatial distortions due to the increased range of excited off-resonance signal.

Although phase-encoded imaging has unique and favorable properties, the inherently long acquisition times – a typical 3D examination may easily take several hours – are a major challenge for use in a clinical setting. Recently a variable flip angle phase-encoded 3D fast spin-echo technique was shown to significantly reduce the acquisition time of phase-encoded imaging (20). In this retrospective study it was suggested that it must in principle be possible to achieve clinically acceptable scan times by combining their approach with undersampling techniques, e.g. a spherical shutter, partial fourier imaging and parallel imaging. A rather new concept recently proposed to reduce acquisition times in MRI as well is compressed sensing (CS) (21-23), which exploits the implicit data redundancy of signals in a transform domain with a sparse representation of the data (i.e. wavelet, finite differences, image), known as sparsity or compressibility. A crucial requirement for CS reconstruction of MR images is incoherent undersampling, in order to guarantee incoherent aliasing artifacts in the sparse transform domain. A sampling pattern that meets this criterion can be obtained by quasi-random undersampling of k-space (23), which is an intuitive match to the point-by-point sampling of purely phase-encoded techniques.

In the study reported here we explore the potential of CS accelerated 3D phase-encoded turbo-spin-echo imaging (3D-PE-TSE) to reduce the typically long acquisition times of 3D phase-encoded spin-echo imaging (3D-PE-SE) (hours) to acceptable time frames for geometrically undistorted imaging *in vivo* (minutes). For this purpose, broadband 3D-PE-SE and 3D-PE-TSE sequences were implemented on a clinical MR system and a variable density undersampling scheme with a stepwise T_2 weighting was designed to enable the combination of applying a spherical shutter, CS reconstruction and TSE acceleration. Additionally, a multispectral 3D-SE (ms3D-SE) sequence was implemented for reference purposes. The paper is organized as follows. First, we demonstrate the influence of susceptibility induced off-resonance effects on the spatial encoding in broadband 3D-SE, ms3D-SE, 3D-PE-SE and 3D-PE-TSE using a phantom containing a titanium hip implant ($\Delta\chi$=182ppm (24)) with X-ray CT used as a gold standard. A titanium implant was chosen out of practical considerations, such as the ability to cover the titanium induced off-resonance range on the order of 4kHz using standard rf pulses at 1.5T MRI systems, and the possibility to demonstrate the influence of strong susceptibility induced field gradients and smoothly varying frequency offsets on spatial encoding processes using a single object. Additionally, an SNR analysis was performed and the temporally resolved time signal in 3D-PE-(T)SE was exploited to demonstrate the feasibility to retrospectively increase the bandwidth and obtain field maps. Next, we present and evaluate results obtained with fully sampled, retrospectively and prospectively CS accelerated 3D-PE-(T)SE acquisitions to determine an acceptable acceleration factor. Finally, we describe our first *in vivo* results with prospectively CS accelerated broadband 3D-PE-TSE in order to substantiate the feasibility of geometrically undistorted MRI *in vivo*.

2.2 METHODS

2.2.1 PHANTOM AND SUBJECTS

Gel phantom with a titanium hip implant and distortion grid: A phantom was designed with two purposes in mind: i) to demonstrate the effect of multi-kHz susceptibility induced field inhomogeneities on the spatial encoding in frequency and phase-encoded sequences and ii) to determine a suitable CS undersampling factor for 3D-PE-(T)SE scan time acceleration. The phantom was constructed of a rectangular container (23x14.5x8.6 cm) filled with 2% agarose gel and doped with 30.5 mg/L $MnCl_2.4H_2O$ embedding a titanium ($\Delta\chi$=182 ppm) femoral stem of a hip implant placed on top of a (horizontal) grid spanning 9x4 squares of 2.4x2.4 cm. The susceptibility induced field offset $\Delta\upsilon_0(x)=\gamma/2\pi\cdot\Delta B_0(x)$ causes spins at location x to be reconstructed at position x', which results in a shift with respect to the original location according to:

$$x' - x = \frac{2\pi}{\gamma G_{read}} \Delta\upsilon_0(x) \qquad [2.1]$$

where $\gamma/2\pi$ is the gyromagnetic ratio. The position shift x'-x is proportional to the Larmor frequency offset $\Delta\upsilon_0(x)$ and inversely proportional to the strength of the readout gradient G_{read}.

Human subject with a graft fixated by titanium screws: A 35 year old healthy volunteer with two titanium screws in the left knee was subjected to an MRI exam. Written informed consent of the healthy volunteer was obtained and the study was performed in accordance with local guidelines. The volunteer had received an anterior cruciate ligament reconstruction in the past (2003) in which the graft was fixated with titanium screws. Aim of the *in vivo* investigation was to illustrate the typical geometrical distortions and signal hyperintensities caused by titanium objects when using 3D-TSE, and to demonstrate their absence when using CS accelerated 3D-PE-TSE.

2.2.2 SEQUENCES AND ANALYSIS

In addition to standard 3D-SE, 3D-TSE, muli-slice TSE and X-ray CT acquisitions for demonstration, planning and reference purposes (details in section 'imaging parameters' and Table 2.1), three dedicated pulse sequences were implemented for this study: ms3D-SE, broadband 3D-PE-SE and broadband 3D-PE-TSE. The phase-encoded sequences were adapted so as to enable prospective k-space undersampling by restricting the acquisition to a user-specified subset of the original 3D Cartesian k-space.

Multispectral 3D spin-echo sequence: A ms3D-SE method was implemented as a reference for the geometrical accuracy of the phase-encoded sequences. To this end, a standard 3D-SE sequence was adapted by replacing the standard rf pulses by an apodized windowed sinc-gauss excitation and block refocusing pulse and by disabling the slice selection gradients to ensure the absence of slab distortions. In-plane geometrical distortions in the ms3D-SE images were decreased to a sub-pixel level by ensuring that $\gamma G_{read} \geq 2\pi\Delta\upsilon_0(x,y,z)$. This was achieved by 1) decomposing a 5 kHz frequency band into five overlapping 1.7 kHz frequency bands with a different center rf frequency to decrease the maximum off-resonance ($\Delta\upsilon_0(x,y,z)$) to ±0.85 kHz for each acquired 3D-SE image, 2) applying a strong (0.5 - 1.0 kHz/pixel) readout gradient (G_{read}) and 3) combining the five images into a ms3D-SE image using a sum-of-squares algorithm (13). The RF and demodulation frequency were shifted 0.85 kHz between each acquisition to cover the frequency range from -2.5 to +2.5 kHz, while also increasing the acquisition time a factor five compared to a single 3D-SE acquisition.

3D phase-encoded (turbo) spin-echo sequences: Broadband 3D-PE-SE and 3D-PE-TSE sequences (Figure 2.1) were implemented by adapting standard 3D spin-echo spectroscopic imaging and standard 3D turbo spin-echo spectroscopic imaging sequences. To achieve the desired imaging capabilities vendor specific software limitations regarding the maximum acquisition matrix of spectroscopic imaging were removed, slice selection gradients were disabled and crusher and spoiling gradients were added in all directions to avoid spurious echoes in case of imperfect signal refocusing and short repetition times. The standard spectroscopy pulses were replaced by a sinc-gauss excitation pulse and block refocusing pulses to achieve short echo-times. The excitation pulse bandwidth was 5.8 kHz (3D-PE-SE) or 4 kHz (3D-PE-TSE), covering the FWHM of the applied refocusing pulses to effectively obtain a sinc-profile with a cut-off at the borders of the excitation pulse profile. The refocusing pulses can be altered to adjust the refocusing profile at the cost of increasing TE and echo spacing if required. The pulse durations were decreased to increase the excitation and refocusing bandwidths. If necessary (Table 2.1), the flip angles were decreased as well to keep B_1 within hardware and safety limits. In addition to changes in the acquisition, a number of commonly applied spectroscopy post-processing steps were disabled, such as apodization and zerofilling of the time domain data.

In the case of 3D-PE-TSE a number of additional changes were implemented. First, the flip angle of the first refocusing pulse was increased to $((180+\alpha)/2)$, where α is the desired refocusing flip angle, to reduce oscillations in the signal amplitude over the echo train for non-180^0 refocusing pulses (25). In this case the first refocusing pulse was the limiting factor for the maximum achievable rf bandwidth, because this pulse has to produce the largest flip angle. For standard block pulses and a $B_{1,max}$ of 23 μT a bandwidth up to 3.5 kHz could be achieved without additional adjustments to the sequence. Additionally, the length of the

standard implemented crusher pairs was decreased to enable a shorter echo spacing and further decrease the acquisition time, without introducing additional artifacts.
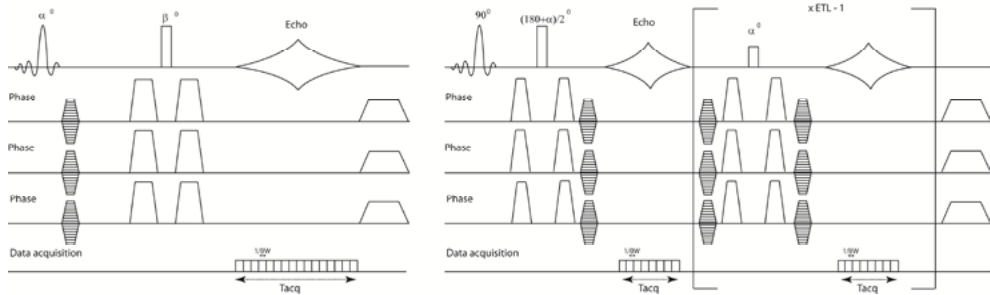

Figure 2.1: The 3D-PE-SE (left) and 3D-PE-TSE (right) sequences used for phase-encoded imaging in this work. The absence of a readout gradient allows the measurement of multiple single point images at different time points.

Exploiting the temporally resolved signal of phase-encoded data: The implemented 3D-PE-SE and 3D-PE-TSE sequences permitted the reconstruction of a series of single point images with varying T_2^* weighting, due to the absence of a readout gradient during the acquisition interval (T_{acq}). The successive points sampled during T_{acq} corresponded to the following 'echo times': $TE(n)=TE+(n-0.5Nt-1)dt$, with $dt=0.125$ms, $Nt=64$ (3D-PE-SE) and $Nt=16$ (3D-PE-TSE), $n=1:Nt$. These time points were exploited in an SNR analysis to either retrospectively decrease the acquisition bandwidth by complex averaging the time points centered around the echo top (n=33) or by spectrally resolving the images by taking the fourier transformation of the time domain (26). Additionally, field offset maps (Δv) were reconstructed by fitting a linear model ($\Delta v = \Delta\phi/(2\pi\Delta t)$) to the unwrapped phase images of eleven subsequent time points of the (CS-accelerated) 3D-PE-SE sequence centered around the echo top (n=28:38). The field offset (Δv) maps were masked using magnitude data for visualization purposes. All phase-encoded magnitude images shown in this paper were reconstructed from the echo top, which corresponds to the 'true' echo time.

SNR analysis: The SNR of the acquired 3D-SE, ms3D-SE, 3D-PE-SE and 3D-PE-TSE magnitude images was determined using SNR = $0.665 S_{ROI}/\sigma_{back}$, where S_{ROI} is the mean signal intensity in a uniform region of the phantom and σ_{back} is the standard deviation in the background. The background was visually inspected to avoid structured background noise before determining the standard deviation. The standard deviation was divided by 0.655, due to the Rician noise distribution in magnitude images (27). Additionally the SNR of 3D-PE-(T)SE magnitude images reconstructed from 1, 2 and 4 time points, a single spectrally resolved image and a sum-of-squares combination of all spectrally resolved images was determined.

2.2.3 COMPRESSED SENSING AND SAMPLING PATTERN DESIGN

In this work undersampling of 3D PE-(T)SE data was performed either after data acquisition using a fully sampled dataset (retrospective undersampling) or directly on the scanner by acquiring a reduced number of k-space points (prospective undersampling) before CS reconstruction. The retrospective study was performed with fully sampled 3D-PE-SE data to determine an undersampling density with satisfactory performance, which was applied for 3D-PE-SE and 3D-PE-TSE in a prospective study to actually obtain decreased data acquisition times.

Retrospective undersampling (with a factor of 2, 4, 6, 8 and 10) of the fully sampled 3D-PE-SE images was done by randomly selecting samples on a Cartesian grid in k-space according to a second order polynomial variable density probability function in all three phase encoding dimensions, with a fully sampled center. Such a pattern is known to create incoherent aliasing artifacts (23) which is a requirement for successful CS reconstruction. The normalized mean square error (NMSE) and correlation coefficient (CC) were calculated between the CS reconstructed and the fully sampled images as quantitative error measures for the overall reconstruction quality (28):

$$NMSE = \frac{\sum_m \sum_n (|A_{mn} - B_{mn}|)^2}{\sum_m \sum_n |B_{mn}|^2}$$

$$CC = \frac{\sum_m \sum_n (A_{mn} - \bar{A})(B_{mn} - \bar{B})}{\sqrt{(\sum_m \sum_n (A_{mn} - \bar{A})^2 \sum_m \sum_n (B_{mn} - \bar{B})^2)}} \qquad [2.2]$$

where A is the reconstructed magnitude image, $\bar{A}$ is the mean of A, B is the fully sampled image and $\bar{B}$ is the mean of B. The NMSE provides an absolute error metric between the reconstructed and the fully sampled data, while the CC gives an estimate of the correlation between two images.

Sampling pattern design for CS accelerated 3D-PE-TSE: To obtain a 3D variable density random undersampling pattern on a Cartesian grid for a 3D-PE-TSE sequence a dedicated sampling pattern was designed. First, to obtain a 3D spherical sampling pattern with a stepwise T_2 weighting, the k-space coordinates were sorted in spherical layers with each layer corresponding to a certain echo number and consisting of an equal number of points (Figure 2.2). All sampling points in a certain layer are therefore sampled at the same 'echo time' and have an equal T_2 weighting. By applying this sampling scheme the T_2 weighting is spread out mainly in the kx and ky direction for a low kz direction and uniformly in kx, ky and kz for isotropic matrices. Variable density undersampling patterns for CS-TSE accelerated imaging were designed in a similar fashion. A side effect of the CS-TSE sampling schemes are decreased thicknesses of the center echo layers and increased thicknesses of the outer echo layers (Figure 2.2 bottom row) compared to the spherical TSE sampling patterns (Figure 2.2 upper row), which is caused by the variable density sampling. Effectively, this leads to an increased T_2 weighting over k-space in the acquired data. The

effective TE of the presented sampling patterns with an echo train length (ETL) of 10 is determined by the sampling time of the first echo, known as a 'low-high' echo scheme.
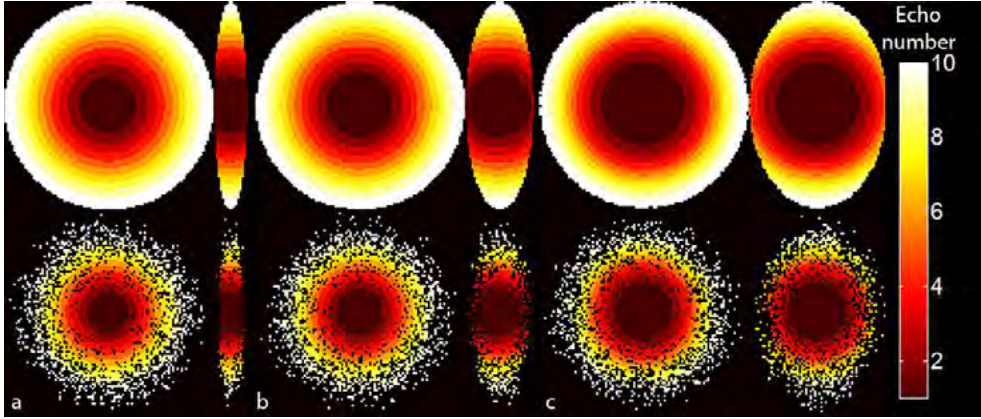

Figure 2.2: The sampling patterns used in this work for fully sampled 3D-PE-TSE data with a spherical shutter (top row) and CS accelerated 3D-PE-TSE (bottom row). The kx-ky and ky-kz plane through the center of k-space are shown for acquisition matrices 128x128x16 (a), 96x96x32 (b) and 96x96x64 (c). The order of each sampling point in the echo train is indicated by the index.

Image reconstruction: All CS reconstructions of undersampled data were performed using an adaptation of the reconstruction algorithm made publicly available by Lustig (23). A non-linear conjugate gradient solver was used to minimize $\lambda_w||\psi_w m||_1 + \lambda_{TV}TV(m)$, where $||\psi_w m||_1$ is the L_1 norm regularization in the wavelet transform domain and TV(m) a total variation regularization in the image domain with weighting factors λ_w and λ_{TV}. The original 2D regularizations were replaced with a 3D wavelet (Daubechies 3) L_1 norm regularization (λ_w) and a 3D total variation norm regularization (λ_{TV}) to reconstruct the 3D phase-encoded data with three undersampled dimensions. The values of the parameters λ_w and λ_{TV} were empirically determined and set to 0.0037 and 0.0013 (weights 3:1). The magnitude of the data was scaled between 0 and 1 before reconstruction by dividing the data through the maximum magnitude value of the 3D dataset. The 3D wavelet transform was implemented in C++ including parallel computation and compiled as .mex files to decrease the reconstruction times in Matlab. Reconstruction times for a single time point of the 3D dataset with 100 iterations was around 60 sec on average, depending on the acquisition matrix, using an Intel Core i7 machine (2.93 GHz, 16GB RAM, Windows 7) with MATLAB (Mathworks Inc, Natick, MA).

2.2.4 GENERAL IMAGING PARAMETERS

All MR imaging experiments were performed on a 1.5T MR system (Achieva, Philips Medical Systems, Best, The Netherlands), using either an eight element head coil (*in vitro*), a two element surface coil and/or a 4.7-mm diameter micro-coil (*in vivo*). References to the objects/subjects under investigation and accompanying MR imaging parameters as used in this work are listed in Table 2.1. The most important variations in the setup and the parameter settings between the experiments were as follows: In the phantom study, the readout bandwidth was varied between 505 Hz/pixel and 1011 Hz/pixel for ms3D-SE. The 3D-SE, 3D-PE-SE and 3D-PE-TSE acquisitions were acquired using a single excitation, while a multi-excitation scheme was used for the ms3D-SE acquisitions. In addition to a fully sampled 3D-PE-SE acquisition, an undersampled dataset was acquired with the same undersampling pattern as obtained from the retrospective CS study. The 3D-PE-TSE data was acquired using a spherical shutter and a dedicated undersampling pattern (Figure 2.2a). For the *in vivo* experiments, two different frequency encoding directions were used in 3D-TSE acquisitions to clearly show the effect of field inhomogeneities on the geometrical accuracy in the readout direction. CS accelerated 3D-PE-TSE data was acquired for two different acquisition matrices (Figure 2.2b,c) using the acceleration factor determined in the phantom study.

A X-ray CT scan (Brilliance, Philips Medical Systems, Best, The Netherlands) of the phantom was acquired as a gold standard. The CT scan was reformatted to the same slice thickness as the MR images. X-ray CT imaging parameters included a FOV of 183x183 mm, matrix = 512x512, slice thickness = 1mm, gap 0.5 mm, collimation of 64x0.625 mm, pitch 0.671, rotation time = 0.5s. X-ray tube voltage and current were 140 KV and 337 mA with mAs/slice = 250 mA.

Table 2.1:
MR Imaging parameters used in this work

Object	Scan	Fig	FOV (mm)	Voxel (mm)	Read dir[b]	BW read (Hz/pix)	T_{acq} (ms)[c]	Flip angle (°)	BW rf (kHz)[d]	Time (min)	Scan time reduction
Phantom	SE	2.3	256x192x80	2x1.5x5	F	505.7	2	60-60	5.0	3.5	
	msSE[a]	2.3	256x192x80	2x1.5x5	F	505.7	2	90-180	1.7	17.5	
	msSE[a]	2.3	256x192x80	2x1.5x5	F	1011.4	1	90-180	1.7	17.5	
	PE-SE	2.3-2.6	256x192x80	2x1.5x5			8	60-60	5.0	436	0
	PE-SE	2.6	256x192x80	2x1.5x5			8	60-60	5.0	73	6
	PE-TSE	2.4,2.6	256x192x80	2x1.5x5			2	90-120-[60]	2.9	21.8	20
	PE-TSE	2.6	256x192x80	2x1.5x5			2	90-120-[60]	2.9	7.3	60
Knee	TSE	2.7	128x96x80	1.33x1x1.25	F	217.7	4.6	90-60	2.9	3.5	
	TSE	2.7	128x96x80	1.33x1x1.25	A	217.7	4.6	90-60	2.9	3.5	
	PE-TSE	2.7	128x96x80	1.33x1x1.25			2	90-120-[60]	2.9	19.8	60
	PE-TSE	2.7	128x96x80	1.33x1x2.5			2	90-120-[60]	2.9	9.8	60

Phantom = titanium hip implant on a grid, TR/TE=100/15 ms and 100/9 ms were used in the 3D-PE-SE and 3D-PE-TSE sequences.
Knee = knee containing titanium screws, TR/TE=120/11ms for PE-TSE
a) Multispectral 3D-SE acquisitions consisting of five measurements with a 0.85kHz stepped central RF frequency
b) The fat shift direction with respect to water, F = Feet direction, A = anterior direction
c) The acquisition interval equals either the duration of the readout gradient (SE, msSE, TSE) or the temporally resolved signal (PE-SE, PE-TSE)
d) The indicated rf bandwidth is the bandwidth of the first refocusing pulse, which determines the effective bandwidth.

2.3 RESULTS

2.3.1 PHASE-ENCODED IMAGING IN THE PRESENCE OF FIELD INHOMOGENEITIES

The effect of field inhomogeneities on the performance of spatial encoding of broadband 3D-SE, ms3D-SE and 3D-PE-SE sequences is demonstrated in Figure 2.3, with X-ray CT acting as a gold standard. The 3D-SE image acquired with a 5 kHz excitation bandwidth (Figure 2.3a) clearly shows bending of the grid and signal-pile-up at locations with large field inhomogeneities (Figure 2.3f), as indicated by arrows. The presence of off-resonances up to 2.5 kHz resulted in a maximal shift of 5 pixels against (-) or in (+) the readout gradient direction, respectively, taking into account a readout bandwidth of 0.5 kHz/pixel (Eq 2.1). Signal pile-up artifacts as well as geometrical distortions with respect to the grid were significantly decreased in the ms3D-SE images (Figure 2.3b,c) where the maximum pixel shift was ±1.7 pixels for a readout bandwidth of 0.5 kHz/pixel (Figure 2.3b) and ±0.85 pixels for a readout bandwidth of 1 kHz/pixel (Figure 2.3c). By increasing the readout bandwidth a factor 2, the SNR was decreased with a factor of $\sim\sqrt{2}$ (Table 2.2). Despite the sub-pixel geometrical distortions in the ms3D-SE images, hyper-intensities were still visible at the locations close the titanium object with the largest susceptibility induced field gradients, which were absent in the 3D-PE-SE images (Figure 2.3d). Furthermore, the contour of the implant in the latter images was nearly identical to the gold standard CT image (Figure 2.3e), indicating that all but a fraction of off-resonance spins close to the implant were excited in a single acquisition using a 5 kHz excitation bandwidth.
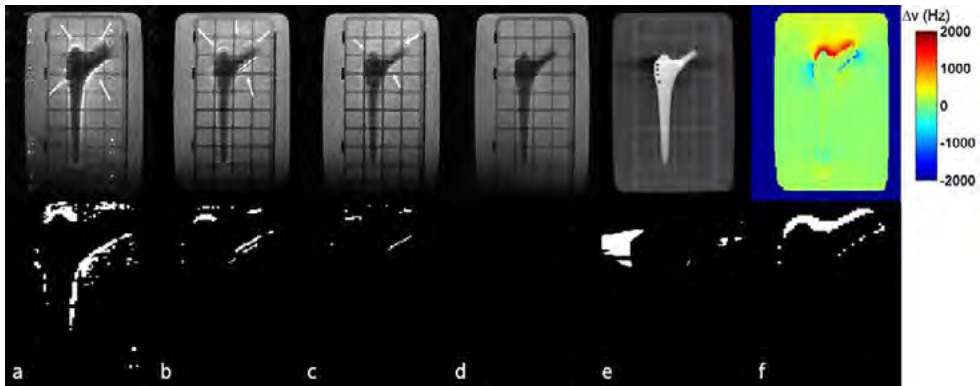
Figure 2.3: MRI and CT images of the titanium femoral stem of a hip implant. A 3D-SE image (a, BW_read=0.5Hz/pixel), ms3D-SE images (b, BW_read=0.5 kHz/pixel; c, BW_read=1 kHz/pixel), a 3D-PE-SE image at the echo time point (d), a reformatted CT image (e) and a field offset map are shown (f). The 3D-SE (a) and 3D-PE-SE (d) images were obtained using the same broadband pulses. The bottom row highlights the hyperintense voxels in the MRI images (a-d), hypointense voxels in the CT image (e) and the voxels exceeding 1kHz off-resonance in the field offset map (e).

An increase in SNR could be achieved for 3D-PE-(T)SE by exploiting multiple acquired time points (Table 2.2) at the cost of increased T_2^* weighting. This was visualized by complex averaging of multiple points (Figure 2.4b,f), which led to signal loss near the implant, trading SNR for accuracy of the implant delineation and vice versa. In a region of interest with $\Delta v(x)=0$ the SNR was increased a factor 3 for 3D-PE-SE (82 vs 250) data (Figure 2.4c-d) and a factor 2 for 3D-PE-TSE (39 vs 79) data (Figure 2.4g-h) by spectrally resolving the images. The 3D-PE-TSE data contained four times fewer time points when compared to 3D-PE-SE (64 vs 16 time points) due to the trade-off between the minimum echo-spacing and the number of acquired time points, resulting in a lower spectral resolution (500 Hz/bin vs 125 Hz/bin, Figure 2.4c,g). A sum-of-squares combination of the spectrally resolved images (Figure 2.4d,h) was able to increase the SNR in the image with only visible additional T_2^* weighting in regions with the strongest off-resonance effects, near the titanium implant.
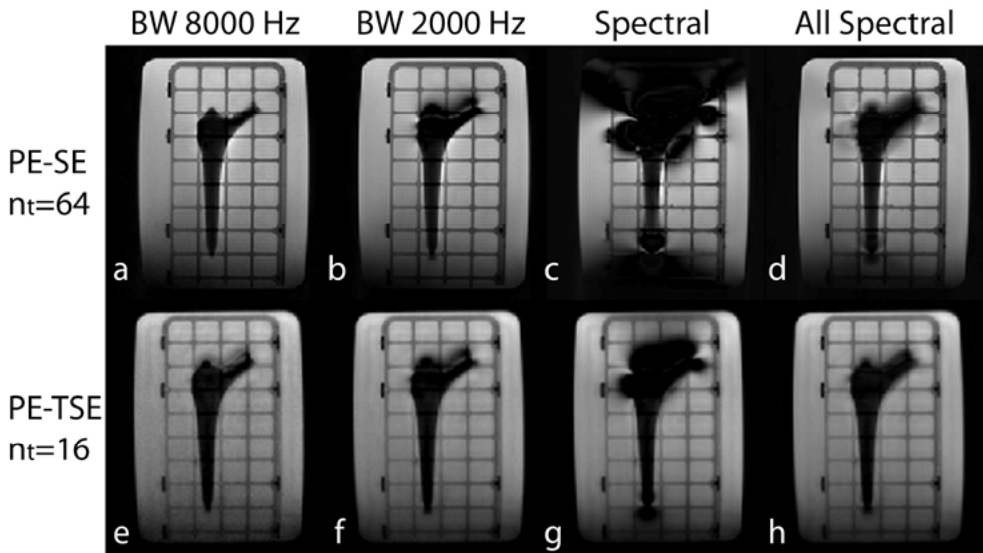
Figure 2.4: Temporally (a-b, e-f) and spectrally (c-d, g-h) resolved 3D-PE-SE (a-d) and 3D-PE-TSE (e-h) images reconstructed from the acquired signal. Magnitude images were obtained from the echo time point (a,e), 4 symmetrically sampled and complex averaged time points sampled around the echo (b,f), a single spectral bin of 125Hz (c) and 500 Hz (g) and a sum-of-squares combination of all spectral bins (d,h). The SNR of each image was noted in Table 2.2.

Table 2.2:
SNR estimates of magnitude images acquired in this work

Sequence	BW (Hz/pixel)	No. time points	SNR	Figure
3D-SE	505.7	-	30	-
3D-SE	1011.4	-	20	-
3D-mSE	505.7	-	29	2.3b
3D-mSE	1011.4	-	19	2.3c
3D-PE-SE	62.5	1	82	2.3d,2.4a
	31.3[a]	2	108	-
	15.6[a]	4	139	2.4b
3D-PE-TSE[b]	62.5	1	39	2.4e
	31.3[a]	2	47	-
	15.6[a]	4	59	2.4f
Spectrally resolved image[c]	Frequency (Hz/bin)	No. freq points	SNR[d]	
3D-PE-SE	125	1	250	2.4c
3D-PE-SE	125	64	244	2.4d
3D-PE-TSE	500	1	79	2.4g
3D-PE-TSE	500	16	82	2.4h

a) The acquisition BW was decreased retrospectively by complex averaging of individual time points.
b) A spherical shutter was used leading to a $\sqrt{2}$ decrease in SNR
c) Spectrally resolved images were obtained by applying a fourier transform over all time points.
d) SNR values of the spectrally resolved images are determined in an on-resonance ROI.

2.3.2 COMPRESSED SENSING ACCELERATED PHASE-ENCODED IMAGING IN VITRO

The fully sampled 3D-PE-SE data of the phantom experiments was used to determine a suitable acceleration factor for CS reconstruction by retrospective undersampling of all three phase encoding dimensions. The retrospectively reconstructed images of the titanium hip implant (Figure 2.5i) show that the geometrical accuracy of 3D-PE-SE was not affected by the undersampling factor (Figure 2.5i,b-f). However, increasing the undersampling factor led to increased blurring and loss of contrast in regions with low SNR (Figure 2.5i-ii, f). The reconstructed field offset maps (Figure 2.5iii) yielded very similar results for the presented undersampling factors (2-10) when compared to the field offset map obtained from the fully sampled data (Figure 2.5iii,a). From the retrospectively reconstructed images and error estimates (Table 2.3) it was inferred that an undersampling factor of six (Figure 2.5d) to eight (Figure 2.5e) may be expected to yield geometrically accurate magnitude images with acceptable loss of high frequency contrast when prospectively acquired.

The geometrical accuracy near the titanium implant in the fully sampled 3D-PE-SE image (Figure 2.6a) was similar to the prospectively accelerated acquisitions using only CS acceleration (Figure 2.6b), only TSE acceleration (Figure 2.6c) and combined CS-TSE acceleration (Figure 2.6d). The acquisition time was decreased a factor 6 (CS only), 20 (TSE),

and 60 (CS-TSE) compared to the fully sampled data. Both CS as well as TSE in itself caused blurring when qualitatively compared to fully sampled 3D-PE-SE, most likely related to undersampling of high spatial frequencies in combination with the total variation constraint in CS and to the T_2 weighting over k-space in TSE. However, the CS-TSE (Figure 2.6d) combination still results in a clear depiction of the grid lines and implant contour.
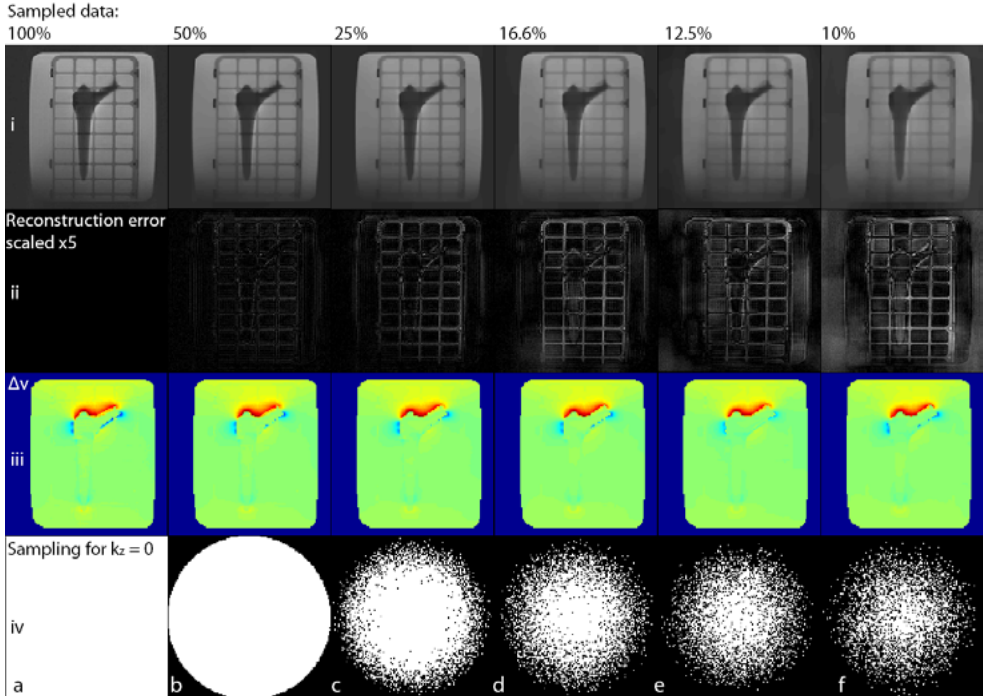

Figure 2.5: Retrospective CS reconstructed magnitude 3D-PE-SE images (i), the absolute reconstruction errors (ii, scaled x5) and CS reconstructed field offset maps (iii) are shown for undersampling factors of 2, 4, 6, 8 and 10 (b-f). The decreasing sampling density can be observed in the undersampling schemes for the middle z encoding (iv, $k_z = 0$).

Table 2.3:
CS reconstruction errors of magnitude images in Figure 2.5

Data (%)	NMSE	CC	Data (%)	NMSE	CC
50%	0.0012	0.997	12.5%	0.0057	0.983
25%	0.0025	0.992	10%	0.0126	0.976
16.6%	0.0048	0.986			

NMSE = normalized mean square error
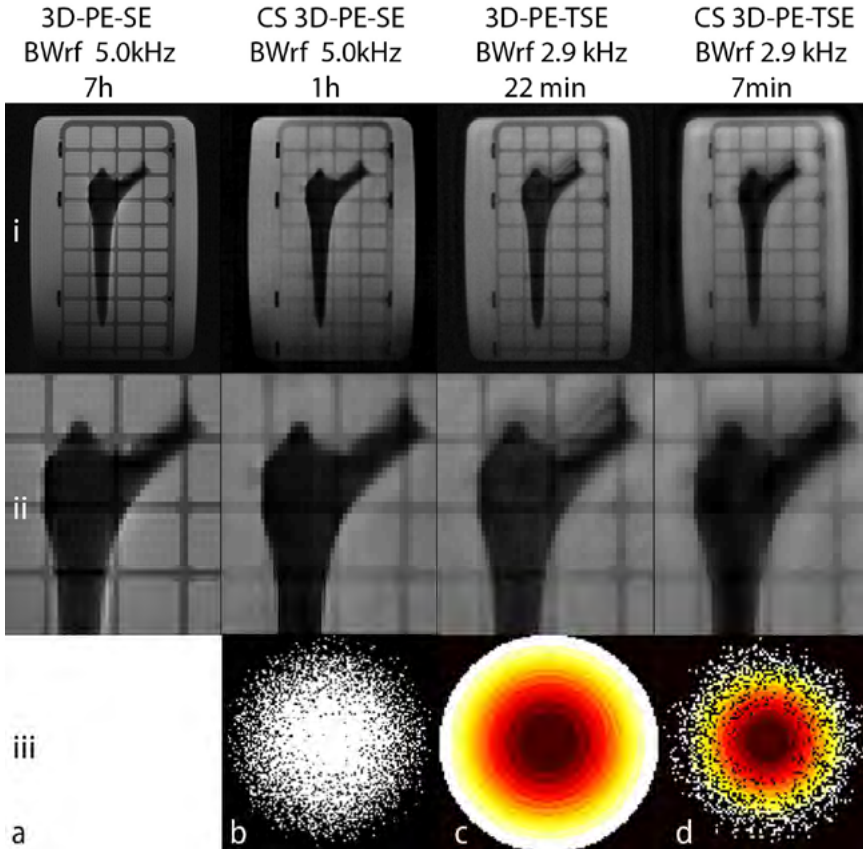CC = correlation coefficient

Figure 2.6: Coronal phase-encoded images of a titanium femoral stem of a hip implant (i), an enlarged region of the upper row (ii) and the corresponding sampling patterns at kz=0 (iii). A fully sampled 3D-PE-SE image (a), 6x prospective CS accelerated 3D-PE-SE image (b), a 3D-PE-TSE image with a spherical shutter (c) and a CS accelerated 3D-PE-TSE image (d) are shown. The indicated rf bandwidth refers to the bandwidth of the first refocusing pulse.

2.3.3 CS ACCELERATED 3D-PE-TSE IN VIVO

The feasibility of CS accelerated 3D-PE-TSE *in vivo* was demonstrated using a micro-coil setup to confine the coil sensitivity to the region of the knee containing the titanium screws. The placement of the micro-coil is indicated on 2D-TSE reference images (Figure 2.7a). The 3D-TSE acquisitions (Figure 2.7b,c) suffered from signal-pile up and geometrical distortions in the frequency encoding direction, which are indicated by arrows (Figure 2.7i,b-c). When comparing CS accelerated 3D-PE-TSE images (Figure 2.7d,e) to 3D-TSE images (Figure 2.7b,c) it becomes clear that signal pile-up and geometrical distortions caused by titanium induced off-resonance effects were successfully prevented. The CS-TSE acceleration decreased the acquisition time a factor 60 compared to a fully sampled 3D-PE-SE acquisition resulting in 20 and 10 minute scan times with a through-plane resolution of 1.25 and 2.5mm.
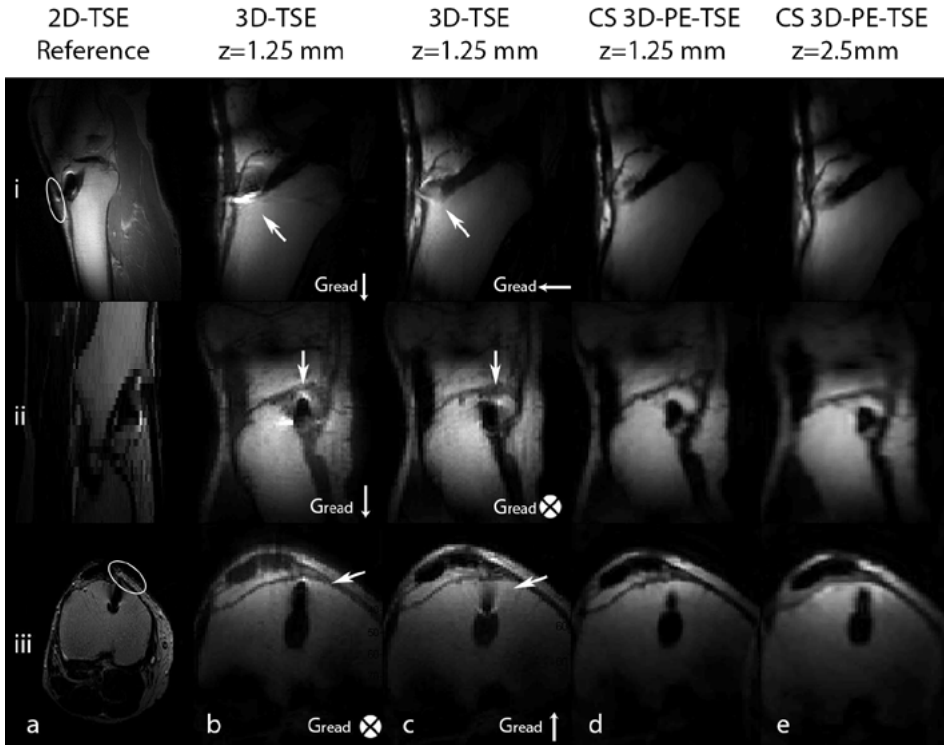
45

Figure 2.7: In vivo images near a titanium screw of 3D-TSE (b-c) and CS accelerated 3D-PE-TSE (d-e) sequences. The placement of the micro-coil is indicated on multi-slice TSE images (a i,iii). The 3D data was reformatted to sagittal (i), coronal (ii) and transversal (iii) images. The frequency encoding direction was changed between (b) and (c) and indicated at the bottom right of the images (b,c i-iii). Arrows indicate discernible geometrical distortions or signal pile-ups. CS accelerated 3D-PE-TSE images are shown for two different z encoding thicknesses (d,e).

2.4 DISCUSSION

In this work, CS accelerated 3D-PE-TSE was shown to obtain geometrically undistorted images in the presence of titanium objects in less than 10 minutes, which is an acceptable time frame for *in vivo* research purposes. The geometrical accuracy of fully sampled 3D-PE-SE was preserved despite the factor 60 scan time decrease by combining CS and TSE acceleration, albeit with some increase in blurring.

The 3D-PE-TSE sequence as proposed in this work was implemented on a clinical MR system by adapting a 3D turbo spin-echo spectroscopic imaging (TSE-SI) sequence. SI was used as a starting point, due to the obvious similarities between the desired sequence and a TSE-SI sequence, requiring minimal changes to data collection and spatial encoding. An advantage of this implementation is the flexibility to acquire an arbitrary number of time points,

resulting in a series of single point images. This property enabled reconstruction of undistorted field offset maps and retrospective sampling bandwidth adaptation by complex averaging of time points to retrospectively optimize the SNR. Moreover, when fitting the time series of undistorted images to an appropriate multiparameter signal model, full advantage can be taken of the spectroscopic nature of the proposed imaging method, facilitating mapping of valuable tissue parameters including the proton density, water-fat fractions and relaxation rates, depending on the need of the clinician and the applied signal model (20,26,29-31).

In this work, the geometric properties of broadband 3D PE-TSE imaging were compared to conventional and multispectral frequency encoded methods to qualitatively assess the potential benefit of fully phase-encoded techniques on clinical MR systems. While the multispectral frequency encoded images in this work significantly decreased the geometrical distortions compared to conventional methods, both signal pile-up and signal voids were still present near strong local gradients, which is to be expected when relying on frequency encoding processes (16). The 3D-PE-TSE images were free of such distortions, even when using high excitation bandwidths. This may prove to be beneficial when imaging near cobalt chromium or stainless steel implants that are often used in hip, knee and shoulder replacements. However, the susceptibility induced off-resonance effects caused by these materials are significantly larger than titanium, requiring higher bandwidths (>15 kHz) than used in this work. Such a frequency range might be covered using low flip angle broadband phase-encoded methods, such as in traditional SPI (19), or by the development of a multispectral 3D-PE-TSE approach. In addition to remaining image distortions, the small but unknown shift of the image center related to the choice of a reference frequency f_0 (26) will remain present when using frequency encoded methods, which is of particular importance for image guided therapies (2,32). In the 3D-PE-TSE sequence no distortions are present by definition, potentially enabling the use of MRI as a stand-alone modality for image guidance.

As a first step, the feasibility to apply CS for acquisition time reduction was assessed. The point by point sampling of the entire k-space in 3D-PE-TSE allowed for significant CS acceleration in three dimensions as was demonstrated for two different cases. The chosen CS reconstruction parameters performed well for the data presented in this work, but should be tested for specific cases to prevent loss of low contrast features. Further case specific optimization can be potentially achieved by including pre-knowledge in the sampling pattern design and image reconstruction. An interesting aspect of CS, as illustrated in this work, is the fact that CS is flexible with respect to the coil setup, as can be observed from the six-fold prospective acceleration using both a single and multi-element coil setup. This kind of aggressive acceleration would be unfeasible when using parallel imaging (PI) in combination with a small number of receive coils, since the number of coil elements and their orientation determines the achievable acceleration factor (33,34). The use of

low-element coil setups (i.e. micro-coils, surface coils) to limit the coil sensitivity profile and consequently the imaging matrix can be particularly beneficial to reduce the acquisition time of phase-encoded imaging, knowing that each point in k-space requires a separate phase encoding step and consequently an additional repetition. By carefully positioning surface coils the sensitivity profile of the receive coils can be limited to the volume of interest, thereby decreasing the volume to be encoded and consequently the required number of phase encoding steps to prevent aliasing.

The decrease in SNR associated with k-space undersampling may complicate successful CS reconstruction. Fortunately, as opposed to frequency encoding, in phase-encoded imaging it is possible to adjust the sampling time (1/BW) to increase the SNR without introducing geometrical distortions. Note, however, that the maximum sampling time is limited by intravoxel dephasing related to macroscopic field inhomogeneities. In this work, a deliberate choice was made for the sampling rate to ensure a minimal effect of signal dephasing during sampling of a single time point, while retaining sufficient SNR to combine reduced field of view imaging with undersampling. By exploiting both aspects it was feasible to obtain 3D-PE-TSE images of a titanium screw *in vivo* within 10 minutes with a reasonable resolution. In case multiple coils are present, it may be expected that PI and CS can be combined to further accelerate the proposed method, since they are based on different principles. However, additional acceleration of a CS-PI combination is likely to be modest (28).

In conclusion, this work has shown that it is feasible to use CS accelerated 3D-PE-TSE imaging to obtain geometrically accurate MR images in the presence of strong field inhomogeneities on a clinical MR system within a reasonable scan time.

REFERENCES

1. Khoo VS, Dearnaley DP, Finnigan DJ, Padhani A, Tanner SF, Leach MO. Magnetic resonance imaging (MRI): considerations and applications in radiotherapy treatment planning. Radiother Oncol 1997;42(1):1-15.

2. Crijns SP, Bakker CJ, Seevinck PR, de Leeuw H, Lagendijk JJ, Raaymakers BW. Towards inherently distortion-free MR images for image-guided radiotherapy on an MRI accelerator. Phys Med Biol 2012;57(5):1349-1358.

3. Kapanen M, Collan J, Beule A, Seppala T, Saarilahti K, Tenhunen M. Commissioning of MRI-only based treatment planning procedure for external beam radiotherapy of prostate. Magn Reson Med 2013;70(1):127-135.

4. Seevinck PR, de Leeuw H, Bos C, Bakker CJ. Highly localized positive contrast of small paramagnetic objects using 3D center-out radial sampling with off-resonance reception. Magn Reson Med 2011;65(1):146-156.

5. Kim Y, Muruganandham M, Modrick JM, Bayouth JE. Evaluation of artifacts and distortions of titanium applicators on 3.0-Tesla MRI: feasibility of titanium applicators in MRI-guided brachytherapy for gynecological cancer. Int J Radiat Oncol Biol Phys 2011;80(3):947-955.

6. Cepek J, Chronik BA, Fenster A. The effects of magnetic field distortion on the accuracy of passive device localization frames in MR imaging. Med Phys 2014;41(5):052301.

7. Sumanaweera TS, Adler Jr JR, Napel S, Glover GH. Characterization of spatial distortion in magnetic resonance imaging and its implications for stereotactic surgery. Neurosurgery 1994;35(4):696-704.

8. Zhang B, MacFadden D, Damyanovich A, Rieker M, Stainsby J, Bernstein M, Jaffray D, Mikulis D, Ménard C. Development of a geometrically accurate imaging protocol at 3 Tesla MRI for stereotactic radiosurgery treatment planning. Phys Med Biol 2010;55(22):6601.

9. Gnannt R, Chhabra A, Theodoropoulos JS, Hodler J, Andreisek G. MR imaging of the postoperative knee. J Magn Reson Imaging 2011;34(5):1007-1021.

10. Hayter CL, Koff MF, Potter HG. Magnetic resonance imaging of the postoperative hip. J Magn Reson Imaging 2012;35(5):1013-1025.

11. Haacke EM, Brown RW, Thompson MR, Venkatesan R. Magnetic resonance imaging: Wiley-Liss New York:; 1999.

12. Cho Z, Kim D, Kim Y. Total inhomogeneity correction including chemical shifts and susceptibility by view angle tilting. Med Phys 1988;15:7.

13. Koch KM, Lorbiecki JE, Hinks RS, King KF. A multispectral three-dimensional acquisition technique for imaging near metal implants. Magn Reson Med 2009;61(2):381-390.

14. Lu W, Pauly KB, Gold GE, Pauly JM, Hargreaves BA. SEMAC: slice encoding for metal artifact correction in MRI. Magn Reson Med 2009;62(1):66-76.

15. Jezzard P, Balaban RS. Correction for geometric distortion in echo planar images from B0 field variations. Magn Reson Med 1995;34(1):65-73.

16. Koch KM, King KF, Carl M, Hargreaves BA. Imaging near metal: the impact of extreme static local field gradients on frequency encoding processes. Magn Reson Med 2014;71(6):2024-2034.

17. Koch K, Brau A, Chen W, Gold G, Hargreaves B, Koff M, McKinnon G, Potter H, King K. Imaging near metal with a MAVRIC-SEMAC hybrid. Magn Reson Med 2011;65(1):71-82.

18. Carl M, Koch K, Du J. MR imaging near metal with undersampled 3D radial UTE-MAVRIC sequences. Magn Reson Med 2013;69(1):27-36.

19. Emid S, Creyghton J. High resolution NMR imaging in solids. Physica B+ C 1985;128(1):81-83.

20. Artz NS, Hernando D, Taviani V, Samsonov A, Brittain JH, Reeder SB. Spectrally resolved fully phase-encoded three-dimensional fast spin-echo imaging. Magn Reson Med 2014;71(2):681-690.
21. Donoho DL. Compressed sensing. IEEE Trans Inf Theory 2006;52(4):1289-1306.
22. Tsaig Y, Donoho DL. Extensions of compressed sensing. Signal Process 2006;86(3):549-571.
23. Lustig M, Donoho D, Pauly JM. Sparse MRI: The application of compressed sensing for rapid MR imaging. Magn Reson Med 2007;58(6):1182-1195.
24. Schenck JF. The role of magnetic susceptibility in magnetic resonance imaging: MRI magnetic compatibility of the first and second kinds. Med Phys 1996;23(6):815-850.
25. Alsop DC. The sensitivity of low flip angle RARE imaging. Magn Reson Med 1997;37(2):176-184.
26. Bakker CJ, de Leeuw H, van de Maat GH, van Gorp JS, Bouwman JG, Seevinck PR. On the utility of spectroscopic imaging as a tool for generating geometrically accurate MR images and parameter maps in the presence of field inhomogeneities and chemical shift effects. Magn Reson Imaging 2013;31(1):86-95.
27. Henkelman RM. Measurement of signal intensities in the presence of noise in MR images. Med Phys 1985;12(2):232-233.
28. Liu F, Duan Y, Peterson BS, Kangarlu A. Compressed sensing MRI combined with SENSE in partial k-space. Phys Med Biol 2012;57(21):N391-403.
29. Rioux JA, Brewer KD, Beyea SD, Bowen CV. Quantification of superparamagnetic iron oxide with large dynamic range using TurboSPI. J Magn Reson 2012;216:152-160.
30. Van Gorp JS, Crijns SPM, Bouwman JG, Raaymakers BW, Bakker CJG, Seevinck PR. Compressed sensing accelerated spectroscopic imaging to obtain geometrically accurate water-fat images and field maps in MR guided interventions. Proc 20th Annual Meeting ISMRM, Melbourne 2012:202.
31. Bakker CJG, van Gorp JS, Verwoerd JL, Westra AH, Bouwman JG, Zijlstra F, Seevinck PR. Multiple single-point imaging (mSPI) as a tool for capturing and characterizing MR signals and repetitive signal disturbances with high temporal resolution: The MRI scanner as a high-speed camera. Magn Reson Imaging 2013;31(7):1037-1043.
32. Lagendijk JJ, Raaymakers BW, Raaijmakers AJ, Overweg J, Brown KJ, Kerkhof EM, van der Put RW, Hårdemark B, van Vulpen M, van der Heide UA. MRI/linac integration. Radiother Oncol 2008;86(1):25-29.
33. Pruessmann KP, Weiger M, Scheidegger MB, Boesiger P. SENSE: sensitivity encoding for fast MRI. Magn Reson Med 1999;42(5):952-962.
34. Griswold MA, Jakob PM, Heidemann RM, Nittka M, Jellus V, Wang J, Kiefer B, Haase A. Generalized autocalibrating partially parallel acquisitions (GRAPPA). Magn Reson Med 2002;47(6):1202-1210.

MULTISPECTRAL 3D PHASE-ENCODED TURBO SPIN-ECHO FOR IMAGING NEAR METAL: LIMITATIONS AND POSSIBILITIES

ABSTRACT

In this work the imaging performance of a multispectral fully phase-encoded turbo spin-echo (ms3D-PE-TSE) sequence for imaging near metal was assessed based on the artifact reduction capabilities, scan time efficiency and signal characterization properties.

For this purpose, ms3D-PE-TSE and ms3D-TSE sequences were implemented to obtain multispectral images (±20 kHz) of a cobalt-chromium (CoCr) knee implant embedded in agarose. In addition, a knee implant computer model was used to investigate the possibilities for scan time acceleration using field-of-view (FOV) reduction for the individual off-resonance frequency bins. Experimental confirmation was obtained for a +10 kHz frequency bin with and without compressed sensing acceleration.

The obtained ms3D-PE-TSE images showed no susceptibility related artifacts, while ms3D-TSE images suffered from hyper-intensity artifacts and signal voids. The limitations of ms3D-TSE were apparent in the far off-resonance regions (±10 - 20 kHz) located close to the implant. The scan time calculations showed that ms3D-PE-TSE can be applied in a clinically relevant timeframe (~12min), when omitting the three central frequency bins. The feasibility of the calculated acceleration factors was demonstrated by decreasing the scan time for the +10 kHz frequency bin from ~10.9 min to ~3.5 min, while also increasing the spatial resolution fourfold, by combining reduced FOV imaging and compressed sensing. The temporally resolved signal of ms3D-PE-TSE proved to be useful to decrease the intensity ripples after sum-of-squares reconstructions, increasing the signal-to-noise ratio and detection of the echo-formation near metal implants.

The presented results suggest that the scan time limitations of ms3D-PE-TSE can be sufficiently addressed when focusing on signal acquisitions in the direct vicinity of metal implants. Because these regions cannot be measured with existing multispectral methods, the presented ms3D-PE-TSE method may enable accurate detection of inflammation, (pseudo-)tumors or metallic debris in locations close to the implant.

3.1 INTRODUCTION

Surgical orthopedic procedures, such as knee and hip replacements (1,2), have been steadily increasing in recent years due to increasing life expectancy and improved clinical capabilities. With the increasing number of metal implants, there is a growing need for accurate post-operative imaging. Ideally, the soft-tissue contrast of MRI is exploited for the detection of complications (3-8) (e.g. osteolysis, infection, implant loosening, pseudo-tumors) (9,10) near metal implants.

To accurately perform post-operative MRI, multispectral turbo spin-echo (msTSE) techniques (e.g. MAVRIC, SEMAC) have been developed for metal artifact reduction caused by the paramagnetic nature of the implants (5,6,11). To a large extent these methods have been successful in improving the diagnostic image quality surrounding metal implants. However, in the case of extreme susceptibility induced field gradients, equal or larger than the frequency encoding readout gradient, such techniques still result in signal hyper-intensities and signal voids (12). In a recent study it was calculated that multispectral techniques are fundamentally limited in regions close to the implants where metal induced off-resonance offsets exceed ±12 kHz, when applied as in the clinic (13).

To overcome these remaining fundamental limitations, fully phase-encoded techniques have been suggested (14-16). These techniques result in geometrically undistorted images, while also acquiring a densely sampled temporal signal decay curve that can be exploited for detailed signal decay characterization. The main limitation of these sequences is the inherently long acquisition time, requiring significant scan time acceleration before clinical application is feasible. In recent studies, both parallel imaging (14) and compressed sensing (15) have been combined with phase-encoded turbo spin-echo sequences to reduce the scan time of phase-encoded MRI techniques under 10 minutes for a single measurement. The peak B_1 requirements in 3D phase-encoded turbo spin-echo (3D-PE-TSE) acquisitions, however, limit the achievable refocusing bandwidth in a single acquisition to ~3 kHz after bandwidth optimization (15). This results in incomplete signal excitation when imaging near strong paramagnetic alloys (i.e. cobalt-chromium, stainless steel).

In order to obtain 3D-(PE-)TSE images from a larger frequency range than the achievable rf refocusing bandwidth, multispectral excitation schemes are required (5,6). Methods that utilize these multispectral excitation schemes, such as MAVRIC and SEMAC, cover the desired frequency range by repeating the imaging experiment with different rf offset frequencies. Coverage of the desired frequency range requires multiple 3D-PE-TSE acquisitions and dedicated multispectral excitation schemes (5,17) that will significantly increase the scan time.

To address scan time issues in ms3D-PE-TSE, both the number of required acquisitions as the number of phase encoding steps in each acquisition should be considered. By optimizing the refocusing bandwidth and the step size between rf pulses, it is possible to reduce the

required number of acquisitions, while the scan time of the individual acquisitions can be reduced by adjusting the field-of-view (FOV) based on the excited signal locations. In the case of orthopedic implants the off-resonance signal is located close to the metal components of the implant, allowing for FOV reduction without introducing aliasing artifacts. Such time-saving FOV reductions have already been applied successfully for the MAVRIC sequence in two phase-encoded dimensions (5), while a FOV reduction in three dimensions might be possible for 3D phase-encoded imaging.

To assess the potential of multispectral 3D phase-encoded turbo spin-echo (ms3D-PE-TSE) for clinical applications requires a better understanding of the artifact reduction capabilities and scan time limitations. Currently, the frequency coverage of multispectral methods is restricted to ± 8 - 12 kHz, because the extreme susceptibility gradients outside this range prevent accurate spatial encoding with frequency-encoded methods. Phase-encoded methods, however, are in principle unaffected by the extreme metal induced susceptibility gradients at these frequencies. To compare the artifact reduction capabilities of multispectral frequency-encoded and phase-encoded methods it is necessary to include off-resonance frequency bins that are excited with rf offsets larger than ± 12 kHz.

In the study reported here, the primary goal was to identify if multispectral 3D phase-encoded turbo-spin-echo (ms3D-PE-TSE) can add value to existing multispectral 3D-TSE (ms3D-TSE) methods based on artifact reduction, scan times and signal characterization. For this study, a cobalt-chromium (CoCr) knee implant phantom and a CoCr knee implant computer model were used to study the imaging performance using a paramagnetic material that is often encountered in orthopedic imaging. First, ms3D-TSE and ms3D-PE-TSE sequences were implemented by designing multispectral excitation schemes using rf pulses with the same shapes, allowing a fair comparison between both methods. Both sequences were used to obtain multispectral images of the CoCr phantom from an extended frequency range of ± 20 kHz for comparison of the artifact reduction capabilities. Second, the knee implant computer model was used to calculate the susceptibility induced field shift from the implant. The field shifts were used to determine the locations where the spatial encoding process of frequency-encoded imaging is expected to be fundamentally limited and to calculate the achievable FOV reduction factors in ms3D-PE-TSE. The calculated scan time values were experimentally confirmed in a second experiment by using reduced FOV imaging with and without additional compressed sensing (CS) acceleration (15,18). The temporal signal of the phase-encoded techniques was exploited during data analysis (i.e. SNR adjustments, adjusting T_2^* weighting), and for signal characterization in the presence of the CoCr implant.

3.2 METHODS

3.2.1 IMPLEMENTATION OF MULTISPECTRAL IMAGING SEQUENCES

To facilitate a fair comparison between multispectral frequency-encoded imaging and multispectral phase-encoded imaging, ms3D-TSE and ms3D-PE-TSE sequences were implemented using similar pulse shapes on a clinical MRI system. The slice selection gradients were disabled in all sequences to exclude slice related artifacts in the data and prevent mixing of slice distortions and frequency encoding related artifacts. The details of the original 3D-PE-TSE sequence are described in (15).

To implement a multispectral excitation scheme with a uniform intensity profile over the full multispectral frequency range it is necessary to first choose a pulse pair and then determine the rf step size that result in the lowest intensity variation after combination of all frequency bins. For ms3D-PE-TSE the time-efficiency is the most important aspect to take into account when choosing the rf pulse pair. To maximize the time-efficiency of ms3D-PE-TSE both a high rf bandwidth and short durations for the refocusing pulse are desired. In light of these criteria we chose to combine a 2.016 ms sinc-gauss excitation pulse with a 0.3456 ms block refocusing pulse to obtain a truncated sinc frequency profile with a FWHM of ~3 kHz (17). In case of ms3D-TSE 2.91 ms sinc-gauss and 0.5 ms block pulses were used to decrease the rf bandwidth to ~2 kHz, limiting the maximum signal displacement to ±1 pixel for a gradient strength of 1 kHz/pixel (according to x'- x = $\Delta v_0(x)$ $2\pi/\gamma G_{read}$).

After choosing the pulse-pair, the rf step sizes (Δf) with the lowest intensity variations after sum-of-squares combination were determined using 1D Bloch simulations (19). First, the actual frequency profiles of the ms3D-TSE and ms3D-PE-TSE the pulse-pairs were simulated for a [-20:0.02:20] kHz range with 100 µs time steps (code available on http://www-mrsrl.stanford.edu/~brian/bloch/). Second, the signal response over the total frequency range was determined by combining multiple rf frequency responses with a varying rf step sizes Δf of [1.0:0.01:3.0] kHz, followed by a sum-of-squares combination for each Δf. The Δf values with the most uniform signal response were selected (Figure 3.1).

3.2.2 MAGNETIC FIELD SIMULATIONS

A 3D vectorized computer model of the femoral component of a knee implant (Smith & Nephew, UK) was used to calculate the susceptibility induced field distribution at 1.5T and 3T (20,21). First, the 3D vector model was converted to a discrete susceptibility distribution ($d\chi_{CoCrMo}$ = 1300 ppm (22)) in a grid coordinate system (FOV = 128^3 mm^3, voxel = 0.25^3 mm^3). The expected field shift was calculated using efficient forward 3D field calculations. Based on these calculations, all voxels with a calculated frequency value within the routinely applied frequency range of ±12 kHz were selected to detect the rf limited regions in current ms3D-TSE methods (Figure 3.2).

3.2.3 REDUCED FIELD-OF-VIEW IMAGING

The off-resonant frequency bins in the ms3D-PE-TSE acquisitions for near metal imaging may often be acquired with a reduced FOV compared to on-resonant acquisitions, because the off-resonance signal is located in proximity to the implant. To determine the scan time reduction factor for a typical metal implant, such as used in this work, it is possible to exploit magnetic field simulations, such as described earlier. To calculate the minimal required FOV for each frequency bin, all voxels with a frequency value within the rf bandwidth (±2.56 kHz, >1% rf frequency response) centered around the rf center frequencies (f = -21.4:3.1:+21.4 kHz) were selected from the simulated field distributions. After selecting the voxels at a specific frequency, a bounding box was determined that contained all signal, representing the minimal required FOV to prevent aliasing. Based on the size of the box and a 2x2x2 mm MR acquisition resolution it was possible to calculate the scan matrix and the number of required repetitions (N_xxN_yxN_z) for each specific off-resonance 3D-PE-TSE acquisition. The FOV reduction factors (rFOV/FOV) were calculated for all phase-encoded dimensions, and combined with earlier reported scan time reduction factors (14,15) to calculate the minimal scan time per bin. The principle of rFOV imaging was visualized for three off-resonance bins (f = -3.1 kHz, +3.1 kHz, +9.2 kHz) by projecting the signal within the specified rf BW over the implant model (imoverlay code available on http://www.mathworks.com/matlabcentral/fileexchange/42904-imoverlay).

3.2.4 EXPERIMENTAL SETUP

The femoral part of a CoCr knee implant (Smith & Nephew, UK) was embedded in 2% agarose gel in a cylindrical container (radius = 5 cm , length = 10 cm). All imaging experiments were performed on a 1.5T MRI system (Philips Achieva, Best, The Netherlands) with an eight element knee coil.

In the first experiment, the goal was to compare the artifact reduction performance of frequency-encoded and phase-encoded sequences for a ±20 kHz frequency range. To this end, ms3D-PE-TSE and ms3D-TSE images were acquired by stepping the rf frequencies with 2.5 kHz and 1.2 kHz to cover a frequency range of ±20 kHz and ±20.4 kHz, respectively. All 3D-PE-TSE acquisitions were performed with a 3D spherical k-space shutter in order to reduce the acquisition time twofold. To minimize artifacts in the readout direction for ms3D-TSE, the maximum frequency encoding strength was applied. The frequency bins were acquired individually (appendix) before combining them into a single dataset with a sum-of-squares reconstruction.

In a second experiment, the possibility for rFOV 3D-PE-TSE imaging was investigated. First, on-resonance (0 kHz) and off-resonance 3D-TSE images (+10 kHz) were acquired for planning of the rFOV acquisitions. Second, 3D-PE-TSE data was acquired at the +10 kHz frequency with a reduced FOV (90x100x68 mm) but with an increased spatial resolution

(1.25x1.56x2 mm) in a similar scan time as the full FOV experiment (FOV = 128x128x128 mm; voxel size 2x2x4 mm). To demonstrate the potential of k-space undersampling strategies for scan time acceleration, CS was combined with rFOV to obtain an additional factor 3 acceleration of the 3D-PE-TSE acquisition as described in (15). To enable qualitative comparison between scans, the acquired 3D-PE-TSE data was reconstructed to the same grid as the 3D-TSE data (dz = 4 mm, FOV = 128x128x128 mm).

3.2.5 ACQUISITION PARAMETERS

Experiment 1:

ms3D-TSE: BW_{read} = 113 kHz (maximum), TE = 9ms, TR = 180ms, FOV = 128x128x128 mm, voxel size = 1x2x4 mm, turbo factor = 10, f_0 = [-20.4:1.2:+20.4 kHz], 36 sec per bin, 21 min in total.

ms3D-PE-TSE: BW_{acq} = 32 kHz, nt = 64, TE = 9 ms, TR = 100 ms, FOV = 128x128x128 mm, voxel size = 2x2x4 mm, turbo factor = 10, f_0 = [-20:2.5:+20 kHz], 10 min 55 sec per bin, 3 h 9 min in total.

Experiment 2:

3D-TSE (2x): BW_{read} = 113 kHz (maximum), TE = 9ms, TR = 180ms, FOV = 128x128x128 mm, voxel size = 1x2x4 mm, turbo factor = 10, 36 sec per bin, f_0 = [0 kHz; +10 kHz].

rFOV3D-PE-TSE (2x): BW_{acq} = 32 kHz, nt = 32, TE = 9 ms, TR = 100ms, FOV = 90x100x68 mm, voxel size = 1.25x1.56x2 mm, turbo factor = 10, f_0 = +10 kHz, 10 min 55 sec with shutter only and 3 min 38 sec with shutter and 3x CS acceleration.

3.2.6 TEMPORALLY RESOLVED SIGNAL IN PHASE-ENCODED IMAGING

Each 3D-PE-TSE dataset contains a series of single point images with varying T_2^* weighting, due to the absence of a readout gradient (16). The echo times obtained during the sampling interval (T_{acq}) of the consecutive images are given by TE(n)=TE+(n-0.5N_t-1)dt, with dt = 0.03125 ms, N_t=256, n=1:N_t using a 32 kHz BW. In this work the echo time series was initially used to retrospectively adjust the bandwidth by complex averaging of multiple time points. Averaging of multiple time points increases the SNR of the individual bins, but also increases the T_2^* weighting (15). In the reconstructed images this effect can result in signal voids at locations with very short T_2^* values, which is therefore often an undesired property. However, if the overlap between bins is sub-optimal the T_2^* weighting might be used to our advantage. By varying the T_2^* weighting before sum-of-squares combination it is possible to alter the bin overlap and potentially decrease variations in the overall image intensity after sum-of-squares combination. Finally, the signal was used to investigate the effect of strong susceptibility gradients on the temporal signal decay. The individual time points of the temporally resolved signals were combined for all frequency bins in a single temporally resolved signal using a sum-of-squares reconstruction. This was done on a pixel-by-pixel

basis to obtain a 4D multispectral dataset with three spatially encoded dimensions and a temporally resolved signal. The signal was used to visualize the influence of metal induced gradients on the echo-formation.

3.3 RESULTS

3.3.1 RF PROFILES

Bloch simulations of the rf pulse pairs were performed to determine the rf step size (Δf) leading to the lowest intensity variation for a multispectral excitation scheme (Figure 3.1). The simulations of the excitation (Figure 3.1a,f) and refocusing pulse-pair (Figure 3.1b,g) led to a uniform truncated sinc frequency response profile as desired for multispectral imaging (Figure 3.1c,h). After sweeping the Δf step size and combining the individual bins with a sum-of-squares reconstruction we found two Δf settings with minimal signal intensity variation. The lowest intensity ripples were observed for Δf = 1.16 kHz in ms3D-TSE (Figure 3.1d) and Δf = 1.74 kHz in ms3D-PE-TSE (Figure 3.1i), while a second near optimal setting was found for 2.04 kHz (Figure 3.1e) and 3.06 kHz (Figure 3.1j), respectively. The two Δf values represent a trade-off between the required number of scans to excite the total frequency range and the remaining intensity ripples in the final reconstructed sum-of-squares image. Furthermore, the total signal amplitude of the sum-of-squares signal is lower for the larger step sizes of 2.04 kHz (Figure 3.1e) and 3.06 kHz (Figure 3.1j), because of the decreased overlap between individual frequency bins.
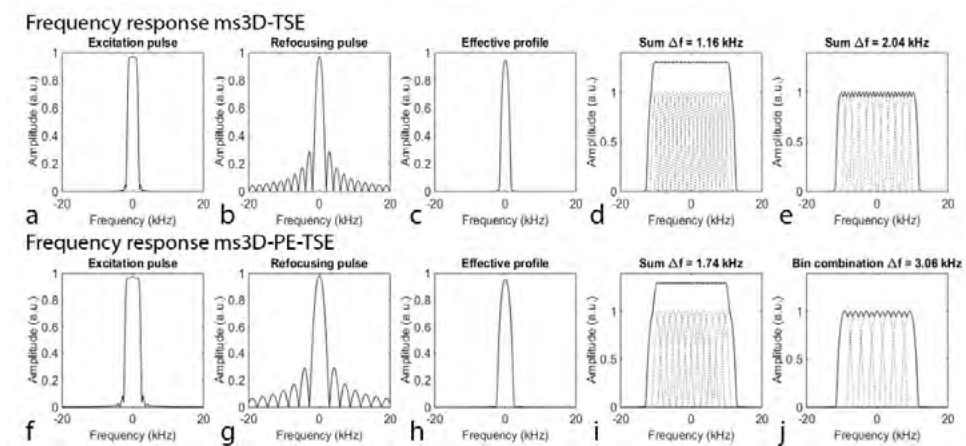

Figure 3.1: The simulated frequency responses for both multispectral 3D-TSE (a-e) and 3D-PE-TSE excitation (a,f) and refocusing (b,g) pulses as implemented in this study. The effective refocusing pulse profile of a single pulse pair was calculated (c,h) and used for sum-of-squares signal combination for different step sizes (d-e, i-j).

3.3.2 FIELD CALCULATIONS

The frequency changes induced by the femoral part of the knee prosthesis (Figure 3.2i) were calculated for a field strength of 1.5T (Figure 3.2ii) and 3.0T (Figure 3.2iv). Images that included only signal within ±12 kHz were constructed to indicate the missing signal regions, where ms3D-PE-TSE can add the most value (Figure 3.2iii,v). To improve the visual assessment of all regions outside the ±12 kHz range, 3D renderings were performed for the implant (Figure 3.2di), the signal regions outside the ±12 kHz range (Figure 3.2dii,iv) and the combination of the two (Figure 3.2diii,v). It can be observed that these regions are all located close to the implant, with substantial signal voids at a higher field strength of 3T.
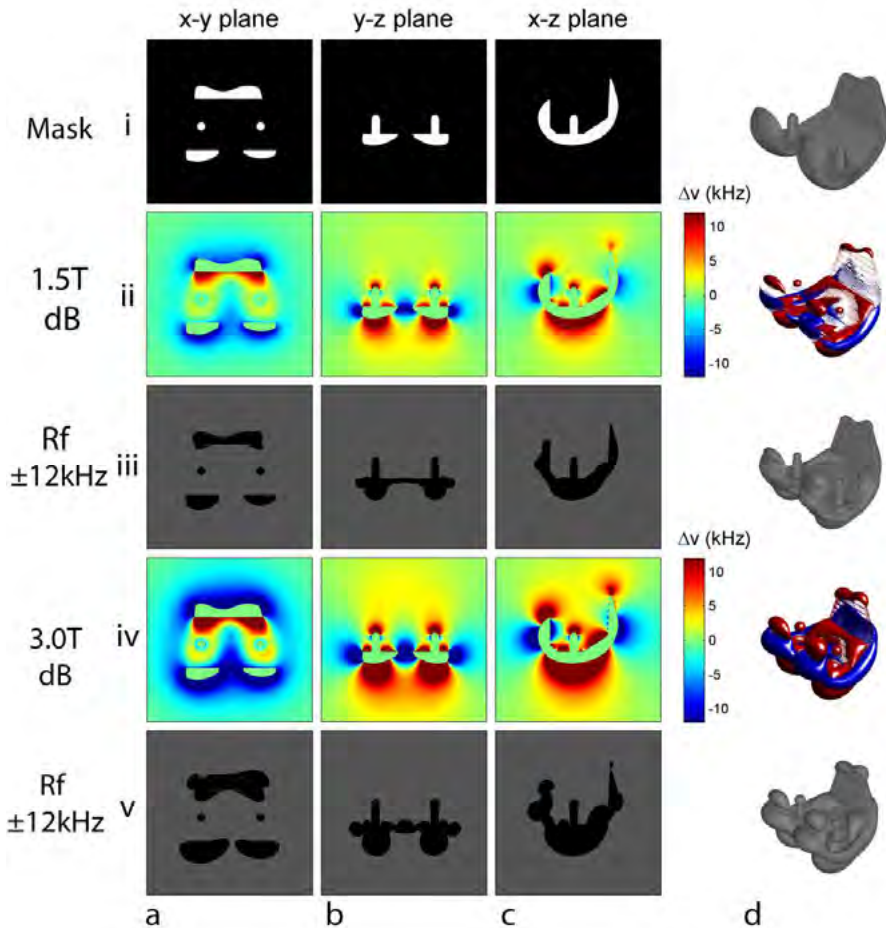
Figure 3.2: A digital model of the femoral component of a knee implant was used to create a mask (i) and calculate the field distribution induced at 1.5T (ii) and 3.0T (iv) (dχ = 1300 ppm) in three imaging planes (a-c). The regions where signal can be expected for a ±12 kHz rf excitation range were calculated (iii,v). 3D renderings of the implant are also shown (d), where the regions outside the rf excitation range were colored blue (dB<-12kHz) and red (dB>+12kHz)(ii-d,iv-d).

3.3.3 IMAGE ARTIFACT REDUCTION

The artifact reduction capabilities of ms3D-PE-TSE are demonstrated in Figures 3.3 and 3.4. In Figure 3.3 it can be observed that the signal pile-up artifacts (hyper-intensities) in ms3D-TSE (Figure 3.3a-b) were absent in ms3D-PE-TSE (Figure 3.3c-d). Broadening of the excited frequency range in ms3D-TSE from ±10 kHz (Figure 3.3a) to ±20 kHz (Figure 3.3b) led to an increase of these signal pile-up artifacts, while signal voids were still present in the vicinity of the implant. The ms3D-PE-TSE images showed more intensity ripples that are most likely related to sub-optimal overlap of the frequency bins (Figure 3.3c, BW = 32 kHz). This phenomenon was decreased by complex averaging of six time points per frequency bin prior to sum-of-squares combination (Figure 3.3d; BW = 5.3 kHz).
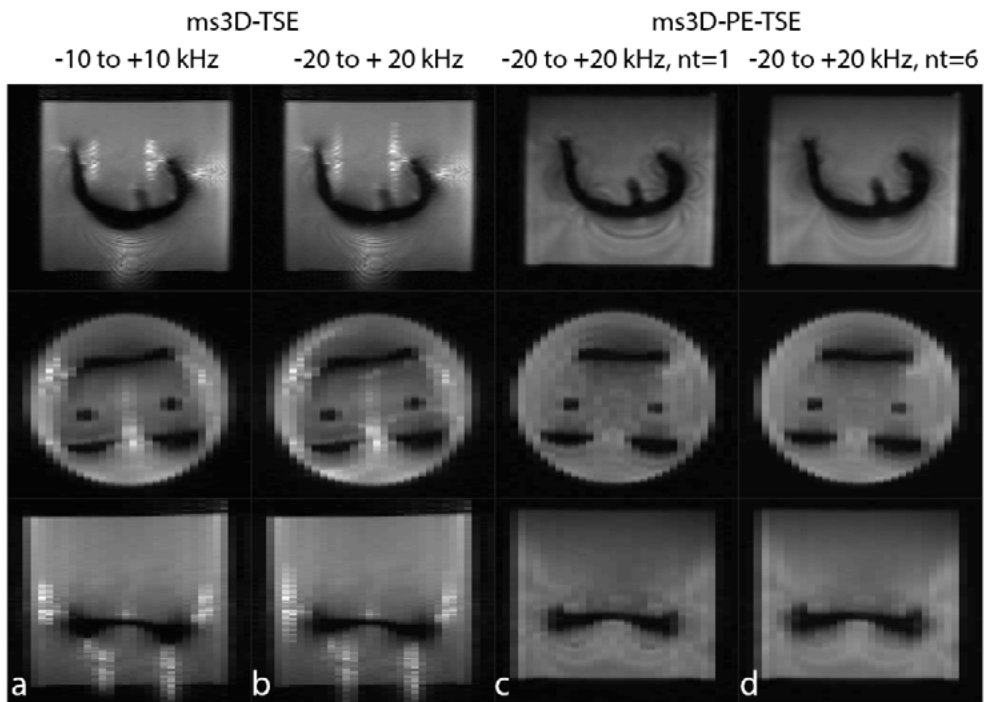
Figure 3.3: ms3D-TSE (a-b) and ms3D-PE-TSE (c-d) images with the rf offset range varied between -10 to +10 kHz (a) and -20 to +20kHz (c-d). The ms3D-PE-TSE images were reconstructed using the central time point at the echo (c) and 6 points symmetrically sampled around the echo (d).

The multispectral excitation range can be divided in far off-resonance regions, where frequency encoding is fundamentally limited, and the frequency range that is routinely excited with multispectral methods. The effect of fundamental limitations in frequency-encoded imaging was observed after splitting the entire frequency range of -20 kHz to +20 kHz in three sub-ranges: below -10 kHz (Figure 3.4a,d), between ±10 kHz (Figure 3.4b,e) and

above +10 kHz (Figure 3.4c,f). In the far off-resonance ms3D-TSE images it was difficult to distinguish hyper-intensity artifacts from correct spatially encoded signal (Figure 3.4a,c). This can potentially obscure clinically relevant information or lead to misinterpretation of the data when *in vivo* investigations are performed. These artifacts were observed at multiple locations near the metal implant after 3D rendering of the far off-resonance ms3D-TSE signal (Figure 3.4g,i). The ms3D-PE-TSE acquisitions did not show any hyper-intensity artifacts in the images (Figure 3.4d-f) or 3D renderings (Figure 3.4j-l). The location of the implant was easily detected with both sequences after 3D rendering of the signal void in the central ±10 kHz frequency range (Figure 3.4h,k).
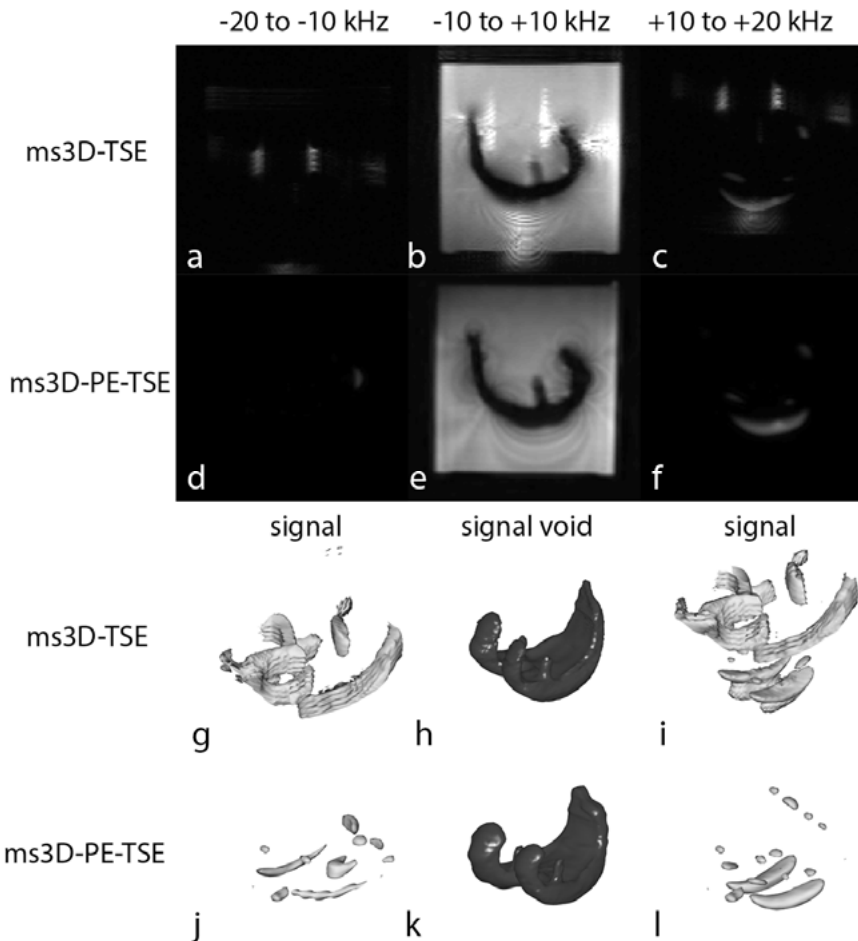
Figure 3.4: Comparison of ms3D-TSE (a-c, g-i) and ms3D-PE-TSE (d-f, j-l) data for the off-resonance regions -20 to -10 kHz (a,d), -10 to +10 kHz (b,e) and +10 to +20 kHz (c,f). The acquired signal for the far off-resonance bins was rendered in 3D to visualize the imaging differences between both sequences (-20 to -10 kHz, g,j, +10 to +20kHz, i,l). The signal void within the gel was rendered from the -10 to +10 kHz region (h,k) to obtain a rough estimate of the implant.

3.3.4 SCAN TIME REDUCTION

The possibilities for FOV reduction were visualized for rf excitation offsets of -3.1 kHz, 0 kHz, +3.1 kHz and +9.2kHz (Figure 3.5a-d). The minimal FOV that was required to prevent aliasing decreased with increasing rf excitation frequency offsets, with strong reductions in all three dimensions for larger frequency offsets (Figure 3.5e, Table 3.1). The calculated FOV reduction factors (rFOV/FOV) were mainly limited by the implant size for excitation frequencies exceeding ±6.1 kHz, and are therefore object specific. To acquire the total frequency range of ±20 kHz with ms3D-PE-TSE for the CoCr knee implant phantom would still require 82.5 min when applying the calculated rFOV factors for each frequency bin. The combination of rFOV imaging with k-space undersampling techniques (e.g. CS, SENSE) (14,15) might decrease the total acquisition time further to 27.5 min. Unfortunately, these scan times are still prohibitive for clinical use and require additional scan time reductions to be practical. As an alternative to acquiring the total frequency range, it is possible to omit the frequency bins where ms3D-TSE can be expected to efficiently capture signal. In doing so the ms3D-PE-TSE sequence would only be used to acquire off-resonance regions where fully phase-encoded imaging is the most beneficial. After omitting the three central bins (-3.1 kHz, 0 kHz, +3.1 kHz) a factor 2.5x reduction in acquisition time can be expected for ms3D-PE-TSE. Including this factor scan times of 35.7 min (without CS) or 11.9 min (with CS) can be obtained, where the latter would be sufficient to enable *in vivo* investigations.

In a second phantom experiment, the scan time reduction factors of Table 3.1 were confirmed for a frequency bin at +10 kHz. 3D-TSE images were acquired to perform planning (Figure 3.6a-b) of the rFOV 3D-PE-TSE measurements. The applied rFOV is indicated by a white box in Figure 3.6. In the off-resonance 3D-TSE image (Figure 3.6b), signal pile-up led to hyper-intensities and a decreased number of signal containing voxels, despite the strong readout BW of 113 kHz. No such artifacts were observed in the 16 kHz BW 3D-PE-TSE images (Figure 3.6c,e). The SNR and the T_2^* weighting of the 2 kHz BW images (Figure 3.6d,f) increased compared to the 16 kHz BW reconstruction, however, at the cost of a slightly
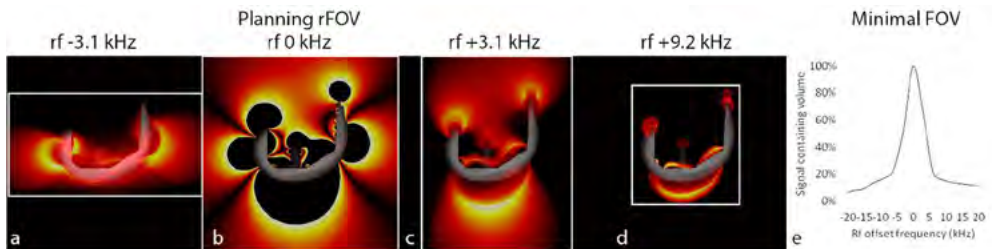
Figure 3.5: The FOV planning is indicated in white for -3.1 kHz (a), 0 kHz (b), 3.1 kHz (c) and 9.2 kHz (d) 3D-PE-TSE acquisitions. Through plane projections were made of the signal (color coded) for the off-resonance bins (a,c-d) to visualize all signal containing voxels in the 3D volume. In the on-resonance bin (b) a single slice was shown, because all slices require full FOV encoding. The minimal FOV for each rf offset frequency in table 3.1 was plotted in (e).

diminishing area of signal visibility. The rFOV 3D-PE-TSE data was acquired without (Figure 3.6c-d) and with CS acceleration (Figure 3.6e-f) to reduce the total scan time of 10 min 55 sec (Figure 3.6c-d) to 3.5 min (Figure 3.6e-f), respectively. No large differences were observed between the fully sampled (Figure 3.6c-d) and CS accelerated 3D-PE-TSE images in the high intensity regions (Figure 3.6e-f). In these experiments the rFOV factor was used to increase the resolution of the images with a factor four to obtain voxel sizes of 1.25x1.56x2 mm, which was four times higher than in the full FOV acquisitions.
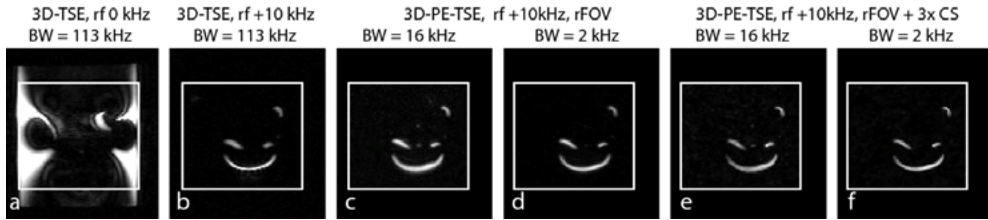

Figure 3.6: 3D-TSE acquisitions were performed with full FOV (a-b) for planning of the reduced FOV 3D-PE-TSE acquisitions (c-f) without (c-d) and with (e-f) CS acceleration. Different time points were included in the reconstructions to obtain a 16 kHz (c,e) and 2 kHz (d,f) BW. The acquisition times of 3D-PE-TSE were 10 min 55 sec (c-d) and 3 min 38 sec (e-f), respectively. All images were reconstructed with a 4 mm z partition thickness.

Table 3.1: FOV reduction for ms3D-PE-TSE

Excitation frequency (kHz)~	FOV with signal present (mm)#	rFOV (%)*	Time rFOV (min)*	Time rFOV + 3x CS/SENSE (min)*
-21.4	75 x 60 x24	5%	1.1	0.4
-18.4	76 x 64 x 35	8%	1.8	0.6
-15.3	78 x 65 x 38	9%	2.0	0.7
-12.2	82 x 68 x 54	14%	3.1	1.0
-9.2	86 x 75 x 56	17%	3.7	1.2
-6.1	96 x 88 x 58	23%	5.1	1.7
-3.1	128 x 128 x 67	52%	11.3	3.8
0	128 x 128 x 128	100%	21.7	7.2
+3.1	103 x 100 x 128	63%	13.7	4.6
+6.1	73 x 68 x 69	21%	4.5	1.5
+9.2	70 x 62 x 76	16%	3.4	1.1
+12.2	70 x 60 x 70	14%	3.0	1.0
+15.3	70 x 59 x 67	13%	2.8	0.9
+18.4	70 x 57 x 64	12%	2.7	0.9
+21.4	69 x 56 x 63	12%	2.5	0.8

~ The frequency offset as calculated from the Bloch simulations in Figure 3.2j was used for the calculations.
# Voxels were selected within 5.12 kHz around the excitation frequency (99% of the effective rf BW) based on the field distribution of a knee implant with dχ = 1300.
* FOV reduction percentages and calculated scan times are based on a 2 x 2 x 2 mm voxel size, a turbo factor of 10 per 100 ms, a 3D spherical shutter and a full FOV of 128x128x128 mm

3.3.5 TEMPORAL SIGNAL IN MS3D-PE-TSE

The ms3D-PE-TSE sequence was also used to reconstruct a series of sum-of-squares images, enabling analysis of the signal evolution in time. This property is unique to fully phase-encoded imaging and might potentially be used to detect metallic wear of the implant by measuring changes in T_2^*. The influence of metal induced field inhomogeneities on the spin-echo formation is demonstrated in Figure 3.7. The susceptibility induced field gradients in the direct vicinity of the knee implant caused signal dephasing leading to fast T_2^* decay, which was clearly observed in voxels close to the knee implant (Figure 3.7a-b). The net sum-of-squares magnitude signal decayed within ±0.4 ms on both sides of the center of the echo. The echo peak widened with increasing distance from the implant (Figure 3.7c). Peak broadening was most likely caused by reduced intra-voxel dephasing related to susceptibility induced gradients further away from the implant.
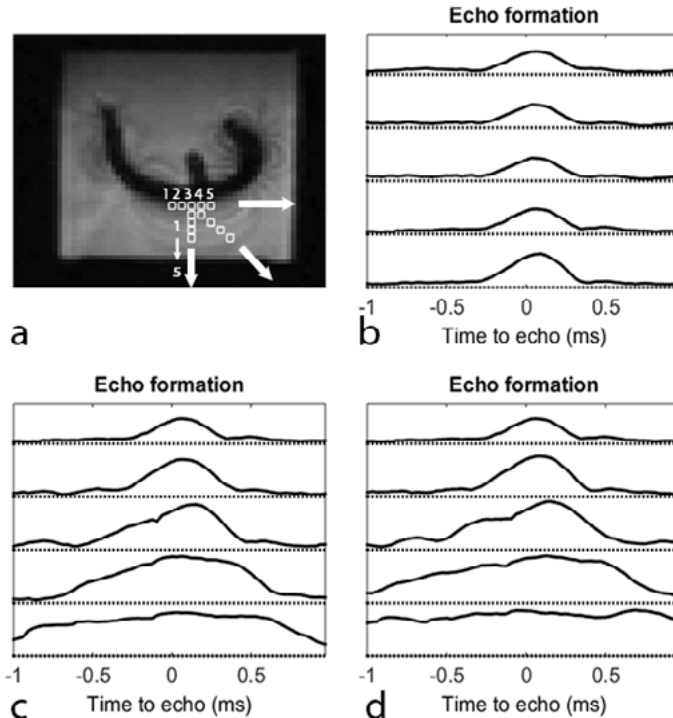

Figure 3.7: The ms3D-PE-TSE temporal signal curves of the voxels indicated in the image (a) are shown. The position from the implant was varied by selecting voxels with an equal distance (b), linearly (c) or diagonal (d) increasing distance. The temporal signal curves (labeled 1 to 5 in b-d) were stacked above each other for visualization purposes.

3.4 DISCUSSION

In this work, the artifact reduction performance, scan time limitations and temporal signal characterization of ms3D-PE-TSE for imaging near metal were assessed *in vitro*. Below we will elaborate on the potential applications and current scan time limitations of ms3D-PE-TSE.

3.4.1 IMAGE ARTIFACT REDUCTION

The ms3D-PE-TSE sequence prevented image artifacts related to extreme susceptibility gradients (12) across all frequency bins. The added value of phase-encoded imaging was most pronounced in the far off-resonance regions (>±10kHz), which are currently not acquired with frequency-encoded techniques, as these ranges are notoriously challenging (12). Imaging these far off-resonance regions may be particularly useful for detection of pseudo-tumors (23), bone marrow edema (24) or bone metastases (25) that can occur close to the implant. In suspicious cases, phase-encoded imaging might be used to complement existing multispectral frequency-encoded sequences to detect signal deviations in the vicinity of the implant or to act as a gold standard to exclude hyper-intensity artifacts.

In addition to possibilities for anatomical imaging, the geometrically advantageous properties of phase-encoded sequences (16) might be exploited for metal localization studies. The post-operative location of orthopedic implants can then be determined relative to either world coordinates or anatomical reference points, which can be useful to assess the accuracy of surgical procedures.

3.4.2 SCAN TIME LIMITATIONS

In this work the possibilities for rFOV imaging were calculated for the femoral part of a knee implant. The FOV reduction of the far off-resonant bins, where 3D-PE-TSE can be beneficial, was limited by the size of the implant. In our case, the required FOV around the femoral part the implant was approximately ~6x6x6 cm, which is comparable to the size of the femoral head of hip implants, or various orthopedic stainless steel screws. Therefore, similar scan time acceleration factors as mentioned in this work can be expected for these materials. To perform accurate and automated planning of rFOV ms3D-PE-TSE imaging on a clinical system, it will be also be useful to determine the frequency content using fast calibration scans (26).

Despite the high acceleration factors from turbo acceleration, k-space undersampling and rFOV imaging, there are still substantial scan time limitations to overcome for ms3D-PE-TSE. The main limitation to increase the frequency range in 3D-PE-TSE was the limited maximum B_1 that prevents large bandwidth refocusing pulses. Innovations that enable the acquisition of an increased frequency range hold potential to significantly decrease the acquisition time of multispectral phase-encoded acquisition schemes. Multiband excitation has been

suggested to obtain multiple 3D-PE-TSE frequency bins in a single acquisition (27). The combination of such pulses with rFOV imaging and k-space undersampling acceleration might enable full ms3D-PE-TSE acquisitions in acceptable scan times. Additionally, the characteristic spatial off-resonance distribution of the individual frequency bins might be used to accelerate multispectral imaging (28) in a similar manner as done with coil sensitivity profiles in parallel imaging.

In its current state, however, *in vivo* application of ms3D-PE-TSE is limited to imaging of the off-resonance regions where multiple off-resonance bins can be obtained within ~10 min. For the on-resonance bins that require a large FOV, it may be possible to reduce the FOV by exploiting off-resonance suppression techniques (29), which have been explored recently to perform fast 2D SEMAC acquisitions (30).

### 3.4.3 EXPLOITING THE TEMPORAL SIGNAL

The temporal signal of (ms)3D-PE-TSE is a unique property that can potentially be exploited to optimize the sensitivity, perform undistorted frequency offset mapping, detect intra-voxel gradients and perform T_2^* mapping. Accurate field mapping near the implant, may for example be useful in detecting paramagnetic particles from metal wear (31). Closer to the implant, however, the induced gradients over a voxel are stronger, thereby increasing the T_2^* decay. In our work the acquisition window close to the implant was limited to ~1 ms, thereby decreasing the detection sensitivity for small metallic particles close to the implant. In these cases it might be beneficial to increase the spatial resolution to mitigate fast signal decay due to intravoxel dephasing.

3.5 CONCLUSION

In this work we demonstrated the artifact reduction capabilities of ms3D-PE-TSE for regions where frequency-encoded sequences are fundamentally limited. The combination of recent scan time acceleration methods with rFOV phase-encoded imaging, enables MRI in the direct vicinity of metal implants.

APPENDIX

The sum-of-squares images in this work were reconstructed from 35 and 17 individual frequency bins for ms3D-TSE and ms3D-PE-TSE, respectively. All individual frequency bins are shown below for both methods.
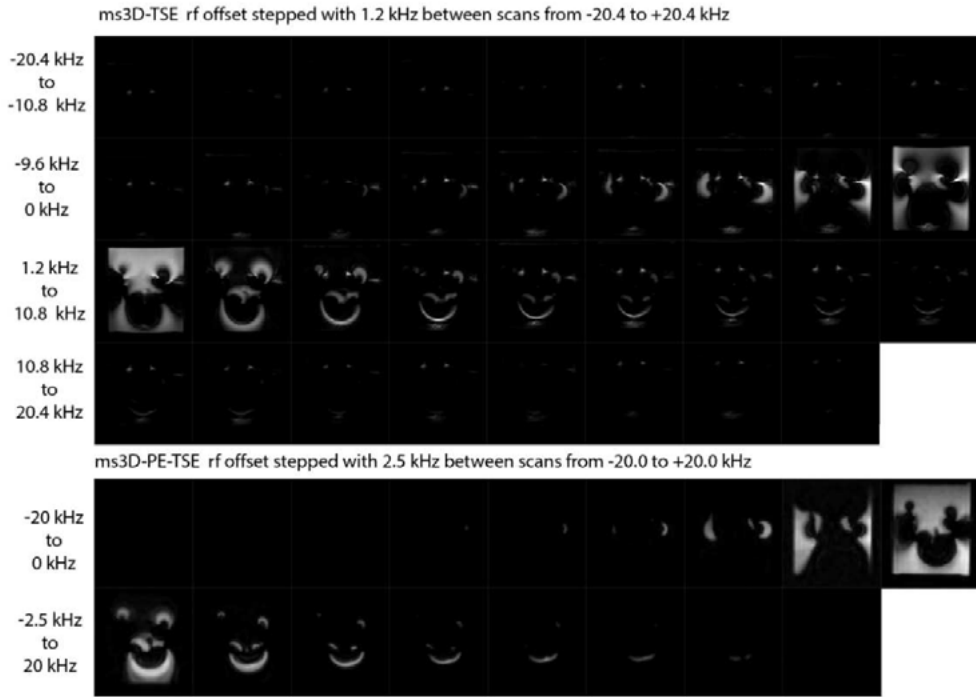
REFERENCES

1. Cram P, Lu X, Kates SL, Singh JA, Li Y, Wolf BR. Total Knee Arthroplasty Volume, Utilization, and Outcomes Among Medicare Beneficiaries, 1991-2010Knee Arthroplasty Volume, Use, and Outcomes. JAMA 2012;308(12):1227-1236.

2. Smith AJ, Dieppe P, Vernon K, Porter M, Blom AW. Failure rates of stemmed metal-on-metal hip replacements: analysis of data from the National Joint Registry of England and Wales. The Lancet 2012;379(9822):1199-1204.

3. Toms A, Smith-Bateman C, Malcolm P, Cahir J, Graves M. Optimization of metal artefact reduction (MAR) sequences for MRI of total hip prostheses. Clin Radiol 2010;65(6):447-452.

4. Cha JG, Jin W, Lee MH, Kim DH, Park JS, Shin WH, Yi BH. Reducing metallic artifacts in postoperative spinal imaging: usefulness of IDEAL contrast-enhanced T1-and T2-weighted MR imaging—phantom and clinical studies. Radiology 2011;259(3):885-893.

5. Koch KM, Lorbiecki JE, Hinks RS, King KF. A multispectral three-dimensional acquisition technique for imaging near metal implants. Magn Reson Med 2009;61(2):381-390.

6. Lu W, Pauly KB, Gold GE, Pauly JM, Hargreaves BA. SEMAC: slice encoding for metal artifact correction in MRI. Magn Reson Med 2009;62(1):66-76.

7. Seevinck PR, de Leeuw H, Bos C, Bakker CJ. Highly localized positive contrast of small paramagnetic objects using 3D center-out radial sampling with off-resonance reception. Magn Reson Med 2011;65(1):146-156.

8. Hayter CL, Koff MF, Potter HG. Magnetic resonance imaging of the postoperative hip. J Magn Reson Imaging 2012;35(5):1013-1025.

9. Harris WH. Osteolysis and particle disease in hip replacement: a review. Acta Orthop 1994;65(1):113-123.

10. Cahir J, Toms A, Marshall T, Wimhurst J, Nolan J. CT and MRI of hip arthroplasty. Clin Radiol 2007;62(12):1163-1171.

11. Koch K, Brau A, Chen W, Gold G, Hargreaves B, Koff M, McKinnon G, Potter H, King K. Imaging near metal with a MAVRIC-SEMAC hybrid. Magn Reson Med 2011;65(1):71-82.

12. Koch KM, King KF, Carl M, Hargreaves BA. Imaging near metal: the impact of extreme static local field gradients on frequency encoding processes. Magn Reson Med 2014;71(6):2024-2034.

13. Smith MR, Artz NS, Wiens C, Hernando D, Reeder SB. Characterizing the limits of MRI near metallic prostheses. Magn Reson Med 2015;74(6):1564-1573.

14. Artz NS, Hernando D, Taviani V, Samsonov A, Brittain JH, Reeder SB. Spectrally resolved fully phase-encoded three-dimensional fast spin-echo imaging. Magn Reson Med 2014;71(2):681-690.

15. van Gorp JS, Bakker CJ, Bouwman JG, Smink J, Zijlstra F, Seevinck PR. Geometrically undistorted MRI in the presence of field inhomogeneities using compressed sensing accelerated broadband 3D phase encoded turbo spin-echo imaging. Phys Med Biol 2014;60(2):615.

16. Bakker CJ, de Leeuw H, van de Maat GH, van Gorp JS, Bouwman JG, Seevinck PR. On the utility of spectroscopic imaging as a tool for generating geometrically accurate MR images and parameter maps in the presence of field inhomogeneities and chemical shift effects. Magn Reson Imaging 2013;31(1):86-95.

17. Carl M, Koch K, Du J. MR imaging near metal with undersampled 3D radial UTE-MAVRIC sequences. Magn Reson Med 2013;69(1):27-36.

18. Lustig M, Donoho D, Pauly JM. Sparse MRI: The application of compressed sensing for rapid MR imaging. Magn Reson Med 2007;58(6):1182-1195.

19. Bloch F. Nuclear induction. Physical review 1946;70(7-8):460.

20.   Salomir R, de Senneville BD, Moonen CT. A fast calculation method for magnetic field inhomogeneity due to an arbitrary distribution of bulk susceptibility. Concepts in Magnetic Resonance Part B: Magnetic Resonance Engineering 2003;19(1):26-34.

21.   Bouwman JG, Bakker CJ. Alias subtraction more efficient than conventional zero-padding in the Fourier-based calculation of the susceptibility induced perturbation of the magnetic field in MR. Magn Reson Med 2012;68(2):621-630.

22.   Koch K, Hargreaves B, Pauly KB, Chen W, Gold G, King K. Magnetic resonance imaging near metal implants. J Magn Reson Imaging 2010;32(4):773-787.

23.   Pandit H, Glyn-Jones S, McLardy-Smith P, Gundle R, Whitwell D, Gibbons C, Ostlere S, Athanasou N, Gill H, Murray D. Pseudotumours associated with metal-on-metal hip resurfacings. Journal of Bone & Joint Surgery, British Volume 2008;90(7):847-851.

24.   Chang EY, McAnally JL, Van Horne JR, Statum S, Wolfson T, Gamst A, Chung CB. Metal-on-metal total hip arthroplasty: do symptoms correlate with MR imaging findings? Radiology 2012;265(3):848-857.

25.   Santavirta S, Hoikka V, Eskola A, Konttinen YT, Paavilainen T, Tallroth K. Aggressive granulomatous lesions in cementless total hip arthroplasty. Journal of Bone & Joint Surgery, British Volume 1990;72(6):980-984.

26.   Koch KM. Metal implant-induced spectral range optimization using rapid 3D-MSI calibration scans. Proc 23th Annual Meeting ISMRM, Toronto 2015:2511.

27.   Artz NS, Wiens CN, Smith MR, Hernando D, Samsonov A, Reeder SB. In-Vivo Fully Phase-Encoded Magnetic Resonance Imaging in the presence of metal using multiband RF excitation. Proc 23th Annual Meeting ISMRM, Toronto 2015:3641.

28.   Smith MR, Artz NS, Koch KM, Samsonov A, Reeder SB. Accelerating sequences in the presence of metal by exploiting the spatial distribution of off-resonance. Magn Reson Med 2014;72(6):1658-1667.

29.   den Harder JC, van Yperen GH, Blume UA, Bos C. Off-resonance suppression for multispectral MR imaging near metallic implants. Magn Reson Med 2015;73(1):233-243.

30.   Valentina Taviani DL, Kevin M. Koch, Brian A. Hargreaves. Reduced FOV imaging near metal using 2D multispectral imaging and very selective outer volume suppression. Proc 23th Annual Meeting ISMRM, Toronto 2015:2505.

31.   Kevin M. Koch MFK, Parina Shah, Hollis G. Potter. A mechanism for quantifiable MRI-based detection of cobalt-chromium particulate deposits near total hip replacements. Proc 23th Annual Meeting ISMRM, Toronto 2015:0310.

SIGNAL CHARACTERIZATION

MULTIPLE SINGLE-POINT IMAGING (MSPI) AS A TOOL FOR CAPTURING AND CHARACTERIZING MR SIGNALS AND REPETITIVE SIGNAL DISTURBANCES WITH HIGH TEMPORAL RESOLUTION: THE MRI SCANNER AS A HIGH-SPEED CAMERA

ABSTRACT

In this paper we aim to lay down and demonstrate the use of multiple single-point imaging (mSPI) as a tool for capturing and characterizing steady-state MR signals and repetitive disturbances thereof with high temporal resolution.

To achieve this goal, various 2D mSPI sequences were derived from the nearest standard 3D imaging sequences by (i) replacing the excitation of a 3D slab by the excitation of a 2D slice orthogonal to the read axis, (ii) setting the readout gradient to zero, and (iii) leaving out the inverse Fourier transform in the read direction. The thus created mSPI sequences, albeit slow with regard to the spatial encoding part, were shown to result into a series of densely spaced 2D single-point images in the time domain enabling monitoring of the evolution of the magnetization with a high temporal resolution and without interference from any encoding gradients.

The high-speed capabilities of mSPI were demonstrated by capturing and characterizing the free induction decays and spin echoes of substances with long T_2s (>30ms) and long and short T_2^*s (4 - >30ms) and by monitoring the perturbation of the transverse magnetization by, respectively, a titanium cylinder – representing a static disturbance -, a pulsed magnetic field gradient – representing a stimulus inherent to a conventional MRI experiment –, and a pulsed electric current – representing an external stimulus.

The results of the study indicate the potential of mSPI for assessing the evolution of the magnetization and, when properly synchronized with the acquisition, repetitive disturbances thereof with a temporal resolution that is ultimately limited by the bandwidth of the receiver, but in practice governed by the SNR of the experiment and the magnitude of the disturbance. Potential applications of mSPI can be envisaged in research areas that are concerned with MR signal behavior, MR system performance and MR evaluation of magnetically evoked responses.

4.1 INTRODUCTION

Single-point imaging (SPI) is a scan technique in which only one point in k-space is acquired after each excitation. As each point is acquired at a fixed time after the excitation pulse, the effect from relaxation, chemical shifts, field inhomogeneities, diffusion, and other line-broadening mechanisms is constant, and the phase increment between successive encoding steps is entirely determined by the encoding gradients. As a consequence and in contrast to conventional imaging, the technique is immune to the blurring, distortion and shift artifacts normally invoked by field inhomogeneities, susceptibility deviations, and chemical shifts.

SPI was originally developed with solid-state (micro)imaging applications in mind (1). Solids are characterized by extremely broad lines and very short T_2 values and SPI was proposed for minimizing the effect of all line-broadening mechanisms while using modest gradient strengths. Up to the present day, SPI has retained the character of a laboratory technique and is typically only available on NMR spectrometers and not on clinical MRI systems. Applications are mostly encountered in solid-state physics, materials research, chemical engineering, food science, and related fields. In the realm of biomedicine, investigators have always been frightened by the lengthy examination times associated with purely phase-encoded techniques and applications of SPI have largely remained restricted to in vitro examinations of solid and quasi-solid tissues and specimens, including bone, teeth, cartilage, tendon, hair, and prosthetic materials (2-6).

Recently, initial experience with SPI in our group (7) made us aware of the fact that the usual restriction of SPI to solid tissues and short T_2 materials is unnecessary and counterproductive and that exactly the extension of SPI to the soft tissue regimen may open up new perspectives, both with regard to biomedical applications and acceleration of the technique. To appreciate this, it should be realized that the T_2 values of soft tissues are usually in the order of tens of milliseconds, at least two orders of magnitude longer than the sub-millisecond T_2 values of solid materials. These longer T_2s enable signal averaging and allow for the generation of spin echoes, as compared to the mere use of the initial amplitude of the FID in solid state imaging, and provide much flexibility in designing SPI sequences. In addition, and most interestingly within the framework of the present study, spatial encoding and data acquisition in SPI can be completely separated, and the relatively long T_2s create the possibility to acquire multiple single-point images (mSPI) with a very high temporal resolution. The mSPI sequence, albeit slow with regard to the spatial encoding part, thus offers the possibility to monitor the evolution of the (already spatially encoded) MR signals and repeatable disturbances thereof with a very high temporal resolution and without interference from any encoding gradients.

In the study reported here, we aim to demonstrate the high-speed (sub-millisecond) capabilities of multiple single-point imaging (mSPI) by some simple phantom experiments.

To achieve this goal, the required 2D mSPI sequences will be derived from the nearest standard 3D sequences by some easily implementable adjustments. This approach is attractive in that it provides direct access to the full imaging environment. The thus created mSPI sequences will be shown to result into a series of densely spaced single-point images in the time domain. The high-speed capabilities of mSPI will subsequently be demonstrated by examining the free induction decays and spin echoes of substances with long T_2s and long and short T_2^*s and by monitoring the perturbation of the transverse magnetization by, respectively, a titanium cylinder – representing a static disturbance -, a pulsed magnetic field gradient – representing a stimulus inherent to a conventional MRI experiment –, and a pulsed electric current – representing an external stimulus. The results will be shown to indicate the potential of mSPI for assessing the evolution of the magnetization and repetitive disturbances thereof with a temporal resolution that is ultimately limited by the bandwidth of the receiver, but in practice governed by the SNR of the experiment and the magnitude of the disturbance.

4.2 MATERIALS AND METHODS

4.2.1 SCAN TECHNIQUES

Imaging was done on a 1.5T clinical whole body system (Achieva, Philips Healthcare, The Netherlands) with standard imaging capabilities using an eight-element phased array head coil for signal reception. A sequence modification tool was made available by the manufacturer. All employed 2D mSPI sequences were created by applying the following modifications to the nearest standard 3D imaging sequences: i) selective excitation of a slab perpendicular to the second phase encoding direction (p_2 in Figure 4.1) was replaced by selective excitation of a slice (s in Figure 4.1) perpendicular to the read direction (r in Figure 4.1), ii) frequency encoding was disabled by setting the dephasing and rephasing lobe of the readout gradient to zero, and iii) the inverse FT along the read direction was removed from the 3D reconstruction. These modifications resulted into a set of equally spaced 2D single-point images in the time domain, describing the evolution of the magnetization during acquisition with a temporal resolution determined by the readout bandwidth: $\Delta t = 1/BW_{read}$. In Figure 4.1, the procedure is illustrated for the conversion of a conventional transversal 3D imaging sequence with readout along the vertical axis into a set of purely phase-encoded coronal 2D single-point images. Sagittal and transversal 2D mSPI data sets were derived from conventional 3D acquisitions in a similar way.

Experiments were done with single and multi-echo 2D mSPI sequences with a slice thickness between 5 and 10 mm. An external trigger pulse with a proper delay was fed to the cardiac triggering facility of the scanner when acquiring signals in the presence of a repetitive external disturbance. The employed 2D mSPI sequences were derived from the nearest 3D

spin-echo and 3D gradient echo-sequences which resulted into the following acquisition parameters for the 2D mSPI sequences:

SQ1: 2D mSPI-SE: TR/TE=240ms/25ms, flip angle=90°, FOV=64^2mm^2, scan matrix=64^2, BW$_{read}$=8000Hz, N_s=64, Δt=125μs, Tacq=N_s *Δt =8.0ms, scan duration=16.4min.

SQ2: 2D mSPI-GE: TR/TE=240ms/18ms, flip angle=30°, FOV=128^2mm^2, scan matrix=64^2, BW$_{read}$=2732Hz, N_s=64, Δt=366μs, Tacq=N_s *Δt =23.5ms, scan duration=16.4min.

SQ3: 2D mSPI-mGE: TR/TE=240ms/4x10ms, flip angle=30°, FOV=64^2mm^2, scan matrix=64^2, BW$_{read}$=13888Hz, N_s=64, Δt=72μs, Tacq=N_s *Δt =4.6ms, scan duration=16.4min.

The choice of a TR of 240 ms was dictated by the maximum cardiac trigger frequency of 250 beats per minute that is currently allowed on our system.
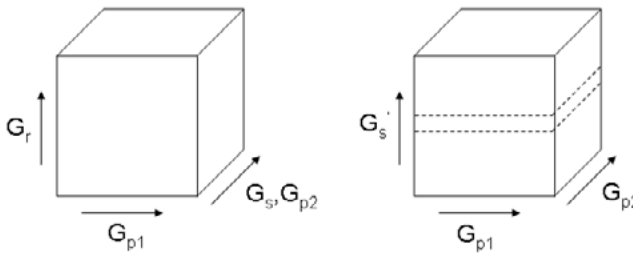

Figure 4.1: Steps involved in the conversion of a conventional transversal 3D acquisition (left) into a purely phase-encoded coronal 2D mSPI acquisition (right, dashed slice). In the latter, a series of N_s time-resolved single-point images is obtained by reconstructing a separate image for each point of the acquisition window. G_s, G_r, G_{p1} and G_{p2} refer to the selection gradient, the read gradient, and the first and second phase encoding gradients, respectively. Note the differences between the read and selection gradients in both cases.

4.2.2 PHANTOMS

To demonstrate the capabilities of the 2D mSPI sequences, we used a series of test tubes and some simple test objects. The test tubes contained a 2% agar gel with different concentrations of paramagnetic particles, i.c., 0, 1, 2, 3, and 4 mg holmium-loaded microspheres per cm^3. As described previously (8), such gels have a T_1 of about 1500 ms, a T_2 of about 33 ms, and a T_2^* varying between 33 ms and about 3 ms, depending on the concentration of the particles. The length of the tubes was 14 cm, the diameter 1.5 cm. The test objects consisted of various cylinders with doped water ($T_1 \approx T_2 \approx T_2^* \approx$ 250 ms). The first one was a coaxial cylinder with a height of 10 cm and a width of 5.7 cm and a 2.53 cm-diameter titanium rod as the inner cylinder. This arrangement was used to study MR signals in the presence of a static disturbance. The second cylinder had a height of 10 cm and a width of 5.0 cm and was used for monitoring the disturbance of the MR signal by a gradient

pulse – representing a stimulus inherent to MRI. A properly centered gradient pulse was obtained by exploiting the read gradient of the original 3D sequence for this purpose. Effectively, such a gradient acts as a projection dephaser across the slice (9). Successive mSPI images may thus be expected to exhibit an amount of dephasing that is proportional to the gradient strength and t'=t-TE. The third cylinder had a height and a diameter of 10 cm and was used for monitoring the repetitive disturbance of the MR signal by a pulsed electric current – representing a stimulus external to MRI. For this purpose, an isolated 0.4 mm-diameter copper wire was suspended horizontally in the fluid and perpendicular to B_0. The wire was connected to a current source providing a user-definable waveform and a trigger signal. The latter was used to properly synchronize the disturbance with the signal acquisition. Experiments were done with steady currents and block pulses and sinusoidal pulses with amplitudes up to 15 mA, frequencies up to 1000 Hz, and durations up to 50 ms. The delay between the trigger signal and the current pulse was 60 ms.

4.2.3 PROCESSING AND DISPLAY

Following on the mSPI acquisition, a complex image was reconstructed for each sample point t = TE+mΔt of the FID with $1 \leq m \leq N_s$ or each sample point of the spin echo with $-N_s/2 \leq m < N_s/2$, yielding a time resolved series of N_s complex images with temporal resolution $\Delta t = T_{acq}/N_s$. Complex images were converted to real, imaginary, magnitude, and phase maps for further analysis. To evaluate the effect of a disturbance on the MR signal, the signal in the presence of the disturbance was compared to the signal in the absence of the disturbance. For the case of a static field gradient and a pulsed gradient, the observed modulation of the complex signal was evaluated against the sinc-shaped modulation that is to be expected for a linear gradient across a voxel (10). For the case of a current pulse, Ampere's law was used to estimate the induced field disturbance ΔB_z. For a point in a plane perpendicular to an infinite wire along the x-axis this yields the following expression:

$$\Delta B_z(r, \theta, t) = \mu_0 \, I(t) \sin(\theta) \, /2\pi \qquad [4.1]$$

where I(t) represents the current along the x-axis, r the distance from the wire, and θ the angle with the z-axis. The theoretical value was compared to the observed field disturbance as calculated by taking the time derivative of the measured phase maps using $\gamma \Delta B = -\partial \phi / \partial t$.

4.3 RESULTS

In the first experiment, mSPI (SQ1) was used to produce time-resolved images of the evolution of the transversal magnetization in gels with a relatively long T_2 and a T_2^* inversely proportional to the concentration of holmium-loaded microspheres. Figure 4.2 shows the magnitude of the observed spin-echo signals for one of the pixels in the resultant series of SPI images for the blank sample and the sample with the shortest T_2^*. The large difference in the magnitude between both signals at the echo time TE is caused by irreversible signal dephasing due to diffusion in the holmium sample, as has been observed before (8). Figure 4.2 clearly demonstrates the capability of mSPI to monitor the signal decay induced by a paramagnetic agent with a temporal resolution that can only be achieved by interleaving many acquisitions in conventional imaging (8,11). The figure also demonstrates a shift between the time at which the echo maximum occurs and the nominal TE of 25 ms, a phenomenon that has been described before and is well understood (see, e.g., 12).
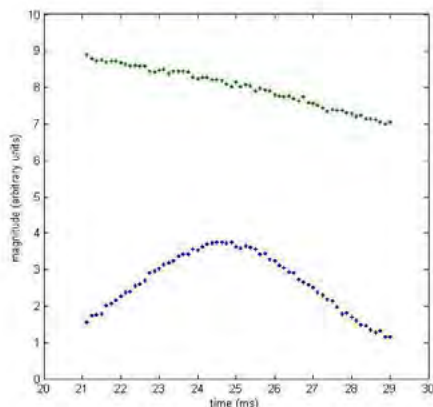

Figure 4.2: Spin-echo curves of, respectively, a blank gel with $T_2^* \approx T_2 \approx 33$ms (top) and a gel with 4 mg/ml holmium-loaded microspheres with $T_2^* \approx 3$ms (bottom). The signals were sampled at N_s=64 intervals of Δt=0.125ms, centered at TE=25ms. Note the absence of refocusing in the blank gel and the small leftward shift of the echo-peak with respect to TE in the holmium gel. The large difference in the magnitude between both signals at the echo time TE is caused by diffusion losses in the holmium sample.

In the second experiment, mSPI (SQ1) was used to closely examine the evolution of the magnetization in the presence of a static field disturbance, in this case induced by a titanium cylinder. Figure 4.3 shows the resultant phase map at t '= t-TE = 3 ms and the sinc-shaped evolution of the signal for a point near the cylinder. This signal behavior is typical for a linear gradient across a voxel and indicates the adequacy of this approximation for a small voxel at some distance from the perturber.
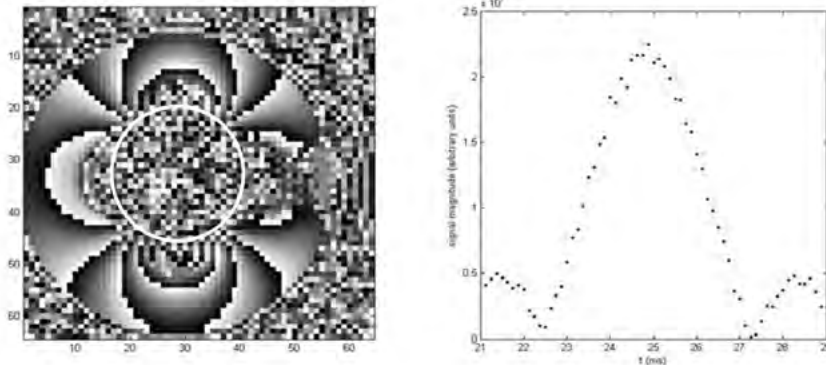
Figure 4.3: Left panel: coronal 2D mSPI phase map at t'=t-TE=3ms of a 5.7-cm diameter coaxial cylinder phantom with a 2.35-cm diameter titanium cylinder - indicated by the white circle - as the inner cylinder. Right panel: sinc-modulation of the spin-echo curve for a point in the annular region, in this case point (9,41). Signals were sampled at N_s=64 intervals of Δt=0.125ms, centered at TE=25ms.

In the third experiment, mSPI (SQ3) with echoes at 10, 20, 30, and 40ms was used to monitor the modulation of MR signals by a user-defined gradient pulse ('G_r' in Figure 4.4). This is an example of an MR intrinsic disturbance whereas gradients are normally applied for encoding purposes. In this case, the gradient operates as a projection dephaser across the slice. Figure 4.4 shows the sinc-shaped modulation of the magnitude of the signal that is known to be effectuated by such a projection dephaser (10). The strength of the gradient that can be deduced from the number of lobes in the observed pattern and the known slice thickness is 5.1 mT/m, which closely corresponds with the imposed gradient of 5.095 mT/m. Figure 4.4 further shows the evolution of the signal during the successive acquisition windows at 10, 20, 30 and 40ms for a voxel at the center and the edge of the slice, respectively. While nice sinc-profiles and exponential signal decays are observed at the center of the slice, profiles and decay curves at the edge appear to be severely distorted by field inhomogeneities.

In the fourth experiment, mSPI (SQ2) was used to monitor the modulation of MR signals by a user-defined electric current pulse synchronized with the acquisition. This is an example of an external disturbance. Figure 4.5 shows the modulation of the magnitude of the free induction decay by a synchronized current $I(t) = I_0\sin(2\pi ft)$ with f = 100 Hz and a span of 10 ms for a point near the current carrying wire. The figure further shows the differential responses of, respectively, the phase P of the signal and the logarithm of |S|. The latter provides an indication of the evolution of the phase spread across the voxel, the former of the average phase within the voxel. Evidently, mSPI will only be able to capture such disturbances if they are large enough with respect to the noise. This was readily verified by evaluating the disturbances at larger distances from the wire or by decreasing the current.
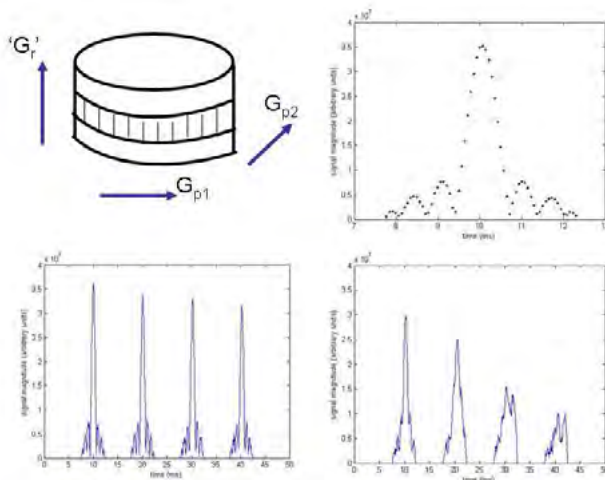
Figure 4.4: Schematic of the phantom and the setup (top left) that were used for monitoring the dephasing effect of a read gradient ('G_r') on the magnitude of the signal in a coronal 2D mSPI acquisition with multiple echoes. Sampling was done at 10, 20, 30, and 40ms with T_{acq}=4.6ms, N_s=64, and Δt=72μs. The top right panel shows the evolution of the signal during the acquisition window at 10ms for a voxel at the center of the slice. The bottom panels show the evolution of the signal during the acquisition windows at 10, 20, 30 and 40ms for a voxel at, respectively, the center (bottom left) and the edge (bottom right) of the slice. Note the sinc-profiles and exponential signal decay at the center of the slice and the inhomogeneity-degraded profiles and decay curve at the edge.
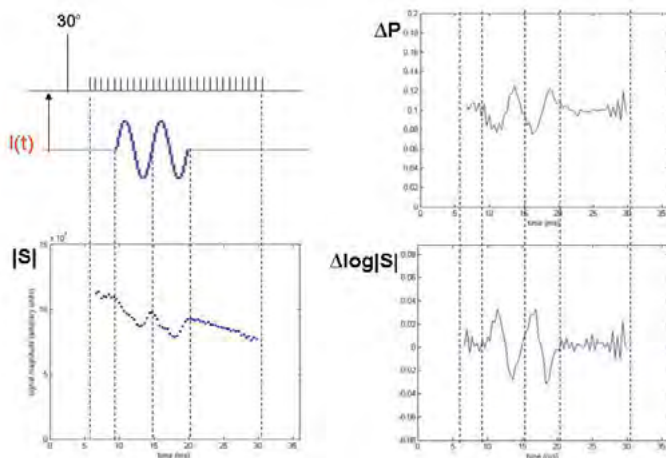
Figure 4.5: Schematic of the setup that was used for monitoring the modulation of the free induction decay by a synchronized current $I(t)=I_0\sin(2\pi ft)$ with f=100Hz and a span of 10ms for a point near the current carrying wire (top and bottom left). The signal was sampled at N_s=64 intervals of Δt=0.367ms, with T_{acq}=23.5ms centered at TE=18ms. The bottom left panel shows the response of the magnitude |S| of the signal. The top right and bottom right panels show the differential responses of, respectively, the phase P of the signal (top right) and the logarithm of |S| (bottom right). The latter provides an indication of the evolution of the phase spread across the voxel, the former of the average phase within the voxel.

Figure 4.6 finally shows that the observed current-induced phase changes are in good agreement with the values predicted by Ampere's law (Eq 4.1) using $\Delta\phi = -\gamma\Delta B_z t$. In this experiment, the phase change was induced by switching between a positive and a negative current of $I = 12.5$ mA along the x-axis.
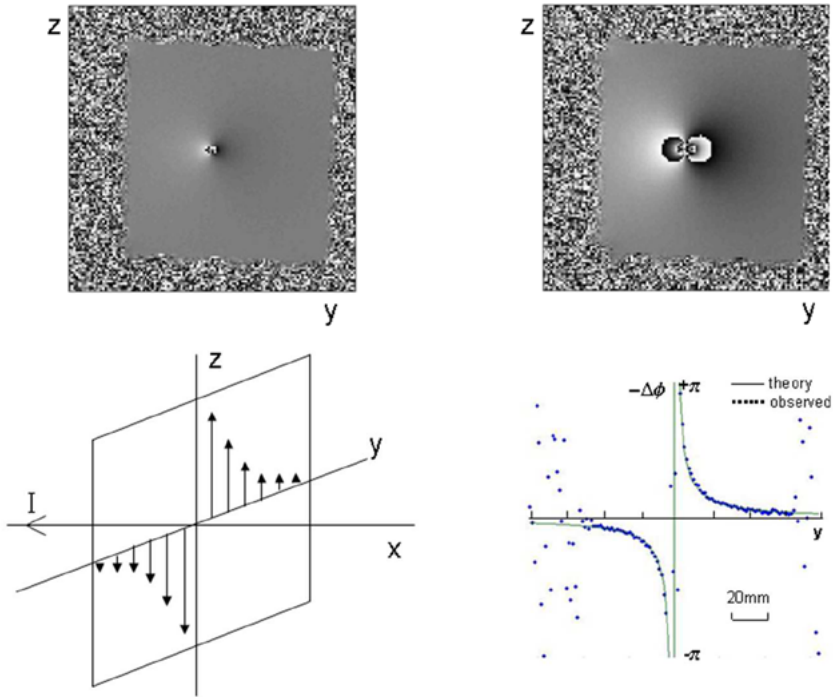
Figure 4.6: Sagittal maps of the phase difference induced by a positive and a negative current of I=12.5mA along the x-axis at t=6ms (top left) and at t=30ms (top right), respectively. The bottom left panel shows a schematic of the z-component of the B-field along the y-axis for a current along the x-axis. The bottom right panel shows a graph of the negative of the predicted and observed phase difference along the y-axis at t=6ms. Note the minus sign of $\Delta\phi$ and the occurrence of phase aliasing near the wire.

4.4 DISCUSSION

In this work, mSPI was proposed as a tool for monitoring the evolution of the transverse magnetization and repetitive disturbances thereof in substances with a relatively long T_2. Albeit a slow technique with regard to spatial encoding, mSPI was shown to provide a high temporal resolution and to behave like a high-speed camera when properly synchronized with the disturbance.

The use of mSPI for signal characterization and system monitoring purposes was made possible by migrating from the realm of solid materials to the realm of soft tissues. In the

former, T_2 values are typically in the microsecond range so that, in order to minimize signal loss, the initial amplitude of the FID has to be taken for the reconstruction of the – in this case – *single* single-point image (SPI). This is in contrast to the much longer T_2 values typically encountered in soft tissues, which permit reconstruction of *multiple* single-point images (mSPI), allow for signal averaging, enable acquisition of spin-echoes, and provide much more flexibility in designing mSPI sequences. The migration from solid to soft tissues thus makes life easier without introducing undesirable side effects.

The 2D mSPI sequences that were used in this study were created in the research mode of a standard MR scanner by some straightforward modifications of the nearest conventional 3D spin echo and gradient echo sequences. This approach provided immediate access to the full capabilities of the imaging environment. Besides, integration of mSPI into the imaging environment appeared to be much easier and far less restrictive – at least on our system and for the specific purpose of a high-speed camera - than incorporation of mSPI into the spectroscopy environment, despite evident similarities between mSPI and a spectroscopic imaging (SI) sequence. Here it should be emphasized that the intentions of mSPI and SI are very different, leading to differences both with respect to the acquisition part and the reconstruction and processing part. SI, on the one hand, is directed at low-concentration tissue metabolites like NAA, creatine and lactate. It usually features large voxels and a large number of signal averages to obtain sufficient SNR and a long acquisition window and a large number of samples to obtain sufficient spectral resolution. The long repetition time that is typically used in SI generally obviates the need of sophisticated spoiling and refocusing measures. mSPI, on the other hand, is directed at imaging of the bulk protons of water and fat and of disturbances of their signals with a high spatial and temporal resolution. The acquisition window, the voxel size, the number of signal averages, and the repetition time are, therefore, usually much smaller than in spectroscopic imaging. The much smaller repetition times make spoiling and refocusing in mSPI an important concern. This concern has usually been taken care of in the imaging environment. Finally, it should be appreciated that the spectral content of the recorded signal in mSPI is not only dependent on the excitation BW, but on the frequency content of the disturbance as well, as is easily learned from the experiments with internal and external stimuli.

One of the attractive features of mSPI as compared to conventional imaging techniques is the complete separation between the excitation-encoding part and the data acquisition part of the sequence. This separation implies that, once the signal has been encoded, there is freedom to interact with the MR signal during the acquisition window without affecting the spatial encoding. The time available for such interactions is limited by T_2 or T_2^* and will be dependent on the acquisition mode (FID, single echo, multi-echo, etc.). Another attractive aspect of mSPI is the extremely high temporal resolution that can be achieved, at least in principle. Theoretically the resolution is limited by the bandwidth of the receiver (3 MHz on our system), but in practice the limit will be determined by the SNR of the

experiment, the magnitude and character of the disturbance, and the employed averaging and filtering techniques.

With regard to potential applications of mSPI, the first area that comes to mind is related to our experiments with the holmium-loaded microspheres. It is the use of mSPI as a gold standard technique for the analysis and quantification of object-induced microscopic and macroscopic field inhomogeneities. Examples of this application would be the detailed characterization of the FIDs and spin-echo signals of tissues/ organs after the administration of paramagnetically labeled contrast agents, drugs, and other substances. As shown by the results for one of the holmium samples in Figure 4.2, mSPI is readily able to offer a temporal resolution that previously could only be attained by interleaving many shifted mGE sequences (8,11), and with all the additional benefits of SPI with regard to image quality. Such detailed signal curves could be helpful in analyzing and characterizing the diffusion regimes in which particle systems may reside, e.g., static dephasing or motional narrowing, and in evaluating theories that have been proposed to describe such systems (12,13 and references therein).

The second area of applications of mSPI that suggests itself is in the area of MRI performance testing and quality assurance. As illustrated by the experiment with the gradient pulse (Figure 4.3) and reported about in the literature (14), mSPI is an ideal tool for characterizing the response of MR signals to stimuli inherent to MRI, including RF pulses and gradient waveforms. mSPI can, for instance, be used to analyze the effects of eddy currents on gradient waveforms or to examine the influence of background gradients on the quality of spin-echoes and gradient echoes, which may be relevant to quantitative relaxation studies.

The third area of applications of mSPI that can be envisaged is suggested by our experiment with the pulsed electric current. It is the study of repetitive perturbations of MR signals by external stimuli. An example of such an application would be the characterization of the field disturbance invoked by transcranial magnetic stimulation (15). The ultimate challenge here would of course be to capture the very weak and short-lived field disturbances invoked by the TMS-induced neuronal currents (16).

With regard to the limitations of mSPI, lack of efficiency is the key issue. Since only one point in k-space is acquired after each excitation, as compared to, e.g., 256 points when a readout gradient is applied, mSPI tends to be about two orders of magnitude slower with respect to spatial encoding than the corresponding standard imaging sequence. To put this dramatic difference in proper perspective, however, it should be noted that the use of frequency encoding instead of phase encoding is never free of charge, but always involves compromises with respect to SNR and image quality. In addition, when multiple time points with small echo spacing are required these frequency encoded sequences need to be repeated a number of times with a slightly different TE, while mSPI yields this temporal information in a single acquisition, therefore becoming significantly more efficient than for

single time point experiments. A full discussion of the trade-offs that are involved is not a trivial exercise at all and lies outside the scope of this paper. In the present study, a 2D setup and small field-of-views and acquisition matrices were used to achieve adequate spatial resolution, while avoiding excessive scan times and still be able to demonstrate essential features. In future work we will try to push the limits by incorporating some of the acceleration tools that we already discussed and partly demonstrated in previous work (7,17,18), including multiple spin echo techniques, multipoint k-space mapping techniques, parallel imaging techniques, and sparse sampling techniques (19-21). Finally it should be realized that the slowness of mSPI and the necessity to synchronize the acquisition with a repetitive signal disturbance both emerge from the spatial encoding part of the technique. Real-time monitoring of single events and transient phenomena would, therefore, easily come into reach when the acquisition would be restricted to a single volume. Such a localized approach has in fact been demonstrated long ago for the detection of transient enhancement of transverse relaxation in the brain following bolus administration of contrast agents (22).

Reviewing our findings, we conclude that mSPI offers a powerful research tool for investigating MR signals and repetitive disturbances thereof with high temporal resolution, and that this research tool may evolve toward a more *practical* tool by fully exploiting current developments with regard to scan time reduction.

REFERENCES

1. Emid S, Creyghton JHN. High resolution NMR imaging in solids. Physica B 1985;128: 81-83.
2. Seo Y, Takamiya H, Ishikawa H, Nakashima T, Sharf Y, Navon G. NMR imaging of rigid biological tissues. In: Bluemich B, Bluemer P, Botto R (eds). Spatially resolved magnetic resonance. Proceedings of the 4th International Conference on Magnetic Resonance Microscopy and Macroscopy, Albuquerque, September 1997. Wiley-VCH, Weinheim, 1998;445-457.
3. Appel TR, Baumann MA. Solid-state nuclear magnetic resonance microscopy demonstrating human dental anatomy. Oral Surg Oral Med Oral Pathol Oral Radiol Endod 2002;94:256-261.
4. Ramos-Cabrer P, van Duynhoven JPM, van der Toorn A, Nicolay K. MRI of hip prostheses using single-point methods: in vitro studies towards the artifact-free imaging of individuals with metal implants. Magn Reson Imaging 2004;22:1097-1103.
5. Gruwel MLH, Latta P, Tanasiewicz M, Volotovskyy V, Sramek M, Tomanek B. MR imaging of teeth using a silent single point imaging technique. Appl Phys A 2007;88:763-767.
6. Mattle E, Weiger M, Schmidig D, Boesiger P, Fey M. MRI of human hair. MAGMA 2009;22:181-186.
7. Bakker CJG, De Leeuw H, Van de Maat GH, Van Gorp JS, Bouwman JG, Seevinck PR. On the utility of spectroscopic imaging for generating geometrically accurate MR images and parameter maps in the presence of field inhomogeneities and chemical shift effects. Magn Reson Imaging 2013;31:86-95.
8. Seevinck PR, Seppenwoolde JH, Zwanenburg JJ, Nijsen JF, Bakker CJ. FID sampling superior to spin-echo sampling for T2*-based quantification of holmium-loaded microspheres: Theory and experiment. Magn Reson Med 2008;60:1466-1476.
9. Bakker CJ, Seppenwoolde JH, Vincken KL. Dephased MRI. Magn Reson Med 2006;55:92-97.
10. Haacke EM, Brown RW, Thompson MR, Venkatesan R. Magnetic resonance imaging: Physical principles and sequence design. New York: Wiley, 1999.
11. Du J, Hamilton G, Takahashi A, Bydder M, Chung CB. Ultrashort echo time spectroscopic imaging (UTESI) of cortical bone. Magn Reson Med 2007;58:1001-1009.
12. Jensen JH, Chandra R. Strong field behavior of the NMR signal from magnetically heterogeneous tissues. Magn Reson Med 2000;43:226-236.
13. Sukstanskii AL, Yablonskiy DA. Gaussian approximation in the theory of MR signal formation in the presence of structure-specific magnetic field inhomogeneities. Effects of impermeable susceptibility inclusions. J Magn Reson 2004;167:56-67.
14. Latta P, Gruwel MLH, Volotovskyy V, Weber MH, Tomanek B. Simple phase method for measurement of magnetic field gradient waveforms. Magn Reson Imaging 2007;25:1272-1276.
15. Hernandez-Garcia L, Lee S, Grissom W. An approach to MRI-based dosimetry for transcranial magnetic stimulation. Neuroimage 2007;36:1171-1178.
16. Petridou N, Plenz D, Silva AC, Loew M, Bodurka J, Bandettini PA. Direct magnetic resonance detection of neuronal electrical activity. Proc Nat Acad Sci 2006;103:16015-16020.
17. Crijns SPM, Bakker CJG, Seevinck PR, De Leeuw H, Lagendijk JJW, Raaymakers BW. Towards inherently distortion-free MR images for image-guided radiotherapy on an MRI accelerator. Phys Med Biol 2012;57:1349-1358.
18. Van Gorp JS, JG Bouwman, CJG Bakker, PR Seevinck. Towards compressed sensing accelerated geometrically undistorted Single Point Images under 10 seconds. Proc Intl Soc Magn Reson Med 2012;20:1599.
19. Beya SD, Balcom BJ, Mastikhin IV, Bremner TW, Armstrong RL, Grattan-Bellew PE. Imaging of heterogeneous materials with a turbo spin echo single-point imaging technique. J Magn Reson 2000;144:255-265.

20.   Fernandez-Seara MA, Wehrli SL, Wehrli FW. Multipoint mapping for imaging of semi-solid materials. J Magn Reson 2003;160:144-150.
21.   Parasoglou P, Malioutov D, Sederman AJ, Rasburn J, Powell H, Gladden LF, Blake A, Johns ML. Quantitative single point imaging with compressed sensing. J Magn Reson 2009;201:72-80.
22.   Zhong J, Kennan R, Schaub M, Gore JC. Measurement of transient contrast enhancement by localized water NMR spectroscopy. J Magn Reson B 1994;104:111-118.

BI-EXPONENTIAL TRANSVERSE RELAXATION MAPPING OF SODIUM WITH HIGH TEMPORAL RESOLUTION USING 3D ULTRASHORT TE SPECTROSCOPIC IMAGING AT 7T

ABSTRACT

In this work a time-efficient strategy for quantitative characterization of bi-exponential sodium (^{23}Na) signal decay, total sodium concentration (TSC) mapping and ^{23}Na imaging was presented.

To achieve this goal, a 3D ultrashort TE spectroscopic imaging (UTE-SI) sequence was implemented on a 7T scanner to characterize single quantum (SQ) ^{23}Na signal behavior. Simulations were performed to evaluate the influence of T_2^* decay on image blurring for various k-space trajectories and to assess the accuracy of bi-exponential fitting models. The feasibility of 3D-UTE-SI for $T_2^*{}_{short}$, $T_2^*{}_{long}$ and TSC mapping as well as for ^{23}Na imaging was assessed *in vitro* and *in vivo* in the knees of two healthy volunteers. Additionally, compressed sensing (CS) acceleration was explored for scan time reduction. The ^{23}Na decay curves were sampled with 32 kHz bandwidth and 0.3 ms TE with 3D-UTE-SI, enabling reconstruction of ^{23}Na images with minimal blurring and accurate characterization of bi-exponential T_2^* decay. Quantitative $T_2^*{}_{short}$, $T_2^*{}_{long}$ and TSC maps were in accordance with literature values. 3D-UTE-SI data in the knee were acquired in 24 min (full) and 12 min (2x CS) with 3x3x5 mm voxels.

The results of this study demonstrated that simultaneous characterization of bi-exponential ^{23}Na decay, mapping of TSC and high SNR ^{23}Na imaging was feasible in acceptable scan times using 3D-UTE-SI.

5.1 INTRODUCTION

Sodium (^{23}Na) plays an important function in physiological processes such as maintaining homeostasis through osmotic and pH regulation and propagation of nerve and muscle impulses (1). In many diseases (e.g. tumors, stroke, multiple sclerosis) the ^{23}Na concentration levels change, owing to altered cellular integrity in organs such as the brain and heart (1-3) or structural changes in tissues such as cartilage (4,5). From an MR point-of-view the low *in vivo* ^{23}Na concentrations (10-300 mM) and MR sensitivity ($\gamma_{23Na}/\gamma_{1H}{\sim}0.26$) means that much longer scan times are required for high SNR ^{23}Na imaging compared to ^{1}H imaging.

In recent years, the signal-to-noise ratio (SNR) of ^{23}Na MR detection has increased due to the availability of high field human MRI scanners, which has stimulated the development of novel acquisition strategies for quantitative single quantum (SQ) ^{23}Na imaging (6-9). In previous work, it has been shown that determination of ^{23}Na fractions with free and restricted mobility may be useful in identifying ^{23}Na changes related to disease (4,10,11). In SQ ^{23}Na imaging the ^{23}Na fraction with restricted mobility can be characterized by its bi-exponential relaxation behavior with short (0.5 - 3.0 ms) and long T_2^* components (10 - 65 ms). Detection of short T_2^* components requires sequences with very short echo-times, such as (ultra)short TE radial (6,7) and spiral imaging techniques (9,12). These sequences apply relatively long frequency encoding gradients (up to 30 ms) to increase the SNR efficiency at the cost of increased image blurring for short T_2^* components and sensitivity to off-resonance effects.

To be able to quantify both T_2^* components in a relaxometry study it is necessary to acquire images at multiple echo times. This requires either a decrease of the readout gradient duration in combination with multi-echo acquisition strategies, which lowers the sensitivity, or additional acquisitions with different TEs, which further increases the acquisition time. In earlier work (12), a radial sequence with 0.15 ms TE was repeated with interleaved echo times to obtain nine images with increasing echo times to detect bi-exponential decay in cartilage. This resulted in scan times up to 40 minutes with an acquired resolution of 5.9x5.9x5.9 mm. In another recent study, a dual-TE imaging method was proposed (10) to detect the ^{23}Na fractions with free and restricted mobility in a significantly reduced scan time by subtraction of long and short TE images. However, to accurately quantify the bi-exponential T_2^* decay *in vivo*, more than two time points on the decay curve are required. A more flexible approach for transverse relaxation mapping is to use a fully phase-encoded spectroscopic imaging (3D-SI) sequence. Since no readout gradient is used, a series of data points with varying TEs can be acquired in a single acquisition with a high sampling bandwidth (BW), eliminating the need for multiple repetitions with different TE values. As such, this technique has also been dubbed the high-speed camera, enabling the detection of high frequency signal changes in the temporal signal domain (13). The high BW sampling

of the decay curve provides a tool for investigation of the assumptions implied in bi-exponential signal decay models (i.e. perfect bi-exponential decay, free or fixed amplitudes in the fitting model, inclusion of background noise). Additionally, the BW can be adjusted retrospectively by complex averaging of multiple data points to optimize the sensitivity of the analysis method based on the data (optimal sensitivity for $T_{acq} \sim T_2^*$ with total sampling time/total acquisition time ~0.8 - 0.95) (14).

In regular 3D-SI the phase encoding is applied in incremental strengths, while the phase encoding time is kept constant. It is also possible to keep the amplitude constant and to increment the time, allowing a much shorter echo time to be achieved for data acquired at the center of k-space, at the cost of some broadening of the point spread function (15,16). A hybrid approach was used in this work: by combining 3D-SI with variable TE sampling (17), a 3D-UTE-SI sequence with sub-ms TE is obtained, facilitating the detection of bi-exponential [23]Na decay and mapping of total sodium concentration (TSC). To investigate the performance of 3D-(UTE-)SI, simulations were performed to isolate the image blurring effect of T_2^* decay during k-space sampling and investigate the accuracy of bi-exponential T_2^* fitting models. Subsequently, phantom studies were performed for experimental validation of $T_{2,short}^*$, $T_{2,long}^*$ and M_0 mapping in freely moving [23]Na (H_2O) and [23]Na with restricted mobility (agarose) as well as high resolution [23]Na imaging with short TR. Finally, 3D-UTE-SI scans were acquired of the knees of two healthy volunteers to validate the method *in vivo* and to perform TSC mapping (18). Additionally, compressed sensing (CS) acceleration was explored to reduce the scan time.

5.2 THEORY

5.2.1 SAMPLING OF THE DECAY CURVE WITH SPECTROSCOPIC IMAGING

In 3D-SI the absence of a readout gradient results in the acquisition of a series of n_t temporally resolved images in a single repetition. The TE of each image is given by:

$$TE(n) = TE_0 + n * \frac{1}{BW} \qquad [5.1]$$

with TE_0 the starting time of the acquisition window. The time series of images enables the calculation of bi-exponential T_2^* decay, which can be described by:

$$s(t) = A_1 \exp\left(-\frac{t}{T_{2,short}^*}\right) + A_2 \exp\left(-\frac{t}{T_{2,long}^*}\right) \qquad [5.2]$$

with A_1 the amplitude of the short T_2^* component of [23]Na with restricted mobility, A_2 the combined amplitudes of the long T_2^* fraction of restricted and freely moving [23]Na. Without the presence of free [23]Na, the amplitude ratio can be approximated by $A_1/A_2 \sim 0.6/0.4$ (19-21). If partial volume effects are present, resulting in a contribution of free [23]Na, the fitted amplitudes may deviate from theoretically expected values (12).

5.2.2 SENSITIVITY OF SPECTROSCOPIC IMAGING

The sensitivity (ψ) of 3D-SI images reconstructed from the sampled time domain signal can be described by (14):

$$\psi = \frac{A(TR, \alpha) \; e^{-TE/T_2^*}}{a \; \sqrt{N_x N_y N_z \, BW \, T_{tot}}}$$ [5.3]

with A(TR,α) the amplitude of the FID as a function of the repetition time (TR) and flip angle (α), a a proportionality constant depending on the sample and hardware, $N_{x,y,z}$ the number of phase encoding steps in each spatial dimension, and T_{tot} the total acquisition time. Retrospective adaptation of the BW by complex averaging of time points can be used to optimize ψ for a specific T_2^* value, which is a unique property of 3D-(UTE-)SI.

5.3 METHODS

5.3.1 SIMULATIONS

2D-SI measurements of a spherical object (radius 32 mm) were simulated using the JEMRIS (22) package to obtain 3D datasets with one temporal and two spatial dimensions. The effect of T_2^* decay on image blurring during k-space traversal was investigated for SI, UTE-SI, Cartesian, 4 shot spiral and single shot spiral k-space trajectories. Here we followed a two-step approach. First, the exact time point of each k-coordinate was logged. Second, the corresponding data point from the simulated 3D dataset was assigned to each k-space coordinate. The BW (16 kHz) for each trajectory was equal. Potential reconstruction differences caused by gridding steps were eliminated by this approach.

In a second set of simulations, the accuracy of a non-linear regression fitting model (Eq 5.2) was investigated. Different amplitude setting were assessed, reflecting various models applied in the literature (9,12,23): 1) fixed amplitudes (A1/A2 = 0.6/0.4, data not shown), 2) free amplitudes and 3) amplitudes restricted to a ratio of M0 (A1=a_{short} and A2=1- a_{short}). The fitting performance was evaluated for SNR ranging between 3-100 and BWs of 8, 4, 2, 1 and 0.5 kHz (Figure 5.3, selected data shown). The different BWs were used to manipulate the relative contributions of the $T_2^*_{,short}$ and $T_2^*_{,long}$ components at each time point and investigate their influence on the fitting accuracy. Fitting statistics were obtained by regarding all voxels within the 2D object as separate measurements (196 voxels were included).

Simulation parameters: The simulated 2D object was assigned the relaxation properties of patellar cartilage ($T_2^*_{,short}$ = 0.5 ms, $T_2^*_{,long}$ = 11.4 ms, T_1 = 20 ms), to mimic a particularly challenging anatomy in terms of the very short T_2^* component (12). Both T_2^* components were simulated separately to investigate their individual effects on image quality prior to combining both components in a 0.6/0.4 ratio for evaluation of bi-exponential fitting.

Simulation parameters included 16 kHz BW, number of time domain points (n_t) = 1024, spatial resolution 1x1 mm, TR = 100 ms, TE = 0.6 ms, a 0.01 ms duration 90^0 block pulse and 2 dummy scans. Different levels of white Gaussian noise were added to the real and imaginary 2D-SI signal to obtain magnitude images with varying SNR values. To investigate the effect of BW, values were adjusted retrospectively by complex averaging of multiple time points.

5.3.2 MR EXPERIMENTS: PULSE SEQUENCE AND HARDWARE

All experiments were performed on a whole body 7T scanner (Philips, Best) using a custom-house built quadrature ^{23}Na birdcage coil combined with four ^{1}H-strip lines (24). A 3D-SI sequence (Figure 5.1a,c) was implemented with full control over the 3D k-space sampling pattern. The freedom to choose the sampling pattern was exploited for variable TE sampling by filling k-space in multiple shells to obtain ultrashort TEs (Figure 5.1b,d). Sampling patterns were designed to accommodate a 3D spherical shutter and variable density sampling for CS acceleration.
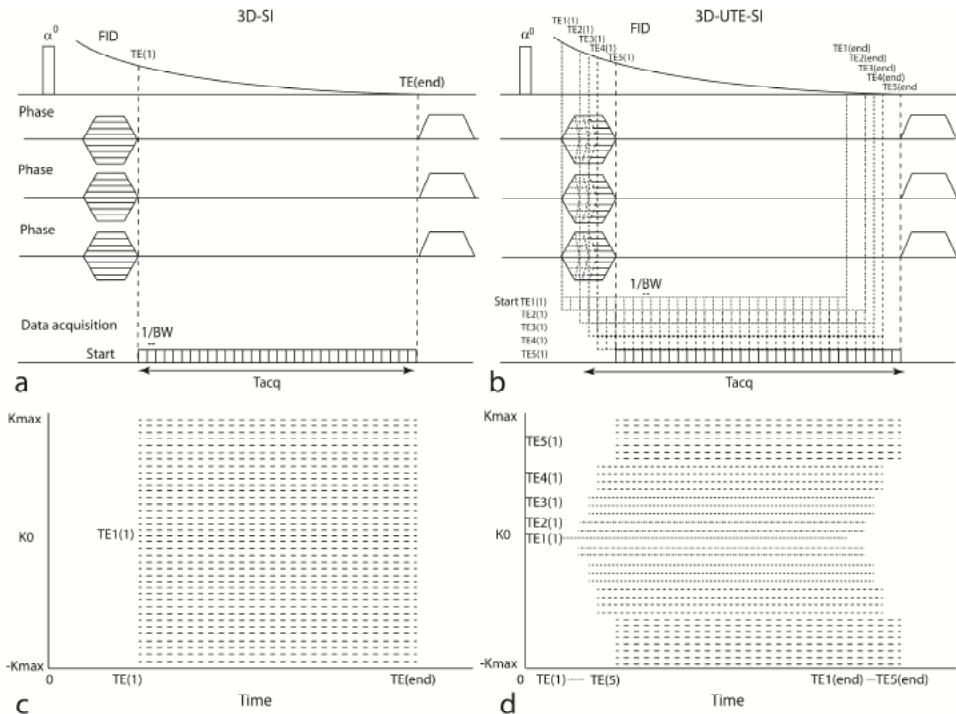

Figure 5.1: 3D-SI (a) and 3D-UTE-SI (b) sequences used for ^{23}Na imaging with high sampling of the decay curve at 7T. The minimum TE as a function of in one dimension of k-space is shown for both sequences (c-d).

5.3.3 EXPERIMENTAL SETUP

Phantom experiments: Two cylindrical phantoms (radius 50 mm, length = 50 mm) were constructed. Phantom A consisted of a large outer cylinder containing 2% agarose gel (no ^{23}Na), and within it six smaller tubes filled with the same gel and NaCl concentrations of 30, 40, 50, 70, 175 and 250 mM (Figure 5.4). ^{23}Na images were obtained with a conventional 3D gradient echo (3D-GRE, number of signal averages (NSA) 16) and a 3D-SI sequence (NSA 1) in 5 min 49 s per scan to compare the sensitivity of a frequency- and phase-encoded sequence with similar acquisition settings (see imaging parameters section).

Phantom B consisted of an outer cylinder of 4% agarose gel with 25mM NaCl, and within it two series of five tubes with 4% agarose and 50, 100, 150, 200 and 250 mM NaCl and 1 tube with 100 mM NaCl in H_2O (Figure 5.5a). As an external reference for *in vivo* quantification two sets of three tubes were used containing 75, 150 and 300 mM NaCl dissolved in H_2O and 2% agarose, respectively. The T_1 values of Phantom B and the 2% reference tubes were measured with a stack-of-spirals inversion recovery experiment for TSC relaxation corrections and Ernst angle calculations ($\alpha_{ernst} = \arccos(e^{-TR/T1})$). The T_1 map (Figure 5.5b) was reconstructed from multiple inversion times using a non-linear regression model with $S = A(1 - 2e^{-Tinv/T1} + e^{-TR/T1})$ as the input function (25).

To demonstrate the potential of 3D-SI data for bi-exponential signal characterization first a relatively long TR of 133 ms was used to acquire a high number of temporal data points ($n_t = 4096$, BW = 32 kHz). In a second experiment, high resolution 3D-SI and 3D-UTE-SI data (2x2x4 mm) were acquired to investigate the influence of variable TE sampling on the image amplitude and the degree of spatial blurring. The large number of repetitions (N_xxN_yxN_z) in 3D-(UTE-)SI prohibits imaging with a lower spatial resolution without decreasing the TR. To acquire a 2x2x4 mm resolution within a reasonable time frame (<30 min), a TR of 22 ms was used. Excitation was performed using the Ernst angle to obtain the optimal sensitivity at the specified TR (14). Note that the decreased TR also introduced T_1 saturation, due to incomplete T_1 relaxation between repetitions.

In vivo experiments: The knees of healthy two volunteers were scanned. The study was in accordance with the local IRB guidelines. First, a healthy 29-year old female was scanned in two separate sessions to acquire 3D-UTE-SI and stack-of-spirals ^{23}Na data with 3x3x5 mm resolution and 22 ms TR. The six reference tubes were positioned around the knee for TSC mapping purposes. Additionally, 3D-UTE-SI data were acquired with a factor 2 CS acceleration to reduce the acquisition time from 24 to 12 min. Second, a healthy 35-year old male was scanned with a 2x CS accelerated 3D-SI sequence in ~21 min with an increased TR of 40 ms to reduce T_1 saturation that may improve assessment of $T_2^*_{,long}$ values.

Imaging parameters: All 3D-(UTE-)SI data were acquired with BW = 32 kHz, NSA=1 and a 3D spherical shutter. Each scan session included the following preparation steps: localized second order B_0 shimming, ^{23}Na resonant frequency determination and pulse calibration.

Phantom A:
1) ^{1}H 3D-GRE, TR/TE = 22/2.79 ms, voxel size = 3x3x4 mm, FOV = 192x192x128 mm, flip angle (FA) = 70^0, readout bandwidth (BW_{read}) = 19 kHz, total acquisition time (T_{tot}) = 43 s
2) ^{23}Na 3D-GRE, TR/TE = 22/2.79 ms, voxel size = 4x4x4 mm, FOV = 128x128x128 mm, BW_{read} = 9.4 kHz, FA = 70^0, NSA=16, T_{tot}=5 min 49 s
3) ^{23}Na 3D–SI, TR/TE = 22/1.25 ms, voxel size = 4x4x4 mm, FOV = 128x128x128 mm, n_t = 512, FA = 70^0, T_{tot}= 5min 49s

Phantom B:
1) ^{23}Na stack-of-spirals inversion recovery, 6x6x8 mm voxels, TR/TE = 100/0.97 ms, inversion times (TI) 15:5:55 ms, readout duration 9 ms, 3 min per TI, T_{tot} = 27 min
2) ^{23}Na 3D-SI, TR/TE = 133/1.25 ms, voxel size = 4x4x4 mm, FOV = 128x128x128 mm, FA = 90^0, nt = 4096, T_{tot} = 36 min
3) ^{23}Na 3D-SI, TR/TE = 22/1.98 ms, voxel size = 2x2x4 mm, FOV = 128x128x128 mm, FA = 57^0, n_t = 512, T_{tot} = 24 min
4) ^{23}Na 3D-UTE-SI, TR/TE = 22/0.29 ms, voxel size = 2x2x4 mm, FOV = 128x128x128 mm, FA=57^0, n_t= 512, T_{tot} = 24 min
Scan 4 was acquired in 6 separate k-space shells (Figure 5.1b,d) with the following matrix sizes and TEs: k_0 with TE = 0.29 ms; 8x8x8 data matrix, TE = 0.56 ms; 16x16x16 data matrix, TE = 0.75 ms; 32x32x32 data matrix TE = 1.15 ms; and 64x64x32 data matrix with TE = 1.98 ms. Receiver gain settings were kept constant between acquisitions.

Volunteer 1 (2 sessions):
1) ^{1}H multi-slice GRE, TR/TE = 300/3.8 ms, voxel size = 0.5x0.5x3 mm, FOV = 192x192x160 mm, BW_{read} = 49 kHz, FA=40^0, T_{tot} = 5min 48s
2) ^{23}Na 3D-stack-of-spirals, TR/TE = 22/1 ms, readout duration 9 ms, BW_{read} = 30 kHz, 3x3x5 mm voxels, FOV = 192x192x160 mm, FA = 70^0, NSA=30, T_{tot} = 5min 28s
3) ^{23}Na 3D-UTE-SI, TR/TE = 22/0.29 ms, voxel size = 3x3x5 mm, FOV = 192x192x160 mm, FA = 70^0, n_t=1024, T_{tot} = 24 min
4) ^{23}Na 3D-UTE-SI, repeat scan 3 with 2x CS acceleration, T_{tot} = 12 min

Volunteer 2:
1) ^{23}Na 3D-SI, TR/TE = 40/1.5 ms, voxel size = 3x3x5 mm, FOV = 192x192x160 mm, FA = 65^0, nt = 1024, 2x CS, T_{tot} = 20min 48 s

5.3.4 Bi-exponential T_2^* mapping procedure

To obtain T_2^*,short, T_2^*,long and M_0 maps the magnitude signal was fitted with a constrained least squares fitting model in Matlab (R2014b, MA, USA) with Eq 5.2 as the input function. The amplitudes of T_2^*,short and T_2^*,long, A_1 and A_2 respectively, were fitted as a fraction of M_0 (defined as A_1=A_{short} and A_2=1-A_{short}). The fitting parameters were constrained with both T_2^* components ranging between 3-50 ms in phantoms and 0.1-30 ms *in vivo*. A_{short} and A_{long} were constrained to 0.5-0.7 and 0.3-0.5, respectively. Additional steps of the fitting procedure included:

1. Resampling to the desired BW by complex averaging of multiple time points
2. Normalization of the magnitude signal between 0 and 1 before fitting
3. Noise value determination by dividing the mean in the background by 1.253 (26)
4. A minimal SNR>10 to perform fitting
5. Truncation of the data to include only signal with SNR>3 to minimize the influence of Rician noise in the magnitude signal (23)
6. If (T_2^*,long - T_2^*,short) < 4 ms the signal was assumed to be mono-exponential and set to zero.
7. T_2^* maps were reconstructed after summation of three encodings in the slice direction.
8. A spatial Gaussian filter was used before fitting the *in vivo* data.

5.3.5 TSC mapping procedure

To relate the amplitudes of the *in vivo* ^{23}Na images to absolute concentrations it is necessary to construct a calibration curve from an external reference with a known concentration (18). In our work, three 2% agarose tubes containing 75, 150 and 300 mM NaCl were used for this purpose. An initial calibration curve was determined from the average amplitudes over five slices in these tubes in the *in vivo* images. However, these amplitudes were weighted according to their relaxation properties because a short TR and a non-zero TE were used. Therefore, the amplitudes of the calibration curve were corrected for T_1 and T_2^* effects using the spoiled steady state ^{23}Na signal model (18,25) according to:

$$M_0 = \frac{M_{x,y}(\theta, TE)(1 - e^{-TR/T_1}\cos(\theta))}{\sin(\theta)\,(1 - e^{-TR/T_1})e^{-TE/T_2^*}} \qquad [5.4]$$

with $M_{x,y}(\theta, TE)$ the measured ^{23}Na signal intensity at a given TE and flip angle. The transverse T_2^* relaxation was corrected with a single correction factor that was determined from the mean T_2^*,short and T_2^*,long relaxivity ($1/T_2^*$) values. The T_1 value of the reference tubes was determined from the measured T_1 map. After relaxation correction the calculated M_0 values of the 2% reference tubes were plotted as a function of concentration to obtain the final calibration curve.

Next, the *in vivo* [23]Na amplitudes were corrected for relaxation effects in a similar fashion using the literature T_1 value of cartilage at 7T (T_1 = 20 ms)(12) and the measured mean relaxivity in the cartilage regions. The relaxation corrected *in vivo* [23]Na amplitudes were fitted to the calibration curve to calculate the sodium concentration in each voxel, thereby obtaining TSC maps (Figure 5.8i). Note that the presented TSC maps are strictly only applicable to the cartilage regions since the T_1 and T_2^* correction factors may be different for other tissues. TSC maps were calculated using *in vivo* images with a 1 kHz BW.

5.3.6 DATA PROCESSING

The raw 4D k-space data were resampled to the desired BW by complex averaging of the desired number of time points for each k-space coordinate. A Tukey filter with a width of 0.4 was used in each k-space dimension to reduce ringing, while minimally affecting the T_2^* decay values (27). After k-space filtering a Fourier transformation was applied in each k-space dimension to obtain temporally resolved images. The variable TE acquisitions were scaled based on the value of k_0 that was acquired separately for all shells. The individual k-space shells were zero-filled to the same matrix size before summation.

5.3.7 CS RECONSTRUCTION

A non-linear conjugate gradient solver (28) was used to minimize $\lambda_w||\psi_w m||_1 + \lambda_{TV}TV(m)$ using a 3D wavelet (Daubechies 6) L_1 norm regularization and a 3D total variation norm regularization (λ_{TV}) to reconstruct 3D-SI data with three undersampled dimensions. All available time points were complex averaged before reconstruction to obtain a single 3D dataset.

5.4 RESULTS

5.4.1 SIMULATIONS

The simulations of different k-space trajectories (Figure 5.2) demonstrated a large variation in image blurring (point-spread function broadening) related to T_2^* signal decay during k-space traversal. These blurring effects were larger for longer k-space trajectories (Figure 5.2c-e) and shorter T_2^* values (Figure 5.2 bottom row). A conventional SI sequence with ultra-short TE and a minimal delay between acquisitions of different k-space points minimizes the k-space weighting (Figure 5.2a). In practice, the shortest achievable TE is limited by the gradient rise and switching times, requiring longer phase encoding gradients for larger k values. Variable phase encoding times in the 2D-UTE-SI trajectory allowed shorter TE values to be used (Figure 5.1d), leading to reduced blurring (Figure 5.2b). In the Cartesian (Figure 5.2c) and spiral trajectories (Figure 5.2d-e) blurring was clearly apparent for the short T_2^* value.
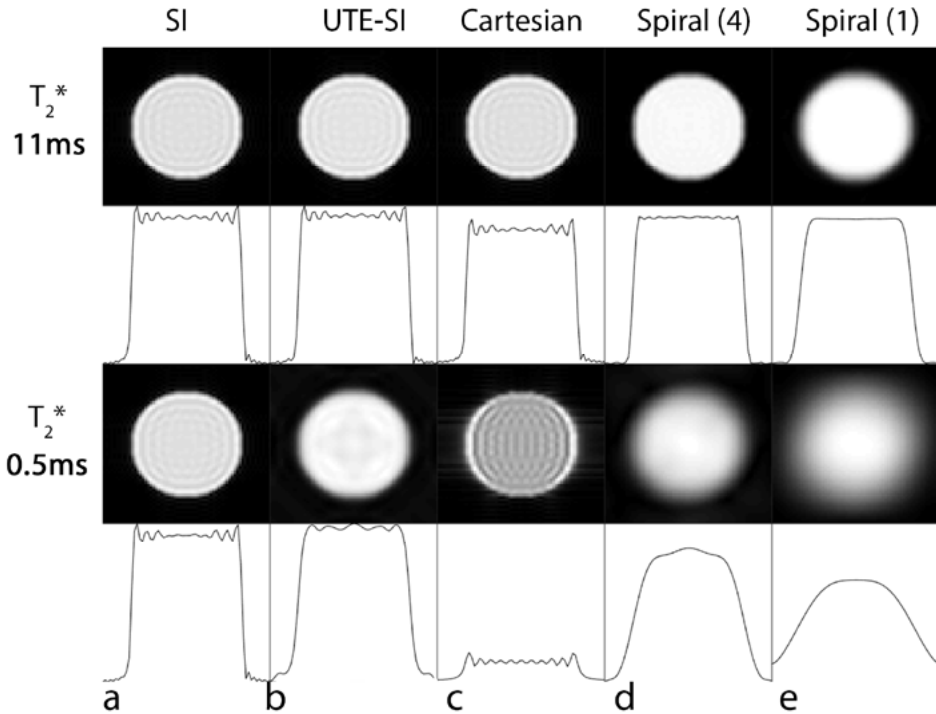
Figure 5.2: 2D-SI simulations of a sphere with 11.4 ms T_2^* (top rows) and 0.5 ms T_2^* (bottom rows) with a 16 kHz BW. The temporal signal information was used to reconstruct UTE-SI sampling (b), Cartesian sampling (c) and spiral sampling with 4 shots (d) or a single shot (e) to demonstrate the effect of T_2^* decay on the spatial resolution for both components excluding effects from reconstruction.

The accuracy of the bi-exponential T_2^* fitting procedure applied to the simulated 2D-SI data are shown in Figure 5.3 as a function of SNR. The model with fixed amplitudes led to increased error estimations in the fitted T_2^* values compared with the other two settings (free amplitudes, ratio approach) and was therefore discarded (data not shown). The fitting models with freely fitted amplitudes (Figure 5.3a-c) and amplitudes defined as a ratio of M_0 (Figure 5.3d-f) showed no major differences in the overall performance for BWs of 2 - 16 kHz (Figure 5.3a-b, d-e). In general the fitting accuracy improved across all BWs when increasing the SNR. However, when evaluating the effects of retrospective BW adaptation on fitting accuracy, differences were observed for BWs lower than 2 kHz (Figure 5.3 c,f). In these cases the standard deviation of the estimated $T_{2,short}^*$ values increased, showing decreased fitting accuracy for this component. Especially, in the SNR region of 10 - 20:1 the model with freely chosen amplitudes showed higher standard deviations than the ratio model. Therefore, all fitting procedures in this work were performed with the amplitude ratio setting. Additionally, the BW was restricted to 2 kHz for the *in vivo* fitting procedure.

Quantitatively, the ratio model resulted in mean $T_2^*{}_{,short}$ values with maximum offsets of +0.03 to +0.06 ms for all BWs with SNR>20:1. For SNR values of 10-20:1 this offset increased to +0.1 to +0.25 ms for BWs between 1 and 8 kHz, showing decreased accuracy at lower SNR (Figure 5.3b-c, e-f). The mean $T_2^*{}_{,long}$ values were determined accurately within +0.16 to +0.36 ms for SNR>20:1 and within +0.4 to +1.4 ms for SNR 10-20:1. The determined standard deviations showed a similar trend as the mean values, with decreasing variation in the fitted values for higher SNR.
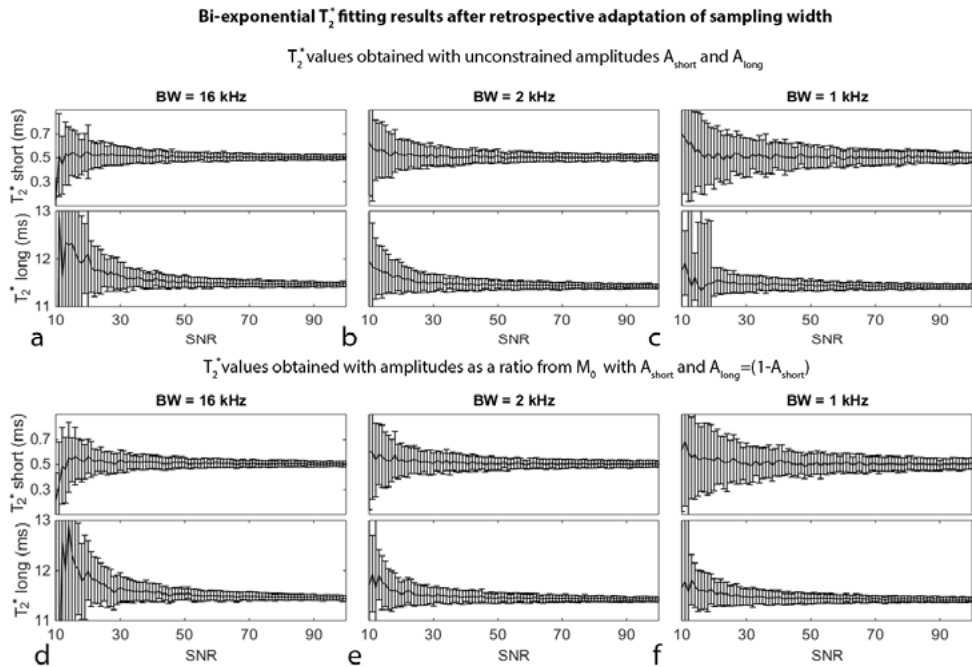
Figure 5.3: T_2^* estimates obtained from the simulated 2D-SI data using unconstrained amplitudes (a-c) or defined as a ratio from M_0 (d-f) in the bi-exponential fitting model. The SNR was varied from 10-100 and the effect of retrospective BW adjustments (b-c, e-f) on the fitting accuracy are shown.

5.4.2 PHANTOM EXPERIMENTS

3D-GRE and 3D-SI images of Phantom A are shown in Figure 5.4. The temporal signal information in the 3D-SI data was used to retrospectively adjust the sampling BW, to significantly increase the SNR (Figure 5.4d-e). After averaging the entire complex-valued 16 ms acquisition window (BW = 62.5 Hz), an increase in SNR was observed, however, at the cost of a decrease in signal at the edges of some tubes, most likely caused by T_2^* dephasing during the acquisition interval.

Figure 5.4: Phantom containing 2% agar and six tubes with varying concentrations of NaCl measured at the ^{1}H frequency (a) and [23]Na (b-e) frequency with a 3D-GRE s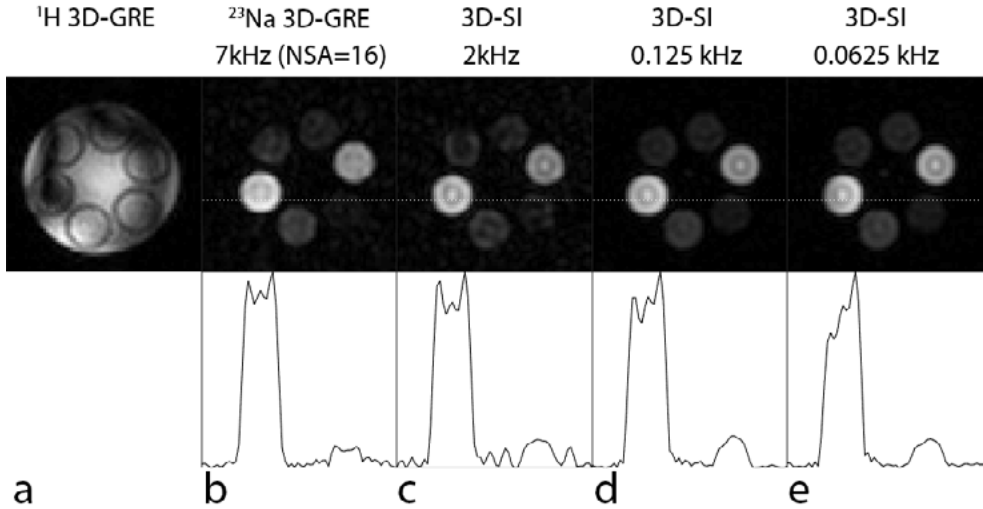equence (a,b) and a 3D-SI sequence with different BWs after complex averaging of the data (c-e). The top row show reconstructed [23]Na images and the bottom row show the intensity profile at the dashed line in b-e.

Phantom B (Figure 5.5a) was used to examine the quantitative capabilities of 3D-SI. The measured T_1 values (Figure 5.5b) in the high concentration [23]Na tubes were determined to be 38.2±0.7 ms for 2% agar (R^2=0.99±0.003), 37.1±0.3 ms for 4% agar (R^2=0.99±0.001) and 70.2±1.1 ms in H_2O (R^2=0.98±0.08). The 3D-SI data were used to reconstruct increased SNR [23]Na images (Figure 5.5c) and densely sampled decay curves (Figure 5.5e-h). The bi-exponential behavior of the [23]Na signal was clearly demonstrated by the non-linear behavior in the log magnitude plot (Figure 5.5g) and quantitatively confirmed in the fitting procedure (Figure 5.5h). Voxel-wise fitting of the data allowed the reconstruction of M_0 (Figure 5.5d), $T_2^*{}_{,short}$ (Figure 5.5i) and $T_2^*{}_{,long}$ (Figure 5.5j) maps. Amplitude ratios of 0.63/0.37 (Figure 5.5g-h) were obtained, which were close to the theoretical approximation of 0.6/0.4 (20,21). In the high [23]Na concentrations of phantom B the $T_2^*{}_{,short}$ values were found to be 8.6±1.1 ms and $T_2^*{}_{,long}$ values were found to be 40.1±4.4 ms.

The implementation of the 3D-UTE-SI sequence decreased the minimum TE from 1.98 ms (Figure 5.6b) to 0.3 ms (Figure 5.6a). This led to SNR gain as demonstrated by the increased intensity of the 3D-UTE-SI image throughout the phantom (Figure 5.6c). The effect of the variable TE weighting in k-space was illustrated by comparing images with similar TE = 1.98 ms from both the 3D-UTE-SI (Figure 5.6d) and 3D-SI (Figure 5.6e). At the same TE, the overall signal intensity did not show large differences, whereas blurring was visible at the borders of the [23]Na tubes as expected (Figure 5.6f).
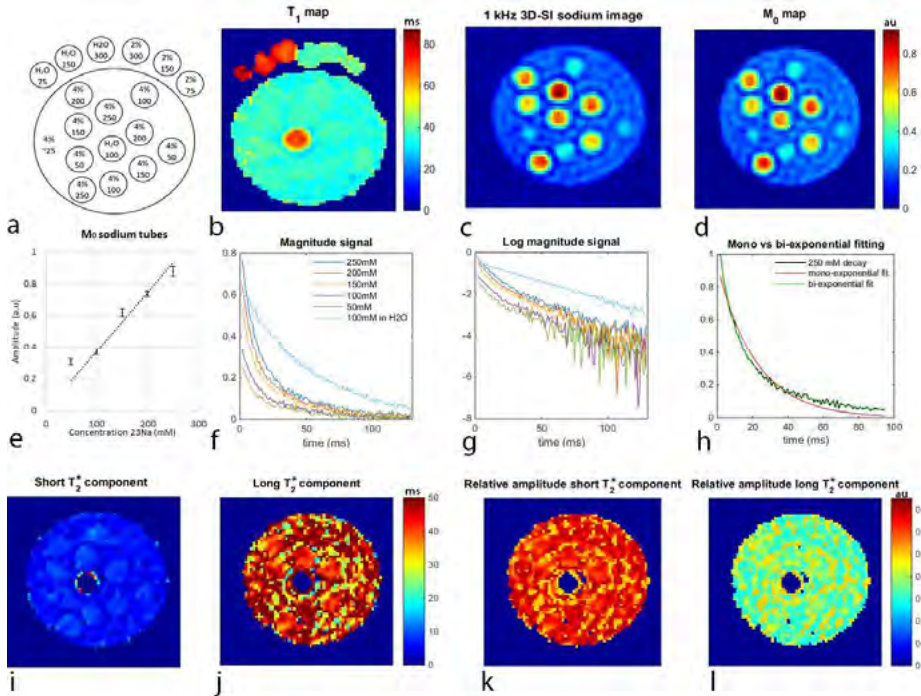
Figure 5.5: Schematic drawing of the phantom with ^{23}Na and agar concentrations (a), a T_1 map (b), 3D-SI image with BW = 1 kHz (c) and reconstructed M_0 maps (d) with the average M_0 determined from 4 slices throughout the phantom (e). The 3D-SI decay curves from the ^{23}Na tubes (f) demonstrated the bi-exponential relaxation behavior of ^{23}Na in agarose gels (f-h) and the mono-exponential decay in H_2O (center tube). All individual decay signals were fitted with a bi-exponential decay model to obtain $T_2^*{}_{,short}$ (i), $T_2^*{}_{,long}$ (j) and $M_{0,short}$ (k) and $M_{0,long}$ (l) maps. Note that voxels where no bi-exponential decay was detected were set to zero.

Figure 5.6: 3D-UTE-SI images reconstructed at the shortest TE (a), and at the TE (d) equal to the conventional SI image (b,e). The difference between the sequences (c,f) is shown to illustrate the gain in SNR due to decreased T_2^* decay (top row) and the loss in resolution due to additional T_2^* weighting in k-space (bottom row). The differences images are scaled between -10% and 10% of the maximum 3D-SI signal.

5.4.3 IN VIVO ^{23}NA IMAGING

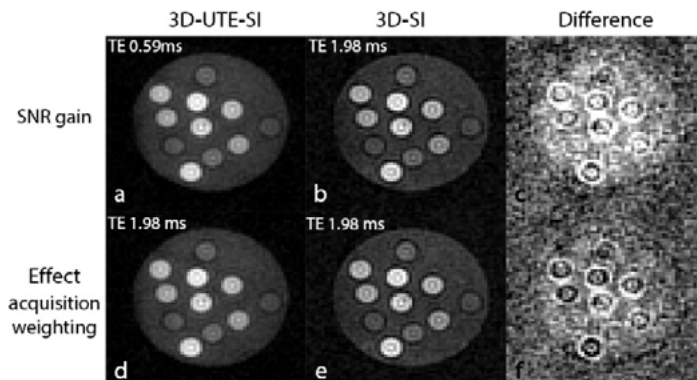^{1}H (Figure 5.7a) and ^{23}Na images (Figure 5.7b-e) of the knee were acquired to compare 3D-stack-of-spirals (Figure 5.7b) and 3D-UTE-SI (Figure 5.7c-e) sequences. The spiral trajectory (Figure 5.7b) was able to depict the cartilage regions, but suffered from increased image blurring effects as compared with the 3D-UTE-SI images (Figure 5.7c-e). Similarly to the phantom experiments, the SNR was increased by retrospectively decreasing the BW of ^{23}Na 3D-UTE-SI images *in vivo* (Figure 5.7d-e).
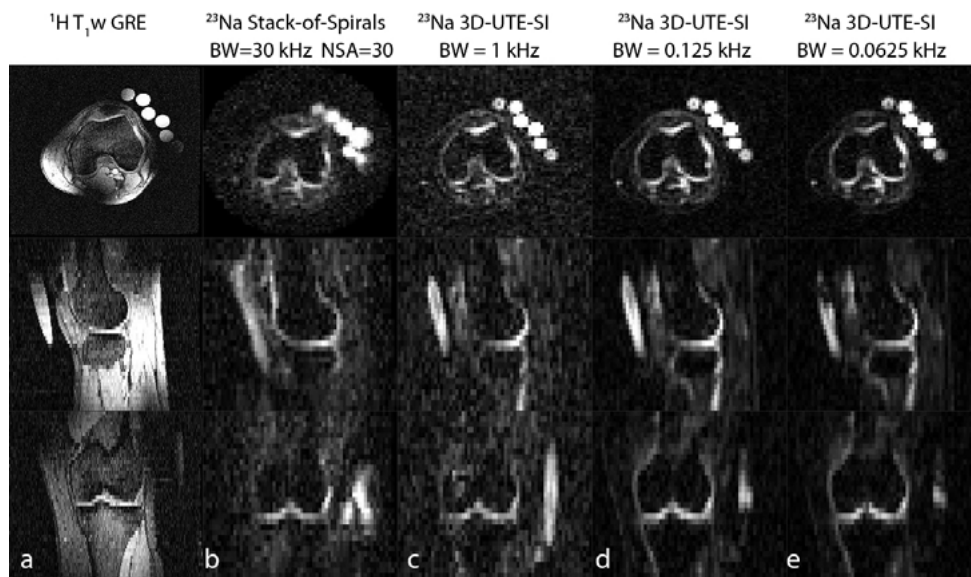
Figure 5.7: In vivo ^{1}H (a) and ^{23}Na images (b-e) acquired with spiral (b) and 3D-UTE-SI (c-e) sequences reconstructed in all planes. The BW was retrospectively adjusted in the UTE-SI data to resemble the same SNR as in the spiral sequence (c) or the maximum achievable sensitivity (d-e). The spiral data was acquired in a separate scan session, due to scan time restrictions.

The 3D-UTE-SI data from the indicated region in the patellar cartilage (Figure 5.8a) was evaluated to detect bi-exponential signal behavior *in vivo*. In a mono-exponential fitting procedure ($R^2 = 0.989$) a clear deviation between the fit and the initial part of the decay curve was observed (Figure 5.8b), which was absent when applying a bi-exponential fit ($R^2 = 0.994$, Figure 5.8c). The T_2^* maps highlight the voxels with apparent bi-exponential ^{23}Na behavior (Figure 5.8d-g) with $T_{2,short}^*$ values of 0.2-1.0 ms and $T_{2,long}^*$ values of 13-30 ms. The M_0 values in the fit were not the same for all voxels, suggesting the presence of partial volume effects. A calibration curve (Figure 5.8h) was used to obtain TSC maps (Figure 5.8i) after a correction for cartilage relaxation parameters. The calculated TSC values in cartilage ranged between 150 and 290 mM.
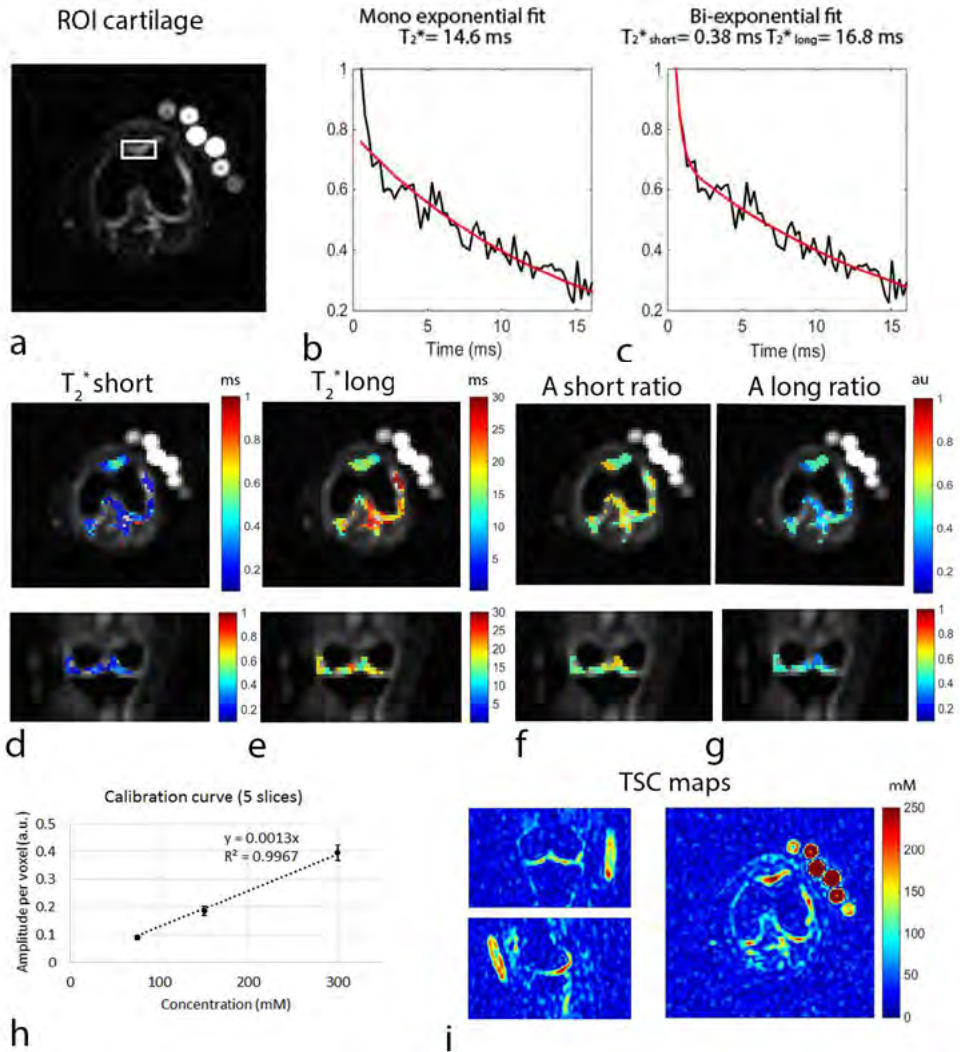
Figure 5.8: Fitting results of the in vivo 3D-UTE-SI [23]Na data (b-g) and TSC maps (i) reconstructed from the 3D-UTE-SI data. A ROI in cartilage is defined in (a) and the signal fitted with a mono- (b) or bi-exponential decay model (c). The reconstructed T_2^* maps (d-e) and amplitude ratios (g-h) from the bi-exponential fitting model are also shown for a transversal and coronal slice after voxel-wise fitting. TSC maps were obtained (i) from the calibration curve (h). The concentration axis is only valid for the cartilage regions, due to the relaxation weighting correction.

The potential for scan time reduction of 3D-UTE-SI was illustrated in Figure 5.9, showing images acquired without (Figure 5.9a) and with (Figure 5.9b) CS acceleration in the same volunteer. In a second volunteer time savings due to CS acceleration were exploited to increase TR without increasing total scan time (Figure 5.9c), which reduces the degree of T_1-weighting. The reconstruction performance and level of anatomical detail was similar for all three scans.
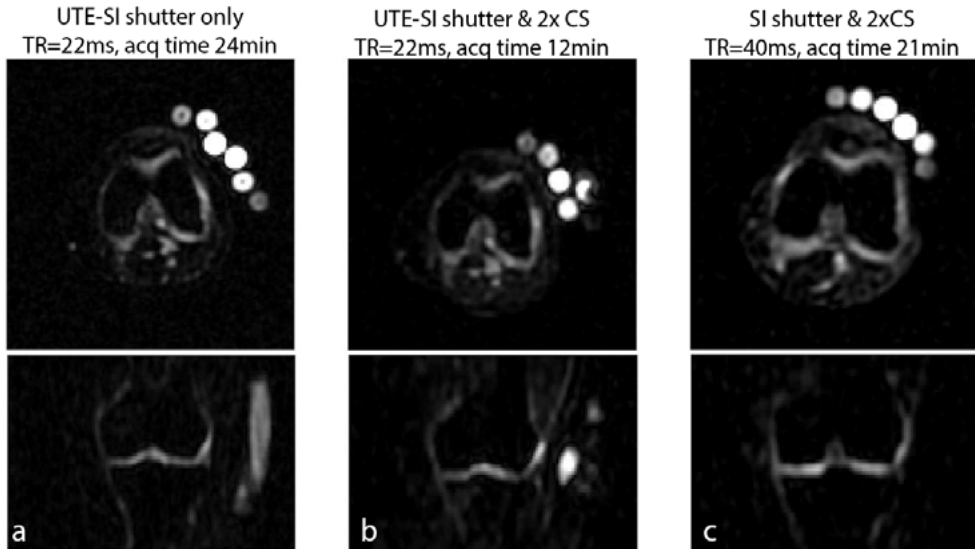
Figure 5.9: 3D-UTE-SI data acquired without (a) and with a factor 2 compressed sensing acceleration (b). CS acceleration was used to increase the TR, which is unfeasible for the non-accelerated 3D-SI acquisition with similar resolution, due to scan time restrictions (c). All images shown were reconstructed from an 8 ms acquisition window (BW = 0.125 kHz).

5.5 DISCUSSION

In this work, the shorter TE values enabled by 3D-UTE-SI were exploited for detection of bi-exponential ^{23}Na decay, TSC mapping and high SNR ^{23}Na imaging *in vivo*. Even with these improvements, the inherently low sensitivity of ^{23}Na requires careful interpretation of the data. The individual applications presented in this work are discussed below.

5.5.1 SIGNAL DECAY CHARACTERIZATION ACCURACY

Our simulation studies showed that it is possible to reduce the BW to 2 kHz to improve the SNR without compromising the bi-exponential fitting accuracy. A sufficiently high sampling BW proved to be crucial for $T_{2,\text{short}}^{*}$ detection in the knee, since the fast decaying signal can only be captured at the initial sampling points. However, for ^{23}Na studies in which the T_2^{*}

values are more accessible, such as in our phantom studies or the brain, a lower BW might not compromise bi-exponential T_2^* fitting capabilities.

Experimentally, the well-known bi-exponential relaxation behavior of [23]Na was shown in agarose and cartilage. The T_2^* values determined in the phantom study were in agreement with earlier reported values (9). The $T_2^*_{,short}$ values in cartilage of 0.2–1.0 ms were somewhat lower compared to previous reported results (12), while the T_2^* values found in the patellar cartilage region were in line with literature values. A potential confounding factor that might influence T_2^* quantification is non-physiological signal dephasing, caused for example by macroscopic field inhomogeneities. However, in the presented *in vivo* data these off-resonance effects were in the order of ~20 Hz per pixel in cartilage, which is insufficient to significantly impact the determined $T_2^*_{,short}$ values.

Another possible confounding factor is the influence of partial volume effects that can cause a mixture of multiple [23]Na compartments with different relaxation behavior, such as synovial fluid and cartilage. Partial volume effects may alter the ratio between $T_2^*_{,short}$ and $T_2^*_{,long}$, thereby hampering accurate bi-exponential fitting. Although the voxel size in this work was relatively small (3x3x5 mm) for a relaxometric study, it is likely that partial volume effects were present, based on anatomical knowledge of the cartilage regions in the knee.

5.5.2 TSC MAPPING ACCURACY

The TSC values in cartilage as found in this work ranged between 150 - 290 mM, which was largely in line with reported literature values in healthy volunteers of 259 ± 59 mM in patellar cartilage (5). Despite these apparent accurate TSC values, care has to be taken when interpreting TSC maps obtained with a short TR and non-zero TE method. Such an approach requires relaxation corrections that are based on several assumptions which, if not accurate, will lead to errors. In this work, for example, the *in vivo* relaxation correction was performed with literature T_1 values of 20 ms (12), which may be different for anatomic regions and between subjects. Additionally, the $T_2^*_{,short}$ values of cartilage may have a significant impact on the estimated M_0 values. The challenging bi-exponential fitting procedure transfers estimation errors in the T_2^* determination to the TSC mapping procedure, potentially impacting the calculated TSC values. Finally, as already elaborated on, the influence of partial volume effects in cartilage imaging can lead to contributions of synovial fluid in the measured sodium images, influencing the determined sodium concentrations in cartilage.

5.5.3 [23]NA IMAGING QUALITY

In the 3D-(UTE-)SI sequences, the time efficiency was ~0.8 ($T_{sampling}$/TR), which was in line with state-of-the-art [23]Na imaging techniques (9,10). The acquired [23]Na images showed relatively minor blurring compared with other sequences studied, due to the significantly

reduced T_2^* modulation over k-space. It should be noted, however, that for the non-Cartesian sequences no state-of-the-art k-space trajectory calibrations or off-resonance correction schemes were applied besides the standard reconstruction algorithms present on our system. Therefore, off-resonance induced blurring effects, when present, may be reduced for these sequences if state-of-the-art corrections were to be applied (9).

In this context, an additional advantage of phase-encoded sequences that was not exploited in this work, is the insensitivity of this type of spatial encoding to off-resonance related geometrical distortions (29). Off-resonance effects caused for example by imperfect shimming, the presence of air cavities in the brain or orthopedic metal objects result in geometrical distortions in the frequency encoding direction. Phase-encoded images, however, remain geometrically undistorted as long as the same phase encoding gradient time is used throughout k-space, which is done automatically in 3D-SI. Note that the 3D-UTE-SI technique as presented in this work, using different TE values for different k-space shells, is susceptible to these type of geometrical artifacts, although much less so than for long readout spiral sequences.

5.5.4 SCAN TIME ACCELERATION

CS acceleration was explored to improve the flexibility of our phase-encoded [23]Na imaging protocol with respect to acquisition time. The point-by-point sampling of 3D phase-encoded methods is perfectly suited for CS acceleration because the 3D sampling pattern can be chosen freely, a facet which was exploited to obtain a variable density sampling pattern. This approach can be further optimized to improve the reconstruction performance (30). Note however that we only performed CS reconstructions for a single high SNR 3D-dataset. For T_2^* quantification purposes dedicated model based CS reconstructions may be preferable to directly reconstruct T_2^* maps from the 4D data (31). In the case of multiple coil setups a combination of CS and parallel imaging would be an option to further improve the reconstruction quality or acquisition speed (32).

5.6 CONCLUSION

3D-(UTE-)SI has been demonstrated to be a time-efficient, flexible and quantitative [23]Na MR imaging strategy facilitating detailed characterization of the multi-exponential [23]Na signal decay related to different [23]Na compartments in biological tissues as well as TSC mapping.

REFERENCES

1. Madelin G, Lee J-S, Regatte RR, Jerschow A. Sodium MRI: Methods and applications. Prog Nucl Magn Reson Spectrosc 2014;79:14-47.
2. Ouwerkerk R, Bottomley PA, Solaiyappan M, Spooner AE, Tomaselli GF, Wu KC, Weiss RG. Tissue Sodium Concentration in Myocardial Infarction in Humans: A Quantitative 23Na MR Imaging Study1. Radiology 2008;248(1):88-96.
3. Nagel AM, Bock M, Hartmann C, Gerigk L, Neumann J-O, Weber M-A, Bendszus M, Radbruch A, Wick W, Schlemmer H-P. The potential of relaxation-weighted sodium magnetic resonance imaging as demonstrated on brain tumors. Invest Radiol 2011;46(9):539-547.
4. Ling W, Regatte RR, Schweitzer ME, Jerschow A. Behavior of ordered sodium in enzymatically depleted cartilage tissue. Magn Reson Med 2006;56(5):1151-1155.
5. Wheaton AJ, Borthakur A, Shapiro EM, Regatte RR, Akella SV, Kneeland JB, Reddy R. Proteoglycan loss in human knee cartilage: quantitation with sodium MR imaging—feasibility study 1. Radiology 2004;231(3):900-905.
6. Nielles-Vallespin S, Weber MA, Bock M, Bongers A, Speier P, Combs SE, Wöhrle J, Lehmann-Horn F, Essig M, Schad LR. 3D radial projection technique with ultrashort echo times for sodium MRI: clinical applications in human brain and skeletal muscle. Magn Reson Med 2007;57(1):74-81.
7. Nagel AM, Laun FB, Weber MA, Matthies C, Semmler W, Schad LR. Sodium MRI using a density-adapted 3D radial acquisition technique. Magn Reson Med 2009;62(6):1565-1573.
8. Staroswiecki E, Bangerter NK, Gurney PT, Grafendorfer T, Gold GE, Hargreaves BA. In vivo sodium imaging of human patellar cartilage with a 3D cones sequence at 3 T and 7 T. J Magn Reson Imaging 2010;32(2):446-451.
9. Mirkes CC, Hoffmann J, Shajan G, Pohmann R, Scheffler K. High-resolution quantitative sodium imaging at 9.4 tesla. Magn Reson Med 2015;73(1):342-351.
10. Qian Y, Panigrahy A, Laymon CM, Lee VK, Drappatz J, Lieberman FS, Boada FE, Mountz JM. Short-T2 imaging for quantifying concentration of sodium (23Na) of bi-exponential T2 relaxation. Magn Reson Med 2015;74(1):162-174.
11. Qian Y, Laymon C, Oborski M, Drappatz J, Lieberman F, Mountz J. PET ML-10 Uptake Correlates with MRI Bound Sodium Change in Early Assessment of Response to Cancer Therapy of Brain Tumors. J Nucl Med 2015;56(supplement 3):1180-1180.
12. Madelin G, Jerschow A, Regatte RR. Sodium relaxation times in the knee joint in vivo at 7T. NMR Biomed 2012;25(4):530-537.
13. Bakker CJG, van Gorp JS, Verwoerd JL, Westra AH, Bouwman JG, Zijlstra F, Seevinck PR. Multiple single-point imaging (mSPI) as a tool for capturing and characterizing MR signals and repetitive signal disturbances with high temporal resolution: The MRI scanner as a high-speed camera. Magn Reson Imaging 2013;31(7):1037-1043.
14. Pohmann R, Von Kienlin M, Haase A. Theoretical evaluation and comparison of fast chemical shift imaging methods. J Magn Reson 1997;129(2):145-160.
15. Gravina S, Cory D. Sensitivity and resolution of constant-time imaging. Journal of Magnetic Resonance, Series B 1994;104(1):53-61.
16. Webb A. Optimizing the point spread function in phase-encoded magnetic resonance microscopy. Concepts in Magnetic Resonance Part A 2004;22(1):25-36.
17. Robson MD, Tyler DJ, Neubauer S. Ultrashort TE chemical shift imaging (UTE-CSI). Magn Reson Med 2005;53(2):267-274.
18. Shapiro EM, Borthakur A, Dandora R, Kriss A, Leigh JS, Reddy R. Sodium visibility and quantitation in intact bovine articular cartilage using high field 23 Na MRI and MRS. J Magn Reson 2000;142(1):24-31.

19.   Hubbard PS. Nonexponential Relaxation of Rotating Three-Spin Systems in Molecules of a Liquid. The Journal of Chemical Physics 1970;52(2):563-568.

20.   Bull T. Nuclear magnetic relaxation of spin-32 nuclei involved in chemical exchange. Journal of Magnetic Resonance (1969) 1972;8(4):344-353.

21.   Andrasko J. Nonexponential relaxation of 23 Na+ in agarose gels. Journal of Magnetic Resonance (1969) 1974;16(3):502-504.

22.   Stöcker T, Vahedipour K, Pflugfelder D, Shah NJ. High-performance computing MRI simulations. Magn Reson Med 2010;64(1):186-193.

23.   Bouhrara M, Reiter DA, Celik H, Bonny JM, Lukas V, Fishbein KW, Spencer RG. Incorporation of Rician noise in the analysis of biexponential transverse relaxation in cartilage using a multiple gradient echo sequence at 3 and 7 Tesla. Magn Reson Med 2015;73(1):352-366.

24.   Bruin PW, Koken P, Versluis MJ, Aussenhofer SA, Meulenbelt I, Börnert P, Webb AG. Time-efficient interleaved human 23Na and 1H data acquisition at 7 T. NMR Biomed 2015;28(10):1228-1235.

25.   Haacke EM, Brown RW, Thompson MR, Venkatesan R. Magnetic resonance imaging: Wiley-Liss New York:; 1999.

26.   Henkelman RM. Measurement of signal intensities in the presence of noise in MR images. Med Phys 1985;12(2):232-233.

27.   Storey PL, Y.W.; Novikov, D.S. Artifact-free T_2^* mapping without post hoc corrections Proc Int Soc Magn Reson Med 2015;23:0442.

28.   Lustig M, Donoho D, Pauly JM. Sparse MRI: The application of compressed sensing for rapid MR imaging. Magn Reson Med 2007;58(6):1182-1195.

29.   Bakker CJ, de Leeuw H, van de Maat GH, van Gorp JS, Bouwman JG, Seevinck PR. On the utility of spectroscopic imaging as a tool for generating geometrically accurate MR images and parameter maps in the presence of field inhomogeneities and chemical shift effects. Magn Reson Imaging 2013;31(1):86-95.

30.   Zijlstra F, Viergever MA, Seevinck PR. Evaluation of Variable Density and Data-Driven K-Space Undersampling for Compressed Sensing Magnetic Resonance Imaging. Invest Radiol 2015;DOI: 10.1097/RLI.0000000000000231.

31.   Doneva M, Börnert P, Eggers H, Mertins A, Pauly J, Lustig M. Compressed sensing for chemical shift-based water–fat separation. Magn Reson Med 2010;64(6):1749-1759.

32.   Liu F, Duan Y, Peterson BS, Kangarlu A. Compressed sensing MRI combined with SENSE in partial k-space. Phys Med Biol 2012;57(21):N391-403.

^{19}F MRSI OF CAPECITABINE IN THE LIVER AT 7T USING BROADBAND TRANSMIT-RECEIVE ANTENNAS AND DUAL-BAND RF PULSES

ABSTRACT

Capecitabine (Cap) is an often prescribed chemotherapeutic agent, successfully used to cure some patients from cancer or reduce tumor burden for palliative care. However, the efficacy of the drug is limited, it is not known in advance who will respond to the drug and it can come with severe toxicity. ^{19}F MR spectroscopy (MRS) and spectroscopic imaging (MRSI) have been used to non-invasively study Cap metabolism *in vivo* to find a marker for personalized treatment. *In vivo* detection, however, was hampered by low concentrations and the use of RF surface coils limiting spatial coverage. In this work the use of a 7T MR system with radiative multi-channel transmit-receive antennas was investigated with the aim of maximizing sensitivity and spatial coverage of ^{19}F detection protocols. The antennas were broadband-optimized to facilitate both the ^{1}H (298 MHz) and the ^{19}F (280 MHz) frequency for accurate shimming, imaging and signal combination. B_1^+ simulations, phantom and noise measurements showed that more than 90% of the theoretical maximum sensitivity could be obtained when using B_1^+ and B_1^- information obtained at the ^{1}H frequency for optimizing B_1^+ and B_1^- at the ^{19}F frequency. Furthermore, to overcome the limits in maximum available RF power, while assuring simultaneous excitation of all detectable conversion products of Cap, a dual-band RF pulse was designed and evaluated. Finally, ^{19}F MRS(I) measurements were performed to detect ^{19}F metabolites *in vitro* and *in vivo.* In two patients at 10h (patient 1) and 1h (patient 2) after Cap intake ^{19}F metabolites were detected in the liver and the surrounding organs illustrating the potential of the setup for *in vivo* detection of metabolic rates and drug distribution in the body.

6.1 INTRODUCTION

Chemotherapeutic drugs are often prescribed for cancer treatment despite an unpredictable treatment outcome for the patient, undesired side-effects and high treatment cost. Ideally, the use of these drugs as well as their treatment regime should be adjustable based on the measured efficacy early during treatment to maximize quality of life, particularly in non-responding patients. However, currently no information is available how to accurately predict treatment outcome during the early treatment stages. Biomarkers that have been suggested to predict the toxicity and efficacy of chemotherapeutic agents are 1) drug trapping in the tumor and 2) the metabolic conversion rate (1-3). Therefore, it would be of great interest to measure these parameters in the human body early during treatment to further investigate their predictive value and to possibly guide treatment regimes. To achieve this goal ^{19}F MR spectroscopy (MRS) and MR spectroscopic imaging (MRSI) have been exploited in the last decades for *in vivo* monitoring of drug metabolism and determination of the spatial distribution of ^{19}F-containing anti-cancer agents (1-11). Despite the low ^{19}F concentrations present *in vivo* following treatment, ^{19}F MRS(I) has a very high specificity due to the absence of endogenous ^{19}F metabolites in the human body.

A chemotherapeutic drug that has been studied often with ^{19}F MRS(I) is 5-fluorouracil (5-FU) (1-6,8-10), which has been used in the treatment of solid tumors, head and neck, colorectal and breast cancer. Intravenous administration of 5-FU is often performed through continuous infusion or bolus injection, which gives a short time-frame in which drug metabolism can be monitored before 5-FU is fully converted through its metabolic pathways. 5-FU is activated through anabolic conversion into fluorine containing ribonucleotides or deoxyribonucleotides, which can be incorporated into DNA and RNA (12) leading to the anti-tumoral activity of 5-FU (13). In the catabolic pathway 5-FU is degraded by the enzyme dihydropyrimidine dehydrogenase into α-fluoro-ureido-propionic acid (FUPA), α-fluoro-β-alanine (FBAL) and their acid conjugates (8-10,12), clearing 5-FU from the liver and tumor. Increased catabolism in the tumor has been related to decreased efficacy of the drug (12) and is related to systemic toxicity (14). The catabolic pathway is responsible for ~80% of 5-FU conversion in the liver (15) and can be monitored using ^{19}F MRS(I). In previous studies, the 5-FU retention and metabolism have been suggested as the primary factors for clinical efficacy in various tumor types (1-3,6). However, in patients with metastasized colon carcinoma the 5-FU half-life doesn't appear to be a predictive ^{19}F MRS parameter for clinical response (10), while other ^{19}F parameters showed correlation with the clinical response (5,9). One study found a relation between the maximum 5-FU levels in liver metastases >20cm^3 and the response to treatment in a group of six patients (5). In another study, a correlation was found between the clinical response and the measured maximum concentration of 5-FU catabolites in larger tumors (>35 cm^3), which was not

found in smaller tumors (<26 cm^3)(9). The variations in clinical outcome for different tumor sizes were hypothesized to be caused by partial volume effects of healthy liver tissue in the sensitive volume of the surface coil (9) or differences in vasculature between tumors (10) and requires further research.

In recent years the pro-drug capecitabine (Cap) has been prescribed instead of 5-FU, because of its lower side-effects and easy oral administration. Unfortunately, oral administration increases the difficulty of ^{19}F MRSI detection due to the lower concentrations present and the gradual conversion of Cap into 5'-deoxy-5-fluorocytidine (5'DFCR), 5'deoxy-5-fluorouridine (5'DFUR), the active component 5-FU and its catabolites FUPA, FBAL and their acid conjugates (Figure 6.1). Two earlier published pilot studies at 1.5 and 3T have demonstrated that it was feasible to detect Cap and its catabolites in patients (7,11), while no significant amounts of 5-FU were detected. This may be due to a relatively short presence of 5-FU, due to fast conversion from 5'DFUR to 5-FU to FUPA and FBAL. To further investigate the relation between clinical response rates and different tumor sizes when giving the current therapy it will be helpful to measure Cap and as many catabolites as possible with spatially localized MRSI at a high sensitivity. Additionally, inclusion of T_1 values of the individual metabolites might enable determination of the total fluorine content in different voxels in MRSI data. This information may be used determine in- or outflow of ^{19}F in the tumor over time.
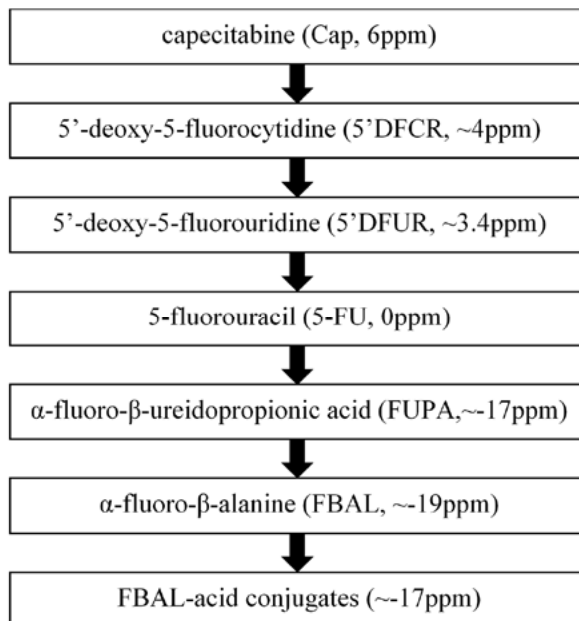

Figure 6.1: Catabolic pathway of capecitabine in vivo. Only previously reported metabolites in MRS(I) studies are shown with their respective chemical shift position in ppm.

In the previous Cap studies, a surface coil was used to detect Cap with high sensitivity in the liver. However, the sensitivity of surface coils is highest close to the coil but decreases rapidly when the distance from the coil increases, leading to a lower sensitivity in liver regions further away from the coil with very limited sensitivity in regions outside of the liver. Additionally, the obtainable RF pulse bandwidth at 3T was limited to 10 ppm in a previous study (11) requiring separate acquisitions to detect Cap (+6ppm) and FUPA/FBAL (-19ppm) frequencies. Despite promising initial results the challenging conditions (i.e. low concentrations, limited spatial coverage, limited rf bandwidth and timing of scans after drug intake) have hampered further research in humans (10).

The objective of the present study was to increase spatial coverage and sensitivity for detection of Cap and its catabolites in the liver, by introducing three improvements in the technical setup as compared with previous studies. First, a high field 7T MR scanner is utilized to maximize the SNR (SNR$\propto B_0$). Second, a single surface coil was replaced with a dedicated eight-element radiative transmit-receive antenna array (16) to increase spatial coverage for assessment of the spatiotemporal ^{19}F distribution in- and outside the liver. By using an array of broadband antennas that generate similar B_1^+ and B_1^- fields for ^{1}H and ^{19}F it is possible to accurately perform B_1 shimming and signal combination at the ^{1}H frequency, ensuring accurate B_1^+ shimming and signal combination for optimal ^{19}F detection. Additionally, ^{1}H reference spectra can be acquired to quantify the ^{19}F signals as metabolite concentrations per unit of water (17). Third, dual-band rf pulses were implemented to overcome excitation issues related to the limited available B_1^+ field. Such pulses may enable simultaneous excitation of Cap, 5'DFCR, 5'DFUR (~3-7 ppm), FUPA, FBAL, and FBAL-acid conjugates (~16-20 ppm). This is especially useful for simultaneous assessment of the kinetics of all substrates in the body.

The study was organized as follows: First, B_1^+ simulations, rf pulse simulations and phantom experiments were performed to validate the developed experimental setup and to maximize ^{19}F sensitivity using ^{1}H imaging data. Second, the setup was tested in a clinically relevant situation. To this end, two patients with liver metastases were scanned using pulse-acquire spectroscopy and spectroscopic imaging at 10 hours (patient 1) and 1 hour (patient 2) after Cap intake to detect Cap and its breakdown products *in vivo*.

6.2 METHODS

6.2.1 TECHNICAL SETUP

All experiments were performed on a 7T MR system (Philips, Best, The Netherlands) equipped with a broadband eight element radiative antenna (16)(Figures 6.2a-c, MRcoils, Drunen, The Netherlands) that was able to transmit and receive at both the ^{1}H and the ^{19}F frequency. Simulations of the B_1^+ fields of the eight individual coil elements were performed with SEMCAD (Zurich, Switzerland) at the ^{19}F (280 MHz) frequency and the ^{1}H (298 MHz)

frequency to investigate the difference in transmit and receive efficiency between the two frequencies before combining the elements. To homogenize the B_1^+ field in the liver the phase and amplitude settings for the individual B_1^+ fields were calculated to achieve constructive interference in the liver and minimize the amount of destructive interference after summation of the complex fields (Figure 6.3). The calculated phase and amplitude settings were calculated for the 298 MHz frequency and applied to the simulated 280 MHz fields to reflect the MR protocol where all preparation steps have to be performed at the ^{1}H frequency due to the very limited amount of signal at the ^{19}F frequency. In addition, potential power losses in the transmit-receive switches were investigated using S12 measurements at both 280 MHz and 298 MHz (Figures 6.2d-e, Table 6.1). Finally, the bandwidth of the antenna was verified by measuring the S parameters of the loaded antenna array at both frequencies.
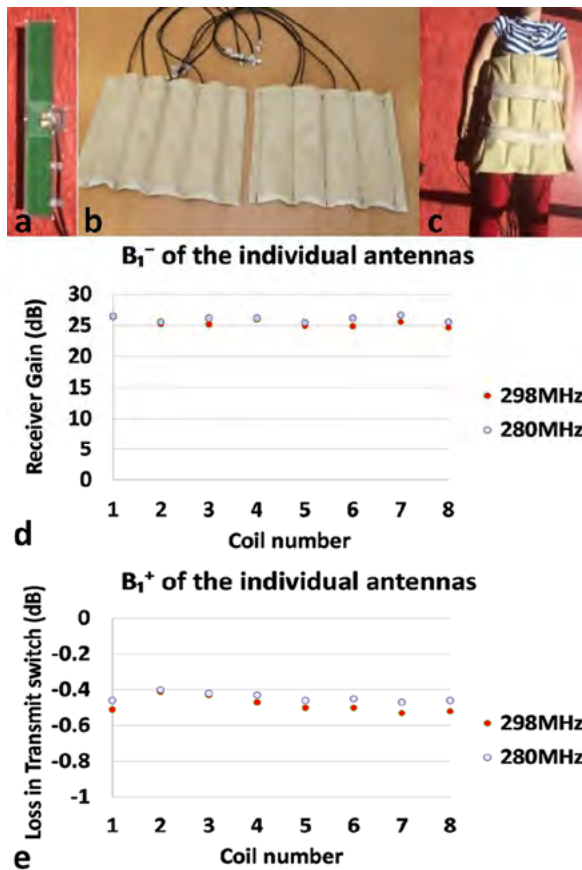
Figure 6.2: The 8 channel transmit-receive radiative antennas used in this study with the corresponding S12 parameters for each channel measured at 280 and 298 MHz are presented. A single antenna (a), all eight channels (b), the antenna positioning on the patient (c), the receiver gain (d) and the loss in transmit efficiency (e) for each channel are shown.

Simulated B$_1^+$ fields
Proton (298 MHz)   Fluorine (280 MHz)

Combined after optimization for liver

Figure 6.3: B$_1^+$ simulations for the eight channel transmit-receive radiative antennas used in this study. The individual and combined elements are shown for proton (left) and fluorine (right) frequencies. The combined B$_1^+$ fields were optimized for the liver at the proton frequency.

Table 6.1: B_1^- and B_1^+ differences of the individual antennas at the proton and fluorine frequencies

Channel	Receiver gain (voltage ratio)			Loss in transmit switch (voltage ratio)		
	280MHz	298MHz	Difference	280MHz	298MHz	Difference
1	21.13	21.13	0.0%	0.95	0.94	5.1%
2	19.05	18.41	3.4%	0.95	0.95	4.5%
3	20.42	18.20	10.9%	0.95	0.95	4.7%
4	20.42	19.95	2.3%	0.95	0.95	4.8%
5	18.84	17.78	5.6%	0.95	0.94	5.1%
6	20.42	17.58	13.9%	0.95	0.94	5.0%
7	21.63	19.05	11.9%	0.95	0.94	5.2%
8	19.05	17.18	9.8%	0.95	0.94	5.1%

Voltage ratio calculated from dB values in Figure 6.2 according to $V_2/V_1 = 10^{dB/20}$.

6.2.2 PULSE DESIGN

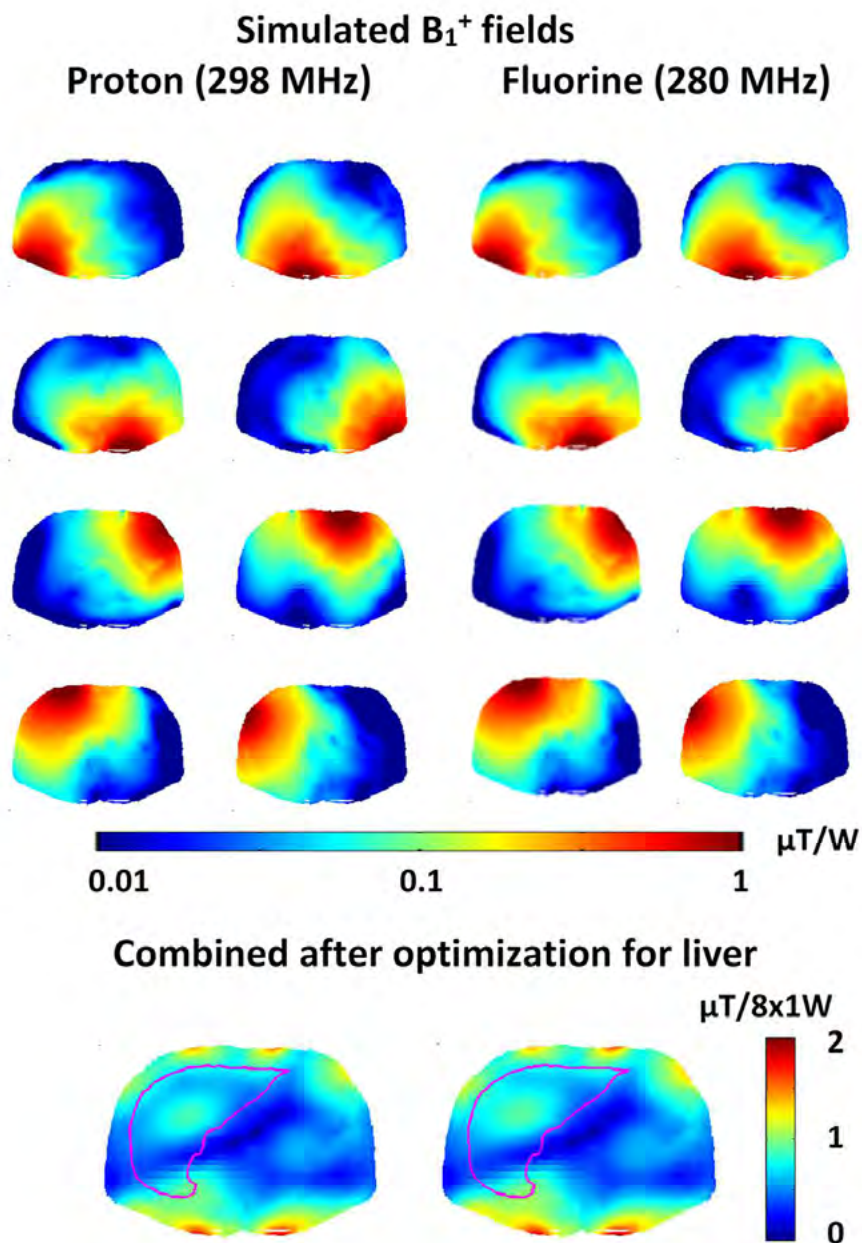To simultaneously excite Cap and its metabolites a dual-band RF pulse was designed with the Shinnar-Le Roux (SLR) algorithm in Matpulse [18] and implemented on the scanner (Figure 6.4a). The pulses were designed with the following parameters: 2.504 ms duration, 3.95 kHz (~14 ppm) separation between the edges of two spectral bins with 2.5 kHz FWHM (3.95+2*0.5*2.5 = 6.45 kHz ~ 23 ppm from center to center), 1% passband and rejection band ripple and a flip angle of 20^0. By positioning the center RF frequency at -1.82 kHz (-6.5 ppm) simultaneous excitation from the spectral regions 0.56 – 2.24 kHz (2 - 8 ppm, i.e. Cap, 5'DFCR and 5'DFUR) and -4.2 – -5.89 kHz (-15 - -21 ppm, i.e. FBAL, FUPA, conj. bile lipids) can be achieved. To experimentally confirm the simulated excitation profile multiple FIDs were acquired from a 0.38M 5-FU phantom with the f_0 ranging between -6.16 and 6.16 kHz (~-22 – 22ppm) with 0.56 kHz (~2 ppm) steps.

6.2.3 EXPERIMENTAL SETUP

Phantom experiments were performed to assess the performance of the proposed setup by observing how well the field information of a high SNR MR signal, in this case a ~25 mM ^{19}F stock solution as described below, can be used to increase the coil-combination sensitivity. To this end, we positioned a small cylindrical tube containing a fluorine compound (25 ml) in the center of an anthropomorphic phantom (40x20x25 cm) mimicking the cross-section of a human upper body. The phantom was filled with ethylene glycol and 35 g/l NaCl to obtain permittivity and conductivity values of 34 S/m and 0.4 S/m, which represent the average tissue properties in the human abdomen [19].
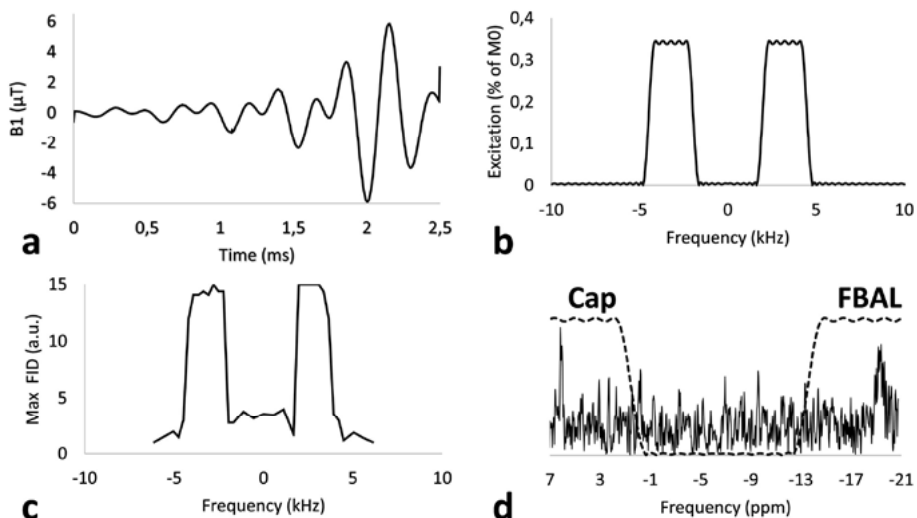
Figure 6.4: Dual-band pulse (a), simulated magnitude excitation profile (b), experimentally measured profile (c) and in vivo spectrum acquired with the dual-band pulse at 82 min after Cap ingestion (d). The simulated pulse profile is shown with a dotted line in the spectrum. The MRS spectrum in (d) was reconstructed from the highlighted coil elements in Figure 6.6 and acquired with TR=100 ms, TE= 0.46 ms, FA= 30^0.

All eight transceiver elements were wrapped around the phantom to contribute substantially to the B_1^+ and B_1^- field in the tubes. A 24.9 mM Cap (Xeloda, Roche) stock solution was made by dissolving 563 mg of a pulverized tablet (447 mg Cap) in distilled water. Similarly a 24.5 mM FBAL (Sigma-Aldrich, St Louis, MO, USA) stock solution was made by dissolving 132 mg FBAL in 50 mL distilled water. Both stock solutions were diluted to obtain 25 mL of 10 mM, 8.5 mM, 5 mM and 1 mM Cap or FBAL solutions. The 8.5 mM solution contained both 8.5 mM Cap and FBAL. Nine cylindrical 25 mL tubes with 2.5 cm diameter were filled with one of the solutions before placing them one by one in the center of the anthropomorphic phantom. Each FBAL and Cap tube was scanned individually (Figure 6.5a-c) to assess the sensitivity for the combined coil elements (Figures 6.5d-e). For the highest concentration of 25 mM three measurements were performed with varying flip angles in the center of the phantom (3, 13 and 53^0) to determine the value with the highest amplitude. The T_1 was estimated using a variable flip angle T_1 estimation approach (20). The T_2^* was estimated from a mono-exponential fit of the time signal with $M_0 \cdot exp(-TR/T_2^*)$ measured with the highest flip angle. B_0 and B_1 shimming at the location of the fluorine phantom were performed at the ^1H frequency before switching to the ^{19}F frequency. For the phantom experiments non-localized pulse-acquire spectroscopy scans were acquired in 3.5 min per scan with TR/TE=100/0.28 ms, NSA=2048, FA=53^0, 512 samples and 8000 Hz sampling rate, and the data were stored for each coil element.

Next, two patients with metastases in the liver were scanned after approval of our Medical Ethical Committee and written informed consent. The half-life of Cap was 51 min and the half-life of FBAL was 3h 13.8 min (Roche, Basel, Switzerland). To detect Cap *in vivo* we aimed to minimize the time between drug intake and ^{19}F measurements in one patient where the scan was performed 1h after drug intake. In another patient we wanted to ensure the full conversion of Cap to investigate if we were able to detect FBAL or FUPA metabolites in the liver and other organs. The patient was scanned 10h after drug intake. Both patients received 2000 mg of Cap.

Four elements were placed anteriorly and four posteriorly, covering the abdomen of the patients (Figures 6.2a-c). Non-localized pulse-acquire spectroscopy scans were performed in 3.5 min per scan with TR=100 ms, NSA=2048, 0.26 ms block pulses with nominal flip angle of 40^0 (TE=0.28 ms), 0.52 ms block pulses with nominal flip angle of 80^0 (TE=0.41 ms) or a 2.50 ms dual-band pulse with nominal flip angle of 30^0 (TE=0.46 ms) were used with 512 samples and 8000 Hz sampling rate. 3D MR spectroscopic imaging (MRSI) data were acquired in 10.7 min for ^{19}F (NSA=16) and in 40 sec for ^{1}H (NSA=1). Other acquisition parameters included: Matrix 8x8x8, voxel size 40x40x40 mm, TR/TE=100/0.66 ms, 512 samples, 8000 Hz sampling rate, 0.52 ms block pulse with nominal flip angle of 80^0.

The scan preparation at the proton frequency in both patients included the following scans: 1) Survey, 2) multi-slice gradient-echo images used for the calibration of the B_1 fields using a home-build B_1 shimtool. The B_1 shim region was manually defined in this tool, which calculated the RF phase and amplitude settings for the transmit array to homogenize the signal intensity in the defined region. The effect of the calculated pulse settings on the intensity of the magnitude images was visualized before passing these settings to the scanner, 3) survey after RF shimming, 4) B_0 maps used for linear image based B_0 shimming on a user defined region (21).

In patient 1 (scanned 10h after Cap intake) the following scans were performed after the scan preparation: 1) ^{19}F MRS at the FBAL frequency, 2) ^{19}F MRSI at the FBAL frequency, 3) ^{19}F MRS at the 5-FU frequency, 4) H_2O MRSI, 5) T_1W Turbo Field-Echo (TFE) Dixon.

In patient 2 (scanned 1h after Cap intake) the following set of scans was performed after scan preparation: 1) ^{19}F MRS at the FBAL frequency, 2) ^{19}F MRS with a single element, 3)^{19}F MRS at the Cap frequency with flip angle 40^0, 4) ^{19}F MRS at the Cap frequency with flip angle 80^0, 5) ^{19}F MRS with 30^0 dual-band pulse to excite the Cap and FBAL frequencies simultaneously, 6) ^{19}F MRSI at the Cap frequency, 7) H_2O MRSI, 8) ^{19}F MRS at the Cap frequency.

6.2.4 DATA PROCESSING

A dc correction was performed by nulling the central spike in the raw spectra before applying a gaussian apodization filter and zerofilling in the time domain. The three spatial dimensions of the spectroscopic imaging data were cosine-filtered to reduce ringing

artifacts and zero-filled in kx and ky. The raw data were corrected to match the x,y,z orientation of the scanner coordinates before creating an overlay of the anatomical image and the MRSI data in 3DiCSI (22). To ensure correct peak assignment in the MRSI data the chemical shifts of the fluorine spectra were corrected by setting the corresponding water resonance to 4.7 ppm, and using the ratio of gyromagnetic ratios (γ_{19F}/γ_{1H}=0.94) to correct for the chemical shift reference on a voxel-by-voxel basis. In patient 1, a global f_0 offset was detected, which was corrected for the full CSI dataset based on the well-known FBAL chemical shift value of 19 ppm in the liver. Additionally, a peak threshold was applied at the 99.5% confidence interval (SNR>2.8) for both the SNR determined using the gaussian noise distribution in the real signal and the rician noise distribution in the magnitude signal. The standard deviation used to calculate the confidence interval was determined in a spectral region outside of the rf excitation range. As an additional quality control the ratio between the real and magnitude standard deviations was determined since they are related according to $\sigma_{magnitude} = 0.655*\sigma_{real}$ (23).

In all datasets the data from individual coil elements were combined by complex averaging of all elements after correction of the phase offset between coils and after weighting of the signals according to their local sensitivity. To correct for the phase and weight the signals in the ^{19}F data, the phases and amplitudes of the initial point in the measured FIDs of a high SNR MR signal (~25 mM stock solution in the phantom experiments and the H_2O spectra in the *in vivo* measurements) for each coil element were used to correct the corresponding ^{19}F signal. For the MRSI experiments the corrections were performed on a voxel-by-voxel basis in the image domain. Note that at the chosen TR of 100 ms a significant T_1 saturation effect exists for the ^{1}H signal. When combining the coil elements the underlying assumption is that the amplitude and phase differences between coil elements are dominated by the coil sensitivity in a voxel and positioning of the coils relative to each other while the T_1 saturation effect is relatively constant in the liver.

6.3 RESULTS

The performance results of the individual and combined coil elements at the ^{1}H (298 MHz) and ^{19}F frequencies (280 MHz) demonstrated that the proposed setup can be used to perform shimming at the ^{1}H frequency before switching to the ^{19}F frequency (Figures 6.2-6.4, Table 6.1). The results of the S12 measurements (Figures 6.2d-e, Table 6.1) of each antenna showed only a 5% difference in receiver gain between 280 MHz and 298 MHz for channels 1-5, while the differences were within 10-14% for channels 6-8. The transmit efficiency demonstrated a loss of only 5% in the transmit-receive switches with a maximum difference of 0.7% between the channels at 280 MHz and 298 MHz.

Simulations of the B_1^+ fields (Figure 6.3) showed the similarity of the B_1^+ field patterns at 280 MHz and 298 MHz. If the amplitude weighting and phasing in combining the fields of
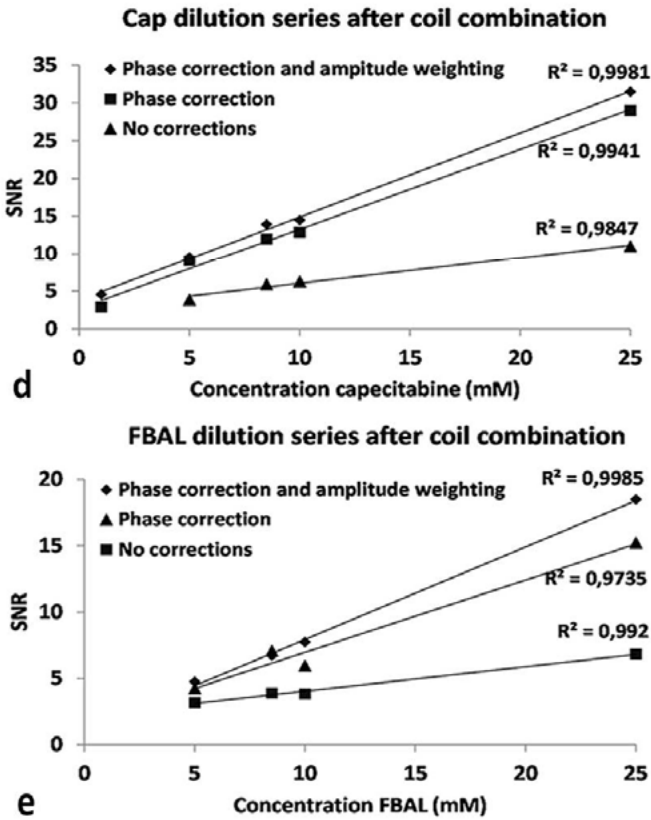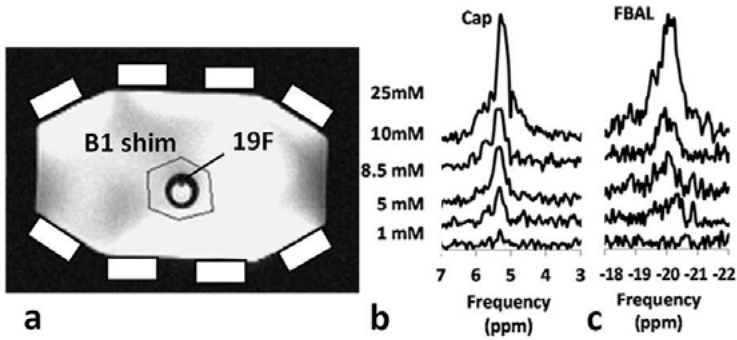
the antennas at 280 MHz was based on the 298 MHz data, a difference of ~10% was observed in B_1^+ when compared with the maximum attainable B_1^+.

In the phantom experiments the coils were placed on the body phantom (Figure 6.5a) in a similar position as in the patient measurements (Figure 6.2c). The SNR of the Cap (Figure 6.5b,d) and FBAL (Figure 6.5c,e) solutions was determined after combination of all coil elements with no corrections, a phase correction and a phase correction with amplitude weighting determined on the basis of the highest ^{19}F concentration. The SNR linearly correlated to the concentration for all methods, which was expected as only the spin density increased with concentration. However, the SNR and the slope of the curve increased after applying the phase correction and amplitude weighting, which enabled detection of the 1 mM Cap signal. The measured chemical shift of the Cap (5.5 ppm) and FBAL solutions (20 ppm) were very close to earlier reported peak positions *in vivo* (7,8). The T_1 value of Cap *in vitro* was estimated to be ~410 ms with a T_2^* of ~5 ms.

A dual-frequency pulse (Figure 6.4) was designed to excite both the Cap and FBAL regions (Figure 6.4b) in a single experiment to allow simultaneous measurements of the metabolites involved in the conversion of Cap to 5-FU (2 - 8 ppm) and the metabolites formed after conversion of 5-FU (-15 - -21 ppm). The simulated (Figure 6.4b) and experimentally measured (Figure 6.4c) frequency response profiles showed that both regions were sufficiently broad to be able to uniformly excite other previously reported ^{19}F metabolites such as FUPA (-17 ppm) and 5`DFCR/5`DFUR (3 - 4 ppm)(7).

In vivo experiments were performed following the phantom experiments. To that end, the coil elements were positioned around the body (Figure 6.6) to detect *in vivo* [19]F signals in the body after ingestion of 2000 mg Cap tablets. Resonances were clearly detected at the chemical shift position corresponding to the Cap (6 ppm, Figures 6.6 - 6.8) and FBAL frequencies (-17 - -19 ppm, Figures 6.7 - 6.8) reported in the literature (7,11) and in the performed phantom experiments. Application of the dual-band pulse 82 min after Cap ingestion enabled simultaneous detection of Cap and FBAL (Figure 6.4d) *in vivo*.

Inspection of the individual spectra acquired starting at 1h (patient 2) after Cap ingestion (Figure 6.7) clearly showed the conversion of Cap (6 ppm) into FBAL (-19 ppm), corresponding to the catabolic pathway of Cap (Figure 6.1) (24). In these spectra, both single-band and dual-band pulses were used sequentially over time. Cap signal was still detected 82 minutes after the drug intake at 6ppm, while there was also a broad resonance of FBAL detected at -19 ppm. The dual-band pulse provided information about both the Cap and FBAL peaks, giving an additional time-point at the Cap frequency. In the patient scanned 10h after Cap intake a large peak was still detectable at -16.7 ppm, corresponding to the chemical shift position of FUPA and FBAL conjugates (7), after complete metabolic conversion of Cap.

Figure 6.5: The body phantom setup with the B_1 shimming region (indicated by the hexagon) and the 19F solutions highlighted in the center (a). Cap (b) and FBAL (c) spectra from the measured concentrations are shown with a plot of the measured SNR vs concentration for both Cap (d) and FBAL (e) after combining all coil elements without corrections, with a phase correction and with a phase correction plus amplitude weighting.
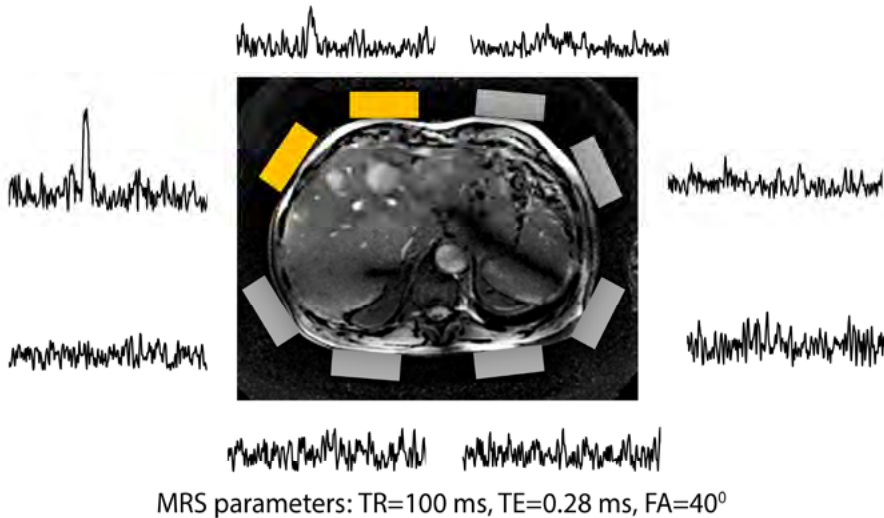
MRS parameters: TR=100 ms, TE=0.28 ms, FA=40⁰

Figure 6.6: Spectra of the separate coil elements at the capecitabine frequency. Coil elements with clear ^{19}F capecitabine signal are highlighted.

The *in vivo* distribution of ^{19}F metabolites at the FBAL (patient 1) and Cap (patient 2) frequency was obtained from the MRSI data (Figure 6.8). At 85-96 min after ingestion (patient 2) Cap (6 ppm) and 5'DFUR (4 ppm) resonances were detected, while at 10h after Cap ingestion FBAL and its conjugates were detected in the liver (patient 1). In addition to peaks in the liver we also observed a small signal in the stomach in patient 2, as based on a 99.5% confidence interval. In this and all other displayed spectra the ratio of $\sigma_{magnitude}/\sigma_{real}$ was 0.60-0.65 (theoretical value 0.655), supporting the use of the peak threshold for signal detection. The signal in the stomach could still be detected despite the non-optimized B_1^+ shim and low coil sensitivity in that area. In patient 1 signals were also observed in the kidney and spleen, where the coil sensitivity was high and no significant B_0 offsets were detected. For patient 1 we identified peaks between -15.5 to -20 ppm at multiple spatial locations, which may correspond to FUPA, FBAL-acid conjugates or/and FBAL. The non-water suppressed spectra measured at the H_2O frequency (Figure 6.8) were used to correct for peak shifting due to B_0 offsets in the ^{19}F spectra. The linewidths of the magnitude H_2O spectra in the liver with the same apodization as the ^{19}F spectra after coil combination were 120 - 200 Hz in patient 1 (10h after Cap intake) and 90 - 120 Hz in patient 2 (1h after Cap intake), which were comparable to the linewidths of the measured ^{19}F spectra (Figures 6.6 - 6.8).
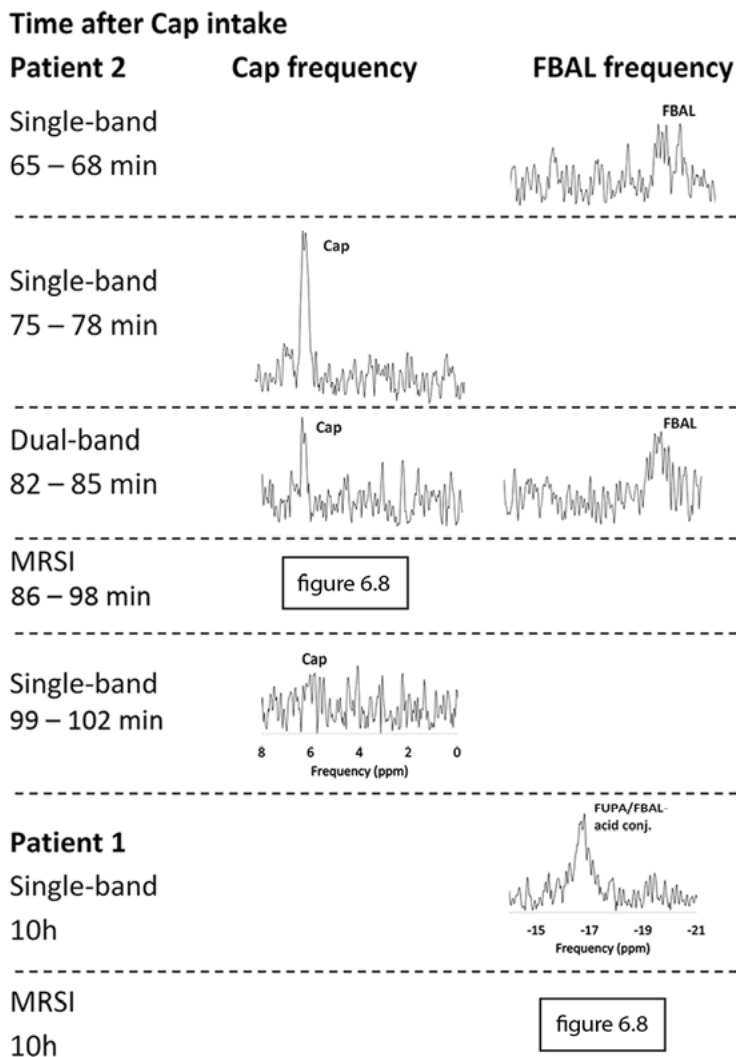
Figure 6.7: Timeline of the experiments with the resulting spectra of both patients. Measurements were performed at the Cap (left) or FBAL (right) frequency with a single-band pulse or at both frequencies using a dual-band pulse.
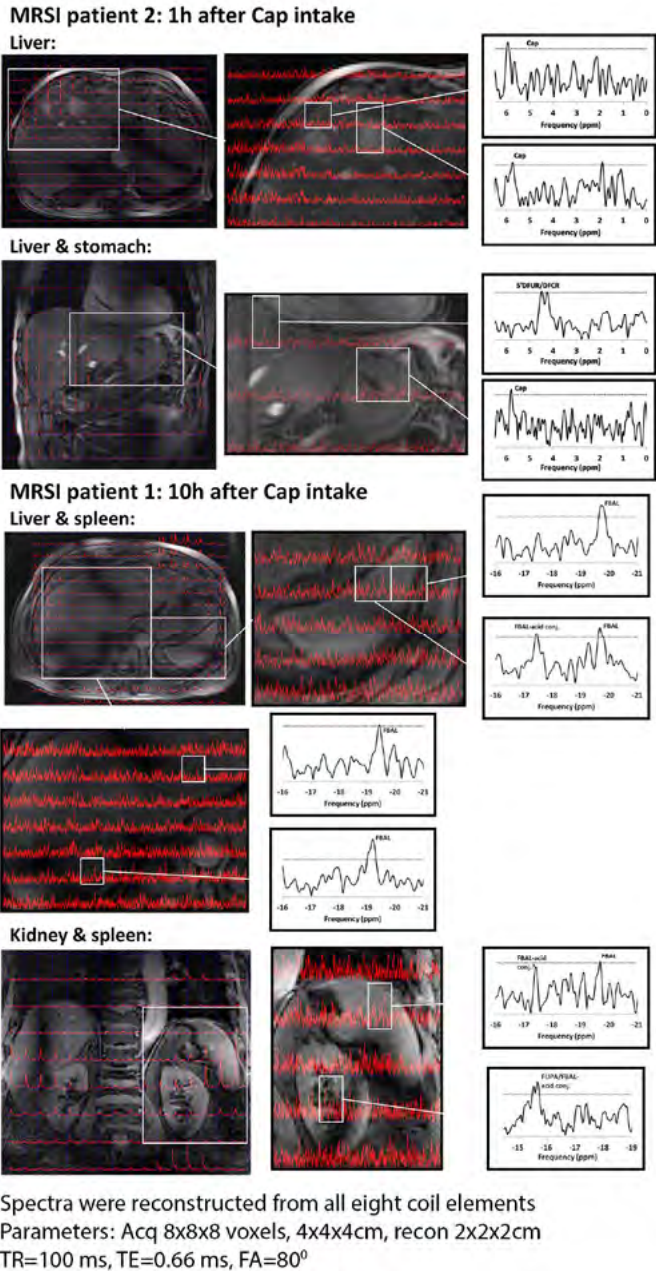
Figure 6.8: MRSI results of the two patients measured 1h and 10h after drug intake at the Cap (1h) and FBAL (10h) frequency. Anatomical images with an overlay of the measured H_2O spectra with similar processing as ^{19}F are displayed as well as a ^{19}F spectra overlay for regions of interest and selected individual ^{19}F spectra. The dotted line in the spectra indicates a 99.5% confidence interval (SNR=2.8) for the rician noise distribution. The chemical shift of the individual ^{19}F spectra was corrected for B_0 offsets using the H_2O spectra.

6.4 DISCUSSION

In this study we have demonstrated that Cap and its metabolites can be detected by utilizing a high field 7T MR system equipped with broadband radiative antennas. The presented setup was able to detect 1 mM of cap in a volume of 25 ml at the center of an anthropomorphic phantom by exploiting the phase and amplitude settings of a high SNR NMR signal measured with similar settings, such as [1]H. From these measurements it became clear that it is crucial to correct for phase offsets and use amplitude weightings to prevent loss of sensitivity when combining data of individual coil elements. This is important in view of the low SNR caused by low drug and metabolite concentrations in the body. The high field strength in combination with multiple coil elements enabled a full examination of the liver, kidneys and stomach using ^{19}F MRSI. Moreover, after administration of Cap, we could observe the clearance of this compound in the liver, as well as conversion to the products FBAL, FUPA, and conjugated FBAL.

In our study, we chose to optimize the transmit field over the liver, rather than optimizing the uniformity throughout the coil sensitivity area. This resulted in black bands in the anatomical MRI, which was acquired with the same coil, transmit amplitudes and phase settings as used in the spectroscopy scans. While more uniformity over the body is feasible, it comes at the cost of efficiency, which is undesirable because of the high spectral dispersion of the ^{19}F metabolites. Stronger RF amplifiers than the 1kW RF amplifier used in this study are likely to aid in improving the transmit field homogeneity in the future. Additionally, other groups have demonstrated the successful implementation of a higher number of transmit channels that might improve the B_1 field further (25,26), while multi-dimensional RF pulses can be exploited to compensate for the non-uniform B_1 fields to obtain uniform flip angles (27-29).

Changes in metabolic rates were detected qualitatively, which opens up possibilities for patient studies to accurately determine the spatiotemporal drug distribution, metabolic conversion rates and *in vivo* concentrations. The dual-band rf pulse appears to be especially useful for this purpose as it was able to simultaneously excite both Cap and the frequency region containing FBAL and its conjugates, which increases the temporal resolution of the experiments. A limitation of our current implementation is the lack of simultaneous detection of 5-FU (0ppm), due to the limited available bandwidth. While it is uncertain whether the concentration of 5-FU would allow detection by MRI at all, a multiband excitation as described in the PINS sequence (30) might resolve this bandwidth problem. In this study the dual-band pulses were applied in non-localized MRS acquisitions to demonstrate the feasibility with sufficient SNR. Similar as for non-localized MRS, these pulses can be applied for 3D MRSI acquisitions as well in order to increase the temporal resolution at the Cap and FBAL frequency or increase the number of signal averages to increase the SNR per unit time.

In this work, 3D MRSI with a large field-of-view was chosen for spatial localization to prevent signals from outside the liver to fold in to the region of interest. This might enable detection of metabolic alterations between metastases and liver tissue. However, alternative spatial decoding using the sensitivity profiles of the multi-channel setup might be used to distinguish signals from the liver and surrounding tissues without using MRSI, similarly as demonstrated recently in the human brain (31). Since the sensitivity profiles of the antennas can be easily obtained for each subject, this approach appears to be suitable to further maximize SNR for metabolism studies.

So far we included only two patients to demonstrate the feasibility of ^{19}F body MRSI at 7T. Accordingly, many questions regarding reproducibility, optimal timing and optimal imaging parameters remain unanswered. Nonetheless, we were already able to report many unanticipated findings as the presence of FBAL, FUPA and conj FBAL in the kidney and the spleen and a small Cap signal in the stomach. Furthermore, the chemical shift positions of FUPA, FBAL-acid conjugates and FBAL resonances were slightly shifted between voxels compared to the previously reported values of 17 and 19 ppm (7). Careful analyses of the surrounding voxels demonstrated that the resonances did not originate from voxel bleeding or ghosting. While the water scan was obtained from the same voxels and thus provides an accurate means to set the offset in the ^{19}F spectra, subtle patient motion may have occurred and could have altered the local magnetic field. However, the linewidth obtained at 7T in the voxel in the liver is narrow, and suggests a much better spectral resolution than observed in earlier studies obtained at 1.5T. The spectral resolution obtained in our study from the relatively small voxel at 7T seems even better than obtained in animal studies at higher field strengths. This may be due to the fact that susceptibility effects within the subject (i.e. within the voxel) are less pronounced in human subjects than in animals, due to the presence of air boundaries combined with the relatively small size of the animals. Finally it may be that the acidity of the biological tissue alters the chemical shift of the component (7,32).

The SNR of ^{19}F MRSI can be further improved. First of all, in vivo T_1 information of the detected metabolites could provide a more accurate Ernst angle that would improve SNR per unit time. The Ernst angle was estimated to be ~40^0 for a TR of 100 ms in the phantom setup. Effectively a ~50^0 angle was achieved in the center of the phantom which was near optimal with respect to T_1, while the acquisition window was quite long regarding the short T_2^* value of 5 ms. Decreasing the TR in combination with a lower flip angle might therefore be an option to improve the sensitivity in the future in addition to determining the T_1 values *in vivo* at 7T. Second, navigator techniques and gating may be used that will decrease the linewidth of the resonances (33). Third, ^{1}H decoupling may be applied to decrease the linewidth (34) and thereby increase the peak height of the FBAL resonance. Still, even without these optimizations, we could see chemotherapeutic drug and conversion products

in various organs located in the left and right hypochondriac and epigastric regions in the abdomen in our spectroscopic data acquired at 7T.

In this work, the application of ^{19}F MRS(I) for detecting Cap compounds was demonstrated. While we have selected patients with metastasized colon carcinoma, Cap is also used combined with lapatinib or sorafenib for the treatment of breast cancer (35-37) or with gemcitabine and sorafenib for the treatment of renal cell carcinoma (38). Further research on the metabolic conversion of such treatments might provide additional information to predict treatment outcomes or reduce toxicity in patients.

In conclusion, it is feasible to detect Cap and FBAL in patients at 7T using radiative antennas and dual-band rf pulses with a spatial coverage that extends beyond the liver. This paves the way to non-invasively study the spatiotemporal chemotherapy distribution and its chemical conversion in patients.

REFERENCES

1. Presant CA, Wolf W, Albright M, Servis K, Ring Rd, Atkinson D, Ong R, Wiseman C, King M, Blayney D. Human tumor fluorouracil trapping: clinical correlations of in vivo 19F nuclear magnetic resonance spectroscopy pharmacokinetics. J Clin Oncol 1990;8(11):1868-1873.

2. El-Tahtawy A, Wolf W. In vivo measurements of intratumoral metabolism, modulation, and pharmacokinetics of 5-fluorouracil, using 19F nuclear magnetic resonance spectroscopy. Cancer Res 1991;51(21):5806-5812.

3. Presant C, Wolf W, Waluch V, Wiseman C, Kennedy P, Blayney D, Waluch V, Wolf W, Brechner R, Presant C. Association of intratumoral pharmacokinetics of fluorouracil with clinical response. The Lancet 1994;343(8907):1184-1187.

4. Stevens A, Morris P, Iles R, Sheldon P, Griffiths J. 5-fluorouracil metabolism monitored in vivo by 19F NMR. Br J Cancer 1984;50(1):113.

5. Schlemmer H-P, Bach3ert P, Semmler W, Hohenberger P, Schlag P, Lorenz WJ, van Kaick G. Drug monitoring of 5-fluorouracil: in vivo 19 F NMR study during 5-FU chemotherapy in patients with metastases of colorectal adenocarcinoma. Magn Reson Imaging 1994;12(3):497-511.

6. Wolf W, Waluch V, Presant C. Non-invasive 19F-NMRS of 5-fluorouracil in pharmacokinetics and pharmacodynamic studies. NMR Biomed 1998;11(7):380-387.

7. van Laarhoven HW, Klomp DW, Kamm YJ, Punt CJ, Heerschap A. In vivo monitoring of capecitabine metabolism in human liver by 19fluorine magnetic resonance spectroscopy at 1.5 and 3 Tesla field strength. Cancer Res 2003;63(22):7609-7612.

8. Klomp DW, van Laarhoven HW, Kentgens AP, Heerschap A. Optimization of localized 19F magnetic resonance spectroscopy for the detection of fluorinated drugs in the human liver. Magn Reson Med 2003;50(2):303-308.

9. Kamm YJ, Heerschap A, van den Bergh EJ, Wagener DT. 19F-magnetic resonance spectroscopy in patients with liver metastases of colorectal cancer treated with 5-fluorouracil. Anticancer Drugs 2004;15(3):229-233.

10. Van Laarhoven H, Klomp D, Rijpkema M, Kamm Y, Wagener D, Barentsz J, Punt C, Heerschap A. Prediction of chemotherapeutic response of colorectal liver metastases with dynamic gadolinium-DTPA-enhanced MRI and localized 19F MRS pharmacokinetic studies of 5-fluorouracil. NMR Biomed 2007;20(2):128-140.

11. Klomp D, van Laarhoven H, Scheenen T, Kamm Y, Heerschap A. Quantitative 19F MR spectroscopy at 3 T to detect heterogeneous capecitabine metabolism in human liver. NMR Biomed 2007;20(5):485-492.

12. van Laarhoven HW, Punt CJ, Kamm YJ, Heerschap A. Monitoring fluoropyrimidine metabolism in solid tumors with in vivo ^{19}F magnetic resonance spectroscopy. Crit Rev Oncol Hematol 2005;56(3):321-343.

13. Spiegelman S, Sawyer R, Nayak R, Ritzi E, Stolfi R, Martin D. Improving the anti-tumor activity of 5-fluorouracil by increasing its incorporation into RNA via metabolic modulation. Proc Natl Acad Sci 1980;77(8):4966-4970.

14. Zhang R, Soong S, Liu T, Barnes S, Diasio S. Pharmacokinetics and tissue distribution of 2-fluoro-beta-alanine in rats. Potential relevance to toxicity pattern of 5-fluorouracil. Drug Metab Disposition 1992;20(1):113-119.

15. Heggie GD, Sommadossi J-P, Cross DS, Huster WJ, Diasio RB. Clinical pharmacokinetics of 5-fluorouracil and its metabolites in plasma, urine, and bile. Cancer Res 1987;47(8):2203-2206.

16. Raaijmakers A, Ipek O, Klomp D, Possanzini C, Harvey P, Lagendijk J, van den Berg C. Design of a radiative surface coil array element at 7 T: The single-side adapted dipole antenna. Magn Reson Med 2011;66(5):1488-1497.

17.   De Graaf RA. In vivo NMR spectroscopy: principles and techniques. Chichester: John Wiley & Sons; 2008.

18.   Matson GB. An integrated program for amplitude-modulated RF pulse generation and re-mapping with shaped gradients. Magn Reson Imaging 1994;12(8):1205-1225.

19.   van den Bergen B, van den Berg CA, Klomp DW, Lagendijk JJ. SAR and power implications of different RF shimming strategies in the pelvis for 7T MRI. J Magn Reson Imaging 2009;30(1):194-202.

20.   Wang HZ, Riederer SJ, Lee JN. Optimizing the precision in T1 relaxation estimation using limited flip angles. Magn Reson Med 1987;5(5):399-416.

21.   Schär M, Kozerke S, Fischer SE, Boesiger P. Cardiac SSFP imaging at 3 Tesla. Magn Reson Med 2004;51(4):799-806.

22.   Zhao Q PP, Arias-Mendoza F, Stoyanova R, Brown T. An interactive software for 3D chemical shift imaging data analysis and real time spectral localization and quantification. Proc Int Soc Magn Reson Med 2005;13:2465.

23.   Henkelman RM. Measurement of signal intensities in the presence of noise in MR images. Med Phys 1985;12(2):232-233.

24.   Desmoulin F, Gilard V, Malet-Martino M, Martino R. Metabolism of capecitabine, an oral fluorouracil prodrug: 19F NMR studies in animal models and human urine. Drug Metab Disposition 2002;30(11):1221-1229.

25.   Snyder C, DelaBarre L, Moeller S, Tian J, Akgun C, Van de Moortele PF, Bolan P, Ugurbil K, Vaughan J, Metzger G. Comparison between eight-and sixteen-channel TEM transceive arrays for body imaging at 7 T. Magn Reson Med 2012;67(4):954-964.

26.   Thalhammer C, Renz W, Winter L, Hezel F, Rieger J, Pfeiffer H, Graessl A, Seifert F, Hoffmann W, von Knobelsdorff-Brenkenhoff F. Two-Dimensional sixteen channel transmit/receive coil array for cardiac MRI at 7.0 T: Design, evaluation, and application. J Magn Reson Imaging 2012;36(4):847-857.

27.   Zhang Z, Yip CY, Grissom W, Noll DC, Boada FE, Stenger VA. Reduction of transmitter B1 inhomogeneity with transmit SENSE slice-select pulses. Magn Reson Med 2007;57(5):842-847.

28.   Cloos M, Boulant N, Luong M, Ferrand G, Giacomini E, Le Bihan D, Amadon A. kT-points: Short three-dimensional tailored RF pulses for flip-angle homogenization over an extended volume. Magn Reson Med 2012;67(1):72-80.

29.   Wu X, Schmitter S, Auerbach EJ, Uğurbil K, Van de Moortele P-F. Mitigating transmit B1 inhomogeneity in the liver at 7T using multi-spoke parallel transmit RF pulse design. Quant Imag Med Surg 2014;4(1):4.

30.   Norris DG, Koopmans PJ, Boyacioğlu R, Barth M. Power independent of number of slices (PINS) radiofrequency pulses for low-power simultaneous multislice excitation. Magn Reson Med 2011;66(5):1234-1240.

31.   Boer V, Klomp D, Laterra J, Barker P. Parallel reconstruction in accelerated multivoxel MR spectroscopy. Magn Reson Med 2015;DOI: 10.1002/mrm.25718.

32.   Lutz NW, Hull WE. Assignment and pH dependence of the 19F-NMR resonances from the fluorouracil anabolites involved in fluoropyrimidine chemotherapy. NMR Biomed 1999;12(4):237-248.

33.   Thiel T, Czisch M, Elbel GK, Hennig J. Phase coherent averaging in magnetic resonance spectroscopy using interleaved navigator scans: compensation of motion artifacts and magnetic field instabilities. Magn Reson Med 2002;47(6):1077-1082.

34.   Berkowitz BA, Ackerman J. Proton decoupled fluorine nuclear magnetic resonance spectroscopy in situ. Biophys J 1987;51(4):681-685.

35.   Gamucci T, Moscetti L, Mentuccia L, Pizzuti L, Mauri M, Zampa G, Pavese I, Sperduti I, Vaccaro A, Vici P. Optimal tolerability and high efficacy of a modified schedule of lapatinib–

capecitabine in advanced breast cancer patients. J Cancer Res Clin Oncol 2014;140(2):221-226.

36. Geyer CE, Forster J, Lindquist D, Chan S, Romieu CG, Pienkowski T, Jagiello-Gruszfeld A, Crown J, Chan A, Kaufman B. Lapatinib plus capecitabine for HER2-positive advanced breast cancer. N Engl J Med 2006;355(26):2733-2743.

37. Baselga J, Segalla JGM, Roché H, del Giglio A, Pinczowski H, Ciruelos EM, Cabral Filho S, Gómez P, Van Eyll B, Bermejo B. Sorafenib in combination with capecitabine: an oral regimen for patients with HER2-negative locally advanced or metastatic breast cancer. J Clin Oncol 2012;30(13):1484-1491.

38. Bellmunt J, Trigo JM, Calvo E, Carles J, Pérez-Gracia JL, Rubió J, Virizuela JA, López R, Lázaro M, Albanell J. Activity of a multitargeted chemo-switch regimen (sorafenib, gemcitabine, and metronomic capecitabine) in metastatic renal-cell carcinoma: a phase 2 study (SOGUG-02-06). The lancet oncology 2010;11(4):350-357.

DISCUSSION

7.1 GENERAL DISCUSSION

MRI is a versatile diagnostic imaging modality that can be used for non-invasive imaging of the human body. To obtain medical images that correctly represent the human anatomy, MRI requires a homogeneous main magnetic field (B_0) and linear magnetic field gradients ($G_{x,y,z}$) for spatial encoding. In practice, however, these conditions are not fulfilled, due to differences in the resonance frequency (i.e. chemical shift, endogenous susceptibility differences), foreign paramagnetic objects (i.e. orthopedic implants, surgical clips), or magnet and gradient imperfections. In current MRI sequences, the presence of these field inhomogeneities causes geometrical distortions, signal voids and signal hyper-intensities in the reconstructed medical images.

To obtain a MRI technique that is insensitive to field inhomogeneities, one can choose to replace the frequency encoding gradients with phase encoding gradients to obtain fully phase-encoded MRI techniques. In fully phase-encoded MRI, all data points contributing to a single image are acquired at a constant time after rf excitation. This results in an equal contribution of the off-resonance induced phase contributions that therefore does not interfere with the spatially dependent phase shift induced by the spatial encoding gradients. The major disadvantage of fully phase-encoded methods are the lengthy scan times that have prevented adaptation in the clinic. In pre-clinical and solid-state imaging, however, phase-encoded sequences have been used more frequently, as the favorable imaging properties of phase-encoded MRI prevail over reducing scan time. Among others, phase-encoded sequences can be designed to obtain geometrical undistorted imaging, enable accurate signal decay characterization, or perform imaging of solid state materials.

In this thesis, phase-encoded MRI was exploited for 1) geometrically undistorted imaging near metal (Chapter 2 - 3), 2) signal characterization of repetitive disturbances (Chapter 4) and 3) MR investigations of non-proton nuclei (Chapter 5 - 6). Although these topics have a very different study focus, they all benefit from the favorable geometrical properties or the unique temporal signal sampling of phase-encoded MRI. The sequences presented in this thesis showed unprecedented spatial encoding accuracy in the presence of off-resonance, high scan efficiency (sensitivity per unit time) and flexibility for multiple TE sampling. However, the long acquisition times raise questions about the clinical viability. Therefore, the use of phase-encoded sequences in clinical practice are often restricted to applications suffering from low sensitivity or substantial image artifacts, in which the unique properties outweigh the long acquisition times.

In the following sections the applicability of phase-encoded MRI will be discussed for clinical MRI in the presence of 1) endogenous field inhomogeneities (e.g. air-tissue interfaces, water-fat shift), 2) field inhomogeneities induced by foreign objects (e.g. metal implants, needles), 3) signal characterization in the temporal (e.g. T_2^* mapping, repetitive disturbances) and 4) spectral domain (e.g. MR spectroscopy).

7.2 CHEMICAL SHIFT AND SUSCEPTIBILITY OF TISSUE

In the presence of modest off-resonance effects (e.g. water-fat shift, air-tissue interfaces) frequency encoded techniques can generally be optimized such that chemical shift artifacts, geometrical distortions and T_2^* related signal loss are minimized to an acceptable level for clinical application. The most common and easiest way to reduce artifacts can be achieved by increasing the strength of the readout gradient (e.g. use a high bandwidth). More advanced methods often apply a combination of strong readout gradients, correction algorithms, reconstruction schemes and pulse sequence modifications. IDEAL (1), for example, combines the acquisition of multiple echoes with an iterative reconstruction scheme to obtain separate water and fat images with optimal noise performance in the presence of B_0 inhomogeneities. Other methods such as MARS (2) exploit spin-echo acquisitions with optimized image parameters and view-angle tilting (VAT). Additionally, off-resonance correction schemes based on field maps have been explored in the literature to retrospectively correct for field disturbances (3). Despite the limited added value of phase-encoded MRI with respect to resolving imaging artifacts in situations with modest off-resonance effects, the high temporal resolution of phase-encoded sequences remains a unique property, which has been utilized extensively in the field of MR spectroscopy (4).

7.3 METAL INDUCED SUSCEPTIBILITY GRADIENTS

In the case of the multi-kHz off-resonance effects, such as induced by metal objects, more advanced techniques are required to reduce imaging artifacts to an acceptable level. The current state-of-the-art techniques for near metal imaging have been able to decrease geometrical distortions and signal voids in the acquired images significantly by applying multispectral excitation schemes (5,6). These sequences yield satisfactory clinical image quality for most clinical research questions, therefore remaining the method of choice for standard clinical investigations. In regions very close to the metal implants, however, it is not possible to capture signal with frequency encoded techniques, due to the presence of extreme static field gradients (7).

In the presence of these extreme static field gradients one can resort to phase-encoded methods to capture signal in regions where frequency encoded methods are fundamentally limited. For these situations we developed a 3D phase-encoded turbo-spin echo (3D-PE-TSE) sequence that can potentially enable detection of (pseudo-)tumors, inflammation and metal wear close the implants (8). The method allows sampling of the decay curve on both sides of a spin echo and is flexible with respect to the choice of TE. The temporally sampled decay curve might be useful for T_2^* mapping and detection of metallic wear (9) that has been communicated a concern for metal-on-metal implants by the U.S. Food and Drug Administration (FDA) (10). The main advantages of our approach compared to the more traditional 3D single point imaging (SPI) techniques, which only provides a single

undistorted image, (11) are full sampling of the signal decay curve and improved flexibility with respect to sensitivity and $T_2(^*)$ contrast that is often desired in clinical investigations. The broadband SPI techniques, however, are much faster and can cover a much larger frequency range in a single repetition, due to the application of low flip angle excitation pulses (12).

In this thesis the scan times of phase-encoded MRI were addressed with compressed sensing reconstruction techniques, turbo acceleration and reduced field-of-view imaging for off-resonance acquisitions (Chapters 2 - 3). The combination of these different acceleration methods led to dramatically reduced acquisition times and acceptable spatial resolution in regions near metal implants where current state-of-the-art methods are fundamentally limited. To obtain a practical compromise between imaging speed and image quality in the future, a hybrid imaging method can be envisioned. Such a method would contain a combination of frequency and a phase-encoded acquisitions to cover the desired frequency range. The implementation of such a hybrid method would require additional corrections to accurately reconstruct a single dataset without signal intensity differences or misalignment of the image center between individual phase and frequency encoded acquisitions. To quickly get an estimate of the required number of frequency and/or phase-encoded acquisitions it will be useful to apply fast calibration scans before performing time demanding multispectral scans (13).

In addition to the scan time acceleration methods reported in this thesis, there a number of current technological developments that appear to be complementary to our work. Multiband rf pulses, for example, might increase the achievable rf bandwidth of 3D-PE-TSE by acquiring multiple frequency bins in a single acquisition (14). Another possibility to improve the acquisition times and flexibility of 3D-PE-TSE imaging are the use of off-resonance suppression techniques (15) that are currently being explored for fast multispectral frequency encoded imaging techniques (16). Additional modest scan time improvements might be achieved by further optimizing the gradient waveforms and amplitudes to increase the turbo factor in a single repetition.

Although phase-encoded imaging completely resolves artifacts due to geometrical distortions, other artifacts that are present in multispectral TSE techniques can still occur. Imperfect overlap of spectral bin profiles can cause a ripple-like artifact that can be reduced by altering the step size between the rf pulses. Furthermore, it has been shown that the B_1 homogeneity is also affected in the presence of metal for field strengths of 3T or higher (17). These variations are caused by finite element summations of the RF pulses, however to our knowledge no RF compensations schemes have been developed to account for these variations. Finally, the contribution of the FID signal arising from the refocusing pulses may cause additional variations of the signal intensity in multispectral imaging (8).

7.4 SIGNAL CHARACTERIZATION IN THE TEMPORAL DOMAIN

The MR signal evolution in time directly following an rf excitation pulse (the Free induction decay (FID)) enables quantification of the T_2^* decay constant. In the presence of off-resonance effects, including macroscopic field inhomogeneities and dia- or paramagnetic particles, the T_2^* is affected, making accurate quantification challenging. To determine the T_2^* relaxation rate it is necessary to obtain images at multiple TE points that can be fitted with a signal model. In situations with modest T_2^* values, such as induced by the presence of air or low concentrations of small paramagnetic particles, multi-echo gradient echo techniques are very efficient. The minimal TE and the number of echoes that can be obtained in a single acquisition are limited, however, by the duration of the frequency readout gradient. Depending on the required sensitivity, these gradients can vary between 1 - 3 ms in conventional proton imaging and up to 30 ms for sensitivity optimized sodium imaging. To accurately assess T_2^* values shorter than the readout gradient duration it is necessary to repeat the experiment multiple times with a slightly altered TE (18). This leads to a dramatic increase in acquisition time, while acquisition and analysis become more troublesome.

In these cases phase-encoded MR methods can be considered as an alternative. The temporal signal in phase-encoded methods can be sampled with a high frequency, which can be further exploited to reconstruct images at any TE value within the data acquisition window. This property was investigated for sampling of the T_2^* decay curve with high temporal resolution as well as characterization of repetitive disturbances of the MR signal (Chapter 4). In both cases the MRI scanner can be seen to act as a high speed camera, which can observe signal behavior in great detail as long as it is synchronized with the MR acquisition. In this thesis it was demonstrated that this approach holds potential for accurate signal characterization, MR system performance evaluation purposes and detection of current induced repetitive disturbances. The excellent signal characterization properties render the approach a gold standard methodology for *in vitro* and *in vivo* signal characterization.

These exploratory investigations led us to investigate the challenging situation of bi-exponential transverse signal decay of sodium (Chapter 5). The signal decay behavior of sodium reflects the overall mobility of sodium, holding information about the free and restricted sodium compartments that have been related to underlying disease (19,20). Sodium has a single dominant resonance frequency in biological tissue (21) that prevents strong chemical shift modulations in the temporal signal, which makes modelling of the signal decay curve in the temporal domain relatively straightforward. To accurately quantify the T_2^* values of sodium, both sub-ms TE values, sufficient SNR and multiple TE values are required. In this specific situation we found that phase-encoded sequences can actually be an efficient method for simultaneous T_2^* mapping, high sensitivity imaging and total sodium

concentration mapping. In this thesis a proof-of-concept was demonstrated using a 3D ultra-short TE spectroscopic imaging (3D-UTE-SI) sequence in cartilage. In principle this technique can also be applied for sodium signal characterization studies in other anatomic regions. Potential diseases where total sodium concentrations and bi-exponential decay are believed to be powerful biomarkers are osteoarthritis (22,23), myocardial infarction (24,25) and breast cancer (26). If T_2^* mapping is not required other methods might be preferable as they can obtain higher spatial resolutions (27). Alternatively, interleaved proton-sodium imaging can be used to efficiently use all available scan time for both proton and sodium imaging, when performing traditional sodium investigations (28).

Despite the recent developments of fast and efficient sodium imaging techniques there are still some issues to overcome before clinical adaptation of quantitative sodium techniques is feasible. An important requirement for clinical evaluation of quantitative sodium measurements is a consensus on the acquisition and quantification procedures to allow comparison between different studies. Furthermore, it is still unclear what parameters hold the most predictive value as a biomarker (i.e. absolute sodium concentrations, imaging contrast, bound sodium fractions). These issues are an ongoing debate in the community, which is currently being addressed through the identification of problem areas (27,29,30) and cross-validation with other imaging modalities (20).

Other areas outside of sodium imaging that benefit from the temporally resolved signal of phase-encoded imaging have been reported in the literature. Turbo-SPI, for example, has been used to perform T_2^* mapping of high concentrations of superparamagnetic iron oxide particles on animal MR systems (31). In clinical situations, similar paramagnetic particles can be encountered in specific radiotherapy treatments (e.g. Holmium microspheres) (32), or in studies of iron overload in the liver (33). These T_2^* mapping studies have a high resemblance to the study in this thesis that was aimed at detection of bi-exponential signal characterization of sodium (Chapter 5). The major difference is that the short decay constants are determined by the local T_2' decay instead of T_2. As T_2' decay can be refocused using spin-echo techniques, the 3D-PE-TSE and 2D-mSPI sequences (Chapter 2 - 4) are potentially better suited for T_2' assessment than 3D-(UTE)-SI sequences (Chapter 5).

7.5 SIGNAL CHARACTERIZATION IN THE SPECTRAL DOMAIN

The analysis of the temporally resolved signal of phase-encoded sequences is often performed in the spectral domain when data of multiple low concentration metabolites with different chemical shifts is acquired. In doing so we move from the realm of MRI to MR spectroscopy (MRS). The spectrally resolved signal has the highest SNR and can resolve small changes in the resonance frequency related to variations between the chemical environments of biological molecules. Frequency encoded techniques are often not very useful for imaging of low concentration metabolites, because many signal averages are required to obtain sufficient SNR, while substantial chemical shift artifacts can occur.

In this work the spectrally resolved signal was exploited to perform chemotherapy monitoring using fluorine (^{19}F) MRS and MRSI (Chapter 6). Fluorine is a non-native element in the human body, in contrast to sodium, that can be introduced in the body by chemotherapeutic treatments. Currently, 2D or volumetric proton measurements are used in the clinical workflow to provide a measure for tumor response to chemotherapeutic treatment (34). These volumetric measurements are often unable to separate responding from non-responding patients, leading to unnecessary toxicity effects and increased treatment costs.

The chemotherapeutic pro-drug capecitabine was investigated in this thesis, because it is an often prescribed cytostatic drug with a known mechanism of action. Capecitabine is converted in the body into the well-studied chemotherapeutic drug fluorouracil (5-FU) that is responsible for the antitumor effect. Unfortunately, MR detection of capecitabine with existing protocols is challenging, because of gradual conversion after oral administration and the low concentrations *in vivo.* The setup that was developed in this thesis enabled direct measurements of capecitabine metabolism and retention rates in the tumor (35-37) that might aid drug efficacy assessment in the future. In the current stage, however, additional clinical evidence is required to determine what parameters (i.e. concentration, retention rates, half-life, tumor size) hold the most predictive value and further investigate the reproducibility of the MR protocol.

In analogy to capecitabine, there are other fluorine containing drugs that can be investigated with the developed setup, such as anti-fungal drugs (38), anti-depressants (39) and other anti-cancer drugs (40). In applications where fluorine is mainly used as a marker for cell tracking (41) conventional MRI techniques will suffice, because multiple equivalent fluorine atoms result in a high sensitivity and a single peak can be selected to prevent chemical shift artifacts.

7.6 OTHER APPLICATIONS OF PHASE-ENCODED IMAGING

Traditionally, single-point imaging (11) and variations thereof, such as SPRITE (42) and PETRA (43) have been used for imaging of solid materials, which can have T_2 values in the order of 10-20 µs. Such sequences switch on gradients in all direction before rf excitation and acquire a single point directly after excitation, while the gradients are still on. In these sequences, the phase encoding gradients also act as a slice selection gradient that limits the flexibility with respect to reduced field of view encoding. In recent years, a combination of the original SPI techniques with a frequency encoding readout (44) has been developed for imaging of structures with very short T_2 values on a clinical MRI system. Potential applications have been reported for bone (45) and dental imaging (46). The spatial encoding gradients of the sequences mentioned in this section act more like frequency encoding gradients, because the gradients are switched on during the acquisition window. This has resulted in efficient imaging techniques with limited applications for signal characterization.

7.7 OUTLOOK

In this thesis, all phase-encoded sequences were validated in phantoms, volunteers or patients. More elaborate patient studies will be required to evaluate the clinical value of phase-encoded MRI in the fields of orthopedics and oncology. However, the initial results appear to be promising with robust performance of the sequences. Most of the developed sequences in this thesis were prototypes and require further work to provide the flexibility of full product sequences as provided by MRI vendors. Nowadays vendors are opening their reconstruction frameworks for research purposes, thereby paving the way to perform in-house development of clinically applicable sequences and protocols. In the case of non-proton investigations the hardware is often custom-build, which makes experimental design more labor intensive and less flexible than desired. Therefore it will be essential to convince vendors and clinicians with clinical evidence before broad adaptation of these techniques can be expected. Altogether we expect that phase-encoded imaging sequences will remain the method of choice for biochemical investigations with the potential to complement existing metal artifact reduction techniques in orthopedic imaging.

REFERENCES

1. Reeder SB, McKenzie CA, Pineda AR, Yu H, Shimakawa A, Brau AC, Hargreaves BA, Gold GE, Brittain JH. Water–fat separation with IDEAL gradient-echo imaging. J Magn Reson Imaging 2007;25(3):644-652.
2. Olsen RV, Munk PL, Lee MJ, Janzen DL, MacKay AL, Xiang Q-S, Masri B. Metal Artifact Reduction Sequence: Early Clinical Applications 1. Radiographics 2000;20(3):699-712.
3. Jezzard P, Balaban RS. Correction for geometric distortion in echo planar images from B0 field variations. Magn Reson Med 1995;34(1):65-73.
4. De Graaf RA. In vivo NMR spectroscopy: principles and techniques: John Wiley & Sons; 2008.
5. Koch KM, Lorbiecki JE, Hinks RS, King KF. A multispectral three-dimensional acquisition technique for imaging near metal implants. Magn Reson Med 2009;61(2):381-390.
6. Lu W, Pauly KB, Gold GE, Pauly JM, Hargreaves BA. SEMAC: slice encoding for metal artifact correction in MRI. Magn Reson Med 2009;62(1):66-76.
7. Koch KM, King KF, Carl M, Hargreaves BA. Imaging near metal: the impact of extreme static local field gradients on frequency encoding processes. Magn Reson Med 2014;71(6):2024-2034.
8. Harder dJ. Metal implant artifact reduction in magnetic resonance imaging: Technische Universiteit Eindhoven; 2015.
9. Kevin M. Koch MFK, Parina Shah, Hollis G. Potter. A mechanism for quantifiable MRI-based detection of cobalt-chromium particulate deposits near total hip replacements. Proc 23th Annual Meeting ISMRM, Toronto 2015:0310.
10. FDA. Metal-on-Metal Hip Implants: FDA safety Communication. http://wwwfdagov/MedicalDevices/Safety/AlertsandNotices/ucm335775htm 2013.
11. Emid S, Creyghton J. High resolution NMR imaging in solids. Physica B+ C 1985;128(1):81-83.
12. Ramos-Cabrer P, van Duynhoven JP, Van der Toorn A, Nicolay K. MRI of hip prostheses using single-point methods: in vitro studies towards the artifact-free imaging of individuals with metal implants. Magn Reson Imaging 2004;22(8):1097-1103.
13. Koch KM. Metal implant-induced spectral range optimization using rapid 3D-MSI calibration scans. Proc 23th Annual Meeting ISMRM, Toronto 2015:2511.
14. Artz NS, Wiens CN, Smith MR, Hernando D, Samsonov A, Reeder SB. In-Vivo Fully Phase-Encoded Magnetic Resonance Imaging in the presence of metal using multiband RF excitation. Proc 23th Annual Meeting ISMRM, Toronto 2015:3641.
15. den Harder JC, van Yperen GH, Blume UA, Bos C. Off-resonance suppression for multispectral MR imaging near metallic implants. Magn Reson Med 2015;73(1):233-243.
16. Valentina Taviani DL, Kevin M. Koch, Brian A. Hargreaves. Reduced FOV imaging near metal using 2D multispectral imaging and very selective outer volume suppression. Proc 23th Annual Meeting ISMRM, Toronto 2015:2505.
17. Graf H, Lauer UA, Berger A, Schick F. RF artifacts caused by metallic implants or instruments which get more prominent at 3 T: an in vitro study. Magn Reson Imaging 2005;23(3):493-499.
18. van de Maat GH, Seevinck PR, Bos C, Bakker CJ. Quantification of holmium-166 loaded microspheres: Estimating high local concentrations using a conventional multiple gradient echo sequence with S0-fitting. J Magn Reson Imaging 2012;35(6):1453-1461.
19. Qian Y, Panigrahy A, Laymon CM, Lee VK, Drappatz J, Lieberman FS, Boada FE, Mountz JM. Short-T2 imaging for quantifying concentration of sodium (23Na) of bi-exponential T2 relaxation. Magn Reson Med 2015;74(1):162-174.

20. Qian Y, Laymon C, Oborski M, Drappatz J, Lieberman F, Mountz J. PET ML-10 Uptake Correlates with MRI Bound Sodium Change in Early Assessment of Response to Cancer Therapy of Brain Tumors. J Nucl Med 2015;56(supplement 3):1180-1180.

21. Hubbard PS. Nonexponential Relaxation of Rotating Three-Spin Systems in Molecules of a Liquid. The Journal of Chemical Physics 1970;52(2):563-568.

22. Wheaton AJ, Borthakur A, Shapiro EM, Regatte RR, Akella SV, Kneeland JB, Reddy R. Proteoglycan loss in human knee cartilage: quantitation with sodium MR imaging—feasibility study 1. Radiology 2004;231(3):900-905.

23. Madelin G, Babb J, Xia D, Chang G, Krasnokutsky S, Abramson SB, Jerschow A, Regatte RR. Articular cartilage: evaluation with fluid-suppressed 7.0-T sodium MR imaging in subjects with and subjects without osteoarthritis. Radiology 2013;268(2):481-491.

24. Kim RJ, Judd RM, Chen E-L, Fieno DS, Parrish TB, Lima JA. Relationship of elevated 23Na magnetic resonance image intensity to infarct size after acute reperfused myocardial infarction. Circulation 1999;100(2):185-192.

25. Ouwerkerk R, Bottomley PA, Solaiyappan M, Spooner AE, Tomaselli GF, Wu KC, Weiss RG. Tissue Sodium Concentration in Myocardial Infarction in Humans: A Quantitative 23Na MR Imaging Study1. Radiology 2008;248(1):88-96.

26. Zaric O, Pinker K, Zbyn S, Strasser B, Robinson S, Minarikova L, Gruber S, Farr A, Singer C, Helbich TH. Quantitative Sodium MR Imaging at 7 T: Initial Results and Comparison with Diffusion-weighted Imaging in Patients with Breast Tumors. Radiology 2016:151304.

27. Mirkes CC, Hoffmann J, Shajan G, Pohmann R, Scheffler K. High-resolution quantitative sodium imaging at 9.4 tesla. Magn Reson Med 2015;73(1):342-351.

28. Bruin PW, Koken P, Versluis MJ, Aussenhofer SA, Meulenbelt I, Börnert P, Webb AG. Time-efficient interleaved human 23Na and 1H data acquisition at 7 T. NMR Biomed 2015;28(10):1228-1235.

29. Niesporek SC, Hoffmann SH, Berger MC, Benkhedah N, Kujawa A, Bachert P, Nagel AM. Partial volume correction for in vivo 23 Na-MRI data of the human brain. Neuroimage 2015;112:353-363.

30. Lommen J, Konstandin S, Krämer P, Schad LR. Enhancing the quantification of tissue sodium content by MRI: time-efficient sodium B1 mapping at clinical field strengths. NMR Biomed 2016;29(2):129-136.

31. Rioux JA, Brewer KD, Beyea SD, Bowen CV. Quantification of superparamagnetic iron oxide with large dynamic range using TurboSPI. J Magn Reson 2012;216:152-160.

32. Nijsen JF, Seppenwoolde JH, Havenith T, Bos C, Bakker CJ, van het Schip AD. Liver tumors: MR imaging of radioactive holmium microspheres--phantom and rabbit study. Radiology 2004;231(2):491-499.

33. Gandon Y, Olivie D, Guyader D, Aube C, Oberti F, Sebille V, Deugnier Y. Non-invasive assessment of hepatic iron stores by MRI. The Lancet 2004;363(9406):357-362.

34. Wen PY, Macdonald DR, Reardon DA, Cloughesy TF, Sorensen AG, Galanis E, DeGroot J, Wick W, Gilbert MR, Lassman AB. Updated response assessment criteria for high-grade gliomas: response assessment in neuro-oncology working group. J Clin Oncol 2010;28(11):1963-1972.

35. Van Laarhoven H, Klomp D, Rijpkema M, Kamm Y, Wagener D, Barentsz J, Punt C, Heerschap A. Prediction of chemotherapeutic response of colorectal liver metastases with dynamic gadolinium-DTPA-enhanced MRI and localized 19F MRS pharmacokinetic studies of 5-fluorouracil. NMR Biomed 2007;20(2):128-140.

36. Kamm YJ, Heerschap A, van den Bergh EJ, Wagener DT. 19F-magnetic resonance spectroscopy in patients with liver metastases of colorectal cancer treated with 5-fluorouracil. Anticancer Drugs 2004;15(3):229-233.

37. El-Tahtawy A, Wolf W. In vivo measurements of intratumoral metabolism, modulation, and pharmacokinetics of 5-fluorouracil, using 19F nuclear magnetic resonance spectroscopy. Cancer Res 1991;51(21):5806-5812.

38. Henry ME, Bolo NR, Zuo CS, Villafuerte RA, Cayetano K, Glue P, Damle BD, Andrews E, Lauriat TL, Rana NS. Quantification of brain voriconazole levels in healthy adults using fluorine magnetic resonance spectroscopy. Antimicrob Agents Chemother 2013;57(11):5271-5276.

39. Bolo NR, Hodé Y, Nédélec J-F, Lainé E, Wagner G, Macher J-P. Brain pharmacokinetics and tissue distribution in vivo of fluvoxamine and fluoxetine by fluorine magnetic resonance spectroscopy. Neuropsychopharmacology 2000;23(4):428-438.

40. Ruiz-Cabello J, Barnett BP, Bottomley PA, Bulte JW. Fluorine (19F) MRS and MRI in biomedicine. NMR Biomed 2011;24(2):114-129.

41. Srinivas M, Heerschap A, Ahrens ET, Figdor CG, de Vries IJM. 19 F MRI for quantitative in vivo cell tracking. Trends Biotechnol 2010;28(7):363-370.

42. Balcom BJ, Macgregor RP, Beyea SD, Green DP, Armstrong RL, Bremner TW. Single-Point Ramped Imaging with T1 Enhancement (SPRITE). J Magn Reson A 1996;123(1):131-134.

43. Grodzki DM, Jakob PM, Heismann B. Ultrashort echo time imaging using pointwise encoding time reduction with radial acquisition (PETRA). Magn Reson Med 2012;67(2):510-518.

44. Weiger M, Brunner DO, Dietrich BE, Müller CF, Pruessmann KP. ZTE imaging in humans. Magn Reson Med 2013;70(2):328-332.

45. Wiesinger F, Sacolick LI, Menini A, Kaushik SS, Ahn S, Veit-Haibach P, Delso G, Shanbhag DD. Zero TE MR bone imaging in the head. Magn Reson Med 2016;75(1):107-114.

46. Weiger M, Pruessmann KP, Bracher AK, Köhler S, Lehmann V, Wolfram U, Hennel F, Rasche V. High-resolution ZTE imaging of human teeth. NMR Biomed 2012;25(10):1144-1151.

SUMMARY

Magnetic resonance imaging (MRI) is a versatile diagnostic modality that has earned its place in clinical practice all over the world. MRI delivers excellent soft-tissue contrast that can be utilized to detect disease and measure physiological properties in a non-invasive manner. The MRI signal originates mainly from protons belonging to either water or fat, which are abundant in the human body. The amplitude and phase of the proton MR signal reflect disease related changes in biological tissue, such as changing water content after cell death, altered vasculature in tumors or iron overload in liver disease.

To perform diagnostic measurements with a MRI scanner, first a relation between the signal and the underlying anatomy has to be introduced. This spatial dependence of the MR signal is introduced using linear gradients. The spatially encoded signals can then be transformed into medical images with a mathematical operation (Fourier transformation). As long as the main magnetic field is homogeneous this methodology leads to accurate localization of the MR signal, resulting in MR images with high diagnostic quality. In cases of inhomogeneous magnetic fields, the spatial encoding process is affected, resulting in severe image artifacts and altered MR signal behavior. Potential sources of these so-called off-resonance effects are local changes in the main magnetic field, differences in magnetic susceptibility of tissues, chemical shift differences and the presence of paramagnetic materials.

In this thesis, the aim was to develop MRI techniques that can be exploited for geometrically undistorted imaging (**Part I**) and signal characterization (**Part II**) in the presence of off-resonance effects. The appearance of off-resonance induced image artifacts depends on the interaction between the spatial encoding gradients and the off-resonance fields. The resulting artifacts can therefore be manipulated by changing the order, timing and strength of the spatial encoding gradients. In the spatial encoding process, a distinction can be made between three types of spatial encoding gradients: 1) gradients that are activated simultaneously with data acquisition (frequency encoding), 2) gradients that are applied before data acquisition (phase encoding) and 3) gradients that are applied during radiofrequency (rf) excitation pulse (slice selection).

Of the three types of spatial encoding, frequency encoding and slice selection are the most efficient, as they can encode an entire spatial dimension and reduce the encoding volume from 3D to 2D, respectively. Currently, frequency and slice encoding are a part of most clinical MRI sequences, because the time per patient is limited and fast sequences are more cost efficient. Unfortunately, both frequency and slice encoding are susceptible to off-resonance effects that can cause geometrical distortions, signal voids and signal hyperintensities. These artifacts do not accurately reflect anatomical information in the reconstructed images and can reduce the diagnostic quality significantly.

A clinical example can be found in the field of orthopedics where metal implants are encountered after knee or hip arthroplasty, which severely degrade the image quality in post-operative imaging. In such cases, fully phase-encoded MRI techniques can be considered as they do not suffer from geometrical distortions, because the process of spatial encoding and data acquisition are separated. Despite the unprecedented image quality, these fully phase-encoded MRI sequences do require substantial longer acquisition times. This is a problem that has to be addressed before clinical application might be feasible.

In addition to the image quality, the MRI signal decay (e.g. T_2, T_2^* relaxation) is also influenced by the presence of off-resonance effects. In contrast to the unwanted effects of off-resonance effects on the image quality, detection of changes in the MRI signal behavior can hold valuable diagnostic or therapeutic information, such as the concentration of paramagnetic particles in tissue (i.e. iron deposits, brachytherapy seeds, Holmium microspheres). In the case of large concentrations, however, this can lead to very fast signal decay that is hard to quantify with conventional MRI methods. To accurately detect these high concentrations it is necessary to measure multiple points in time that can be analyzed to determine the T_2^* relaxation time. In frequency encoded MRI sequences this can be difficult, because the duration of the readout gradient is often multiple milliseconds while the signal decay can be much faster. To obtain a large number of time points with very short time steps for quantification of T_2^* it is possible to separate the spatial encoding gradients from the data acquisition window, as is done in phase encoding.

In this thesis the aim was to exploit the unique properties of phase-encoded MRI sequences to address unmet medical needs in orthopedic and oncological imaging. In the first part of this thesis the metal induced image distortions near orthopedic implants were investigated. In clinical practice, these image distortions can lead to inaccurate diagnosis or obscure clinically relevant information, such as the detection of implant loosening, (pseudo-) tumors, inflammation or metallic wear. To prevent these artifacts we proposed the use of fully phase-encoded MRI sequences, albeit at the cost of significantly lengthened scan times.

In **Chapter 2** a first step was made towards clinically acceptable acquisition times for fully phase-encoded MRI near orthopedic implants. For this purpose a 3D phase-encoded turbo-spin-echo (3D-PE-TSE) sequence was combined with compressed sensing (CS), an iterative reconstruction scheme that exploits redundancy in the MRI methodology. The proposed method decreased the original acquisition time of 3D-PE-SE by a factor of 60, enabling the acquisition of geometrically undistorted 3D *in vivo* data within 10 minutes.

In these experiments a phantom containing a titanium implant was used to evaluate the potential of fully phase-encoded MRI for artifact reduction. Despite the strong susceptibility induced gradients near titanium it was possible to obtain geometrically accurate images and detect signal close to the implant in a single acquisition. In this experiment the majority of

the signal was excited by maximizing the radiofrequency (rf) bandwidth (~3 kHz). In the case of larger field-offsets, such as caused by cobalt-chromium or stainless steel implants, it was necessary to perform multiple acquisitions with different frequency offsets to capture all signal. In the current state-of-the-art MRI sequences for imaging near metal, a multispectral excitation scheme is applied to reduce image distortions in the presence of field inhomogeneities. While these sequences have been demonstrated to significantly reduce image distortions, they still suffer from image artifacts close to orthopedic implants due to fundamental limitations related to the spatial encoding process.

In **Chapter 3** both multispectral frequency encoded 3D-TSE and phase-encoded 3D-PE-TSE sequences were implemented to compare the imaging performance (i.e. artifact reduction, scan time, signal characterization) for a large frequency range of 40 kHz. The methods were compared in a phantom study using a cobalt-chromium knee implant that is representative of the strong paramagnetic materials encountered in post-operative orthopedic imaging. The results showed that the (multispectral) 3D-PE-TSE sequence was able to prevent hyper-intensity artifacts and signal voids near the cobalt-chromium implant that were still present in multispectral 3D-TSE images. For a 10 kHz off-resonance acquisition it was possible to reduce the scan time of 3D-PE-TSE to ~3.5 min by combining reduced field of view imaging and k-space undersampling. The presented results demonstrated the feasibility of multispectral 3D-PE-TSE to selectively image the regions close to the orthopedic implants within a reasonable timeframe.

In the second part of this thesis, the temporal and spectral properties of phase-encoded sequences were exploited to study MR signal behavior. In **Chapter 4**, an exploratory study was performed to investigate the possibilities for MR signal characterization with phase-encoded MRI sequences. For this purpose, a 3D frequency encoded sequence was adapted to a 2D phase-encoded sequence with an additional dimension containing the MR signal evolution through time. Instead of using the signal evolution to study the frequency content, as is done in spectroscopic imaging, it was utilized to study repetitive disturbances of the MR signal. The 2D multiple single-point imaging (mSPI) method was used to characterize T_2^* decay, gradient induced signal perturbations and current induced phase differences. Potential applications of the presented method include accurate T_2^* mapping, system performance evaluation and detection of the induced phase by external stimuli, such as induced by transcranial magnetic stimulation.

The T_2^* mapping capabilities were further exploited for signal characterization of sodium (^{23}Na), which plays an important physiological role in the human body (i.e. maintaining cell integrity and propagation of nerve impulses). Altered sodium concentrations and signal behavior are thought to be biomarkers for early disease detection, such as early onset of osteoarthritis and tumor formation. Quantitative parameters that can be measured with MRI are the total sodium concentration and the bi-exponential T_2^* relaxation. These parameters have been related to a compromised biological structure and cellular integrity.

Unfortunately, it is difficult to accurately quantify the sodium T_2^* values with conventional methods (e.g. multi gradient-echo), due to the low MR sensitivity of sodium and the presence of a very short T_2^* component (~0.5 - 3.0 ms). To accurately determine the T_2^* values with frequency encoded techniques, numerous signal averages and additional data points in time are required, which both significantly increase the scan time.

In **Chapter 5** a flexible phase-encoded method was implemented to perform sodium imaging, mapping of sodium concentrations and bi-exponential T_2^* measurements in a single acquisition. Both conventional and ultra-short echo time (UTE) 3D phase-encoded methods were implemented and evaluated *in vitro* and *in vivo*. This enabled accurate mapping of the bi-exponential signal behavior *in vivo*, with higher effective spatial resolution than reported previously for frequency encoded methods. The presented methods proved to be time-efficient for the specific case of sodium relaxation mapping, due to the excellent sensitivity properties of phase-encoded imaging in combination with sub-millisecond sampling of the decay curve.

Instead of analysis in the temporal domain it is also possible to study the frequency content of the MR signal to detect biological changes on the molecular level. In the field of MR spectroscopy (MRS) this property has been explored extensively to obtain information about metabolism, brain biochemistry, muscle function and many other applications focused on naturally abundant molecules in the body. An exception can be found in the field of fluorine (^{19}F) MRS that has no natural occurrence in the human body, but can be introduced in the form of pharmaceutical drugs or molecular markers. This makes fluorine MRS a very specific method for non-invasive monitoring of drug metabolism and drug distribution. Ideally, these parameters can be used as markers for drug efficacy assessment to improve the predictive strength of current methodologies. The main goal of this line of work is to decrease toxicity effects for non-responding patients and reduce treatment costs. However, in its current stage it is challenging to perform robust fluorine experiments, because of the extremely low concentrations after drug intake (mM range) in combination with specific hardware requirements.

In **Chapter 6**, a new setup was presented to measure the metabolism and distribution of the chemotherapeutic pro-drug capecitabine in the liver and surrounding organs. In this chapter three potential improvements for *in vivo* capecitabine detection were investigated. First, a high field 7T MR scanner with a 3D phase-encoded sequence was used to increase the sensitivity of fluorine detection. Second, an eight-channel transmit-receive antenna was utilized to increase the spatial coverage from a part of the liver to full coverage of the liver and surrounding organs. Third, a dual-band rf pulse was designed to simultaneously measure the drug and its metabolites for metabolism studies. The described setup was able to detect capecitabine in the liver and stomach and its breakdown products in the liver, kidneys and spleen. These findings significantly increase the possibilities for fluorine detection of capecitabine that was previously only feasible in a sub-section of the liver.

The chapters in this thesis illustrate the versatility of phase-encoded MRI sequences and the broad applicability in many MRI research areas. Phase-encoded MRI proved to be a robust alternative for frequency-encoded methods in the presence of field inhomogeneities (Chapter 2 - 3), MR signal characterization (Chapter 4 - 6) and low sensitivity (Chapter 5 - 6). The future perspectives for development and application of phase-encoded sequences were discussed in **Chapter 7**. Although the reported results in this thesis are mostly technical in nature and require additional clinical validation in patient groups, they were promising and are useful as a stepping stone for future work.

Based on the methodology and results presented in this thesis, phase-encoded MRI appears to be a viable strategy for geometrically undistorted imaging near metal implants and signal characterization of nuclei (^{23}Na, ^{19}F) with a low MR sensitivity.

Nederlandse samenvatting

Magnetic resonance imaging (MRI) is een veelzijdige diagnostische modaliteit die wereldwijd een vaste plek heeft veroverd in de kliniek. MRI staat bekend om zijn excellente contrast van zacht biologisch weefsel dat gebruikt wordt om ziektes en fysiologische veranderingen te detecteren op een non-invasieve manier. Het MRI signaal bestaat voornamelijk uit water en vet dat in grote mate aanwezig is in het menselijke lichaam. De amplitude en fase van het MR signaal reflecteren veranderingen in biologisch weefsel die gerelateerd zijn aan ziekte, zoals veranderende waterconcentraties na celdood, aanpassingen in de bloedvaten bij tumoren of hoge ijzerconcentraties in leverziektes.

Om diagnostische metingen te kunnen maken met een MRI scanner moet er eerst een relatie gelegd worden tussen het MR signaal en de onderliggende anatomie. Deze spatiële afhankelijkheid van het MR signaal wordt geïntroduceerd door middel van lineaire gradiënten. De spatieel gecodeerde signalen kunnen daarna gereconstrueerd worden als medische beelden door middel van een mathematische operatie (Fourier transformatie). Als het magnetische veld van de MRI scanner homogeen is zal deze methode leiden tot accurate lokalisatie van het MR signaal wat resulteert in beelden met een hoge diagnostische kwaliteit. In het geval van inhomogene magneetvelden zal het spatiële coderingsproces aangetast worden, waardoor ernstige beeldartefacten kunnen ontstaan en de signaaleigenschappen veranderen. Potentiële oorzaken van deze veldinhomogeniteiten zijn lokale veranderingen in het magnetische veld, verschillen in de magnetische susceptibiliteit van weefsels, effecten van de biochemische omgeving, en de aanwezigheid van paramagnetische materialen.

In dit proefschrift was het doel om MRI technieken te ontwikkelen die gebruikt kunnen worden voor geometrische onverstoorde beeldvorming (**Deel I**) en signaalkarakterisering (**Deel 2**) in de aanwezigheid van veldinhomogeniteiten. De manier waarop beeldartefacten zich manifesteren in de aanwezigheid van veldinhomogeniteiten hangt af van de interactie tussen de spatiële coderingsgradiënten en de inhomogene magnetische velden. De beeldartefacten kunnen dan ook gemanipuleerd worden door de volgorde, timing en sterkte van de spatiële coderingsgradiënten aan te passen. In dit proces kan een onderscheidt gemaakt worden tussen drie types spatiële coderingsgradiënten: 1) gradiënten die tegelijk met de data acquisitie aangezet worden (frequentiecodering), 2) gradiënten die aangezet worden voordat de data wordt gemeten (fasecodering) en 3) gradiënten die aangezet worden tijdens de radiofrequentie (rf) excitatiepuls (slice selectie).

Van de drie types spatiële codering zijn frequentiecodering en slice selectie het efficiëntste, omdat deze respectievelijk een gehele spatiële dimensie kan coderen en het te coderen volume kan verkleinen van 3D naar 2D. Op dit moment bevat het merendeel van klinische MRI sequenties zowel frequentiecoderingsgradiënten als slice selectiegradiënten vanwege de beperkte beschikbare tijd per patiënt en de hogere kosteneffectiviteit. Helaas zijn zowel de frequentiecodering als slice selectie gradiënten gevoelig voor verstoringen van het magnetische veld wat kan resulteren in geometrische vervormingen, signaalverlies en signaalhyperintensiteit in de gereconstrueerde beelden. Aangezien deze artefacten geen weerspiegeling zijn van de onderliggende anatomie kunnen ze de diagnostische kwaliteit sterk verminderen. Een klinisch voorbeeld dient zich aan in de orthopedische beeldvorming waar metalen implantaten gebruikt worden in knie- en heupartroplastiek wat betrouwbare postoperatieve beeldvorming in de weg staat. In dergelijke situaties kunnen volledig fasegecodeerde MRI technieken overwogen worden. Deze technieken hebben geen last van geometrische vervormingen en signaalophopingen in de buurt van veldinhomogeniteiten, omdat het spatiële coderingsproces en de data acquisitie gescheiden zijn. Ondanks de ongeëvenaarde beeldkwaliteit vereisen deze volledig fasegecodeerde technieken wel een veel langere scantijd. Dit is een belangrijke beperking die geadresseerd moet worden voordat deze technieken geschikt zijn voor klinische toepassingen.

Naast de beeldkwaliteit wordt het MRI signaalverval (e.g. T_2, T_2^* relaxatie) ook beïnvloed door de aanwezigheid van veldinhomogeniteiten. In tegenstelling tot de ongewenste effecten van veldinhomogeniteiten op de beeldkwaliteit kan het effect op het signaalverval benut worden om waardevolle diagnostische of therapeutische informatie te verkrijgen, zoals concentratiebepaling van paramagnetische deeltjes (i.e. ijzerdepots, brachytherapie zaden, Holmium microsferen). Voor hoge concentraties paramagnetische deeltjes kan dit echter zorgen voor een zeer snel signaalverval waardoor het lastig is om tot een accurate kwantificatie te komen met conventionele MRI methodes. Om hoge concentraties accuraat te kunnen detecteren moeten meerdere datapunten in de tijd gemeten worden waaruit de zogenaamde T_2^* relaxatietijden bepaald kunnen worden. Dit kan lastig zijn met frequentiegecodeerde technieken vanwege de relatief lange frequentiecoderingsgradiënt die enkele milliseconden kan duren, terwijl de T_2^* vele malen korter kan zijn. Door de spatiële coderingsgradiënten te scheiden van de data acquisitie, zoals in fasegecodeerde MRI sequenties, kan een grote hoeveelheid tijdspunten gemeten worden met binnen een kort tijdsinterval waardoor T_2^* kwantificatie van snel signaalverval mogelijk wordt.

In dit proefschrift zijn de unieke eigenschappen van fasegecodeerde MRI onderzocht voor toepassingen in voornamelijk de orthopedische en oncologische beeldvorming. In het eerste deel van dit proefschrift werden de mogelijkheden voor beeldvorming in de buurt van orthopedische implantaten onderzocht. Indien frequentiegecodeerde MRI beelden gemaakt worden in de buurt van deze metalen implantaten ontstaan er verschillende beeldartefacten die gerelateerd zijn aan vervormingen van het magnetische veld. Dit leidt

tot beeldvervormingen, signaalhyperintensiteit en signaalverlies in de buurt van het implantaat. In het ergste geval kan dit leiden tot verkeerde diagnose of het missen van klinisch relevante informatie, zoals de detectie van (pseudo-)tumoren, ontstekingen, loslaten en slijtage van het implantaat. Om deze artefacten te voorkomen zijn volledige fasegecodeerde sequenties onderzocht, ondanks de vele malen hogere scantijd.

In **Hoofdstuk 2** werd er een eerste stap gemaakt naar klinisch haalbare scantijden voor fasegecodeerde beeldvorming in de buurt van orthopedische implantaten. Hiervoor werd een 3D fasegecodeerde turbo spin-echo (3D-PE-TSE) sequentie gecombineerd met Compressed Sensing (CS). CS is een iteratief reconstructieschema dat gebruik maakt van redundantie in de MRI methodologie. De combinatie van deze methodes verlaagde de scantijd van 3D-PE-SE een factor 60 waardoor een geometrische onverstoorde *in vivo* dataset gemeten kon worden in minder dan 10 minuten.

In deze experimenten werd een titanium implantaat gebruikt om de artefact reducerende eigenschappen van volledig fasegecodeerde MRI te bestuderen. Ondanks de sterke susceptibiliteitsgradiënten in de buurt van titanium was het mogelijk om geometrisch onvervormde beelden te maken en het signaal in de buurt van het implantaat te detecteren in een enkele meting. Het merendeel van het signaal kon geëxciteerd worden door de radiofrequentie (rf) bandbreedte te maximaliseren (~3 kHz). In het geval van grotere veldinhomogeniteiten, zoals veroorzaakt door kobalt-chroom of roestvrij stalen implantaten, zijn meerdere metingen op verschillende frequenties noodzakelijk om al het signaal te detecteren. De huidige state-of-the-art MRI methodes voor beeldvorming in de buurt van metaal maken gebruik van multispectrale excitatieschema's om geometrische vervormingen, signaalhyperintensiteit en signaalverlies te verminderen. Ondanks sterk verminderde artefacten bij het gebruik van deze technieken blijven fundamentele limitaties bestaan voor het verminderen van artefacten in de buurt van metalen implantaten. In deze regio's zou een multispectrale fasegecodeerde techniek een oplossing kunnen bieden.

In **Hoofdstuk 3** werden multispectrale frequentiegecodeerde 3D-TSE en fasegecodeerde 3D-PE-TSE sequenties geïmplementeerd om prestaties van de beeldvorming te vergelijken (artefacten, scantijd, signaalkarakterisering) voor een groot frequentiebereik van 40 kHz. De methodes werden gevalideerd met een knie-implantaat van kobalt-chroom, een sterk paramagnetisch materiaal dat regelmatig voorkomt in postoperatieve orthopedische beeldvorming. De resultaten lieten zien dat multispectrale 3D-PE-TSE gebruikt kon worden om hyper-intensiteitsartefacten en signaalverlies te voorkomen in de aanwezigheid van extreme susceptibiliteitgradiënten in de buurt van het implantaat, terwijl deze artefacten wel aanwezig waren in multispectrale 3D-TSE beelden. Voor een meting met een +10 kHz rf offset was het mogelijk om signaal in de buurt van het implantaat te meten in ~3.5 minuten met voldoende spatiële resolutie, dankzij een combinatie van een kleiner meetvolume (reduced field of view imaging) en iteratieve reconstructietechnieken (CS). De resultaten in dit hoofdstuk lieten zien dat het mogelijk is om artefactvrije MRI beelden te verkrijgen in de

149

buurt van orthopedische implantaten met multispectrale 3D-PE-TSE technieken binnen een redelijk tijdsbestek.

In het tweede deel van dit proefschrift werden de unieke temporele en spectrale eigenschappen van fasegecodeerde sequenties gebruikt om MR signaalgedrag te bestuderen. In **Hoofdstuk 4** werd er een pilotstudie uitgevoerd om de mogelijkheden van signaalkarakterisering met fasegecodeerde beeldvorming te onderzoeken. Hiervoor werd een 3D frequentie gecodeerde techniek aangepast naar een 2D fasegecodeerde techniek met een extra dimensie waarin de MR signaalevolutie in de tijd werd gemeten. In plaats van de signaalevolutie te gebruiken om de frequentie inhoud te bestuderen, zoals in spectroscopische onderzoeken, werd het gebruikt om herhaalde verstoringen van het MR signaal in kaart te brengen. De 2D multiple single-point imaging (mSPI) methode werd gebruikt om T_2^* verval, gradiënt geïnduceerde signaalverstoringen en stroom geïnduceerde faseontwikkelingen te detecteren. Mogelijke toepassingsgebieden van deze methode zijn accurate T_2^* mapping, evaluatie van systeemprestaties en het meten van faseveranderingen door externe stimuli, zoals geïnduceerd door transcraniële magnetische stimulatie.

De mogelijkheden voor T_2^* mapping werden verder benut voor signaalkarakterisering van natrium (^{23}Na), dat een belangrijke fysiologische rol speelt in het menselijk lichaam (bijv. het in stand houden van de celintegriteit en het doorgeven van zenuwimpulsen). Hierbij worden veranderende natriumconcentraties en signaalgedrag gebruikt voor vroege detectie van ziekte, zoals een vroeg stadium van osteoartritis en het ontstaan van tumorcellen. Kwantitatieve parameters die bepaald kunnen worden met MRI zijn de natriumconcentratie en bi-exponentiële T_2^* waardes. Deze parameters zijn gerelateerd aan zowel de biologische structuur als de celintegriteit. Helaas is accurate kwantificatie van beide natrium T_2^* waardes erg lastig met conventionele methoden (e.g. multi gradiënt-echo) vanwege de lage gevoeligheid voor natriummetingen en de aanwezigheid van een erg korte T_2^* component (~0.5 - 3.0 ms). Voor accurate T_2^* mapping met frequentiegecodeerde technieken zijn meerdere signaalmiddelingen en meerdere datapunten in de tijd nodig wat de scantijd sterk verhoogd.

In **Hoofdstuk 5** werd een flexibele fasegecodeerde methode onderzocht voor natrium imaging, het bepalen van natriumconcentraties en detectie van bi-exponentieel T_2^* signaalverval. Hiervoor werden conventionele en ultrakorte TE 3D fasegecodeerde methodes geïmplementeerd en geëvalueerd *in vitro* en *in vivo*. Uit de resultaten bleek dat het mogelijk was om het bi-exponentiële signaalgedrag accuraat te karakteriseren *in vivo* waarbij een hogere spatiële resolutie behaald werd dan in eerdere onderzoeken. De gebruikte methodes bleken tijdsefficiënt te zijn in het specifieke geval van natrium relaxatiemetingen, dankzij de voordelige gevoeligheidseigenschappen in combinatie met de sub-milliseconde bemonstering van de signaalcurve.

Naast analyse in het temporele domein kan de frequentie inhoud van het MR signaal gebruikt worden om biologische veranderingen op moleculair niveau te detecteren. In het

veld van MR spectroscopie (MRS) wordt op deze manier informatie verkregen over metabolisme, de biochemische samenstelling van het brein, spierfunctie en andere natuurlijk voorkomende moleculen in het lichaam. Een uitzondering hierop zijn fluor (^{19}F) MRS metingen. Fluor komt niet van nature voor in het lichaam, maar kan geïntroduceerd worden door medicijnen of moleculaire markers. Dit maakt fluor MRS geschikt voor non-invasieve monitoring van medicijnmetabolisme en medicijndistributie in het lichaam. Idealiter zouden deze parameters gebruikt kunnen worden om de effectiviteit van medicijnen te bepalen. Het voornaamste doel van de huidige onderzoekslijn is het reduceren van toxiciteitseffecten bij patiënten die niet op de therapie reageren, waardoor ook de hoge behandelkosten verlaagd kunnen worden. In het huidige stadium is het echter moeilijk om robuuste fluormetingen uit te voeren, vanwege de lage concentraties na medicijninname (mM range) in combinatie met specifieke hardware benodigdheden.

In **Hoofdstuk 6** werd een nieuwe setup gepresenteerd om het metabolisme en de distributie van de chemotherapeutische pro-drug capecitabine te meten in de lever en omliggende organen. In dit hoofdstuk werden drie verbeteringen onderzocht voor *in vivo* capecitabine detectie. Ten eerste werd een hoog veld 7T MR scanner gebruikt om de gevoeligheid van fluordetectie te verhogen. Ten tweede werd een zend-ontvangstspoel met acht elementen gebruikt om het spatiële bereik te vergroten naar de hele lever en omliggende organen. Ten derde werd een dual-band rf puls ontworpen om simultaan capecitabine en zijn afbraakproducten te kunnen detecteren voor metabolismestudies. De beschreven setup was in staat om zowel capecitabine te detecteren in de lever en maag als ook de afbraakproducten in de lever, nieren en milt. Deze bevindingen vergroten de toepasbaarheid van fluordetectie substantieel aangezien voorheen alleen een sub-sectie van de lever bestudeerd kon worden in een enkele meting.

De verschillende hoofdstukken in dit proefschrift laten de brede toepasbaarheid van fasegecodeerde technieken zien in verschillende MRI onderzoeksvelden. Fasegecodeerde MRI technieken blijken een robuust alternatief te zijn voor frequentiegecodeerde methodes in de aanwezigheid van veldinhomogeniteiten (Hoofdstuk 2-3), MR signaalkarakterisering (Hoofdstuk 4-6) en lage MR gevoeligheid (Hoofdstuk 5-6). De toekomstige mogelijkheden van fasegecodeerde MRI sequenties zijn besproken in **Hoofdstuk 7**. De gerapporteerde resultaten in dit proefschrift zijn voornamelijk technisch van aard en vereisen additionele klinische validatie in patiëntpopulaties. Ondanks deze beperking zijn de gerapporteerde resultaten veelbelovend en bruikbaar als basis voor toekomstige studies.

Gebaseerd op de methodes en resultaten in dit proefschrift lijkt fasegecodeerde MRI een levensvatbare strategie te zijn voor geometrische onverstoorde beeldvorming in de buurt van metalen implantaten en signaalkarakterisering van nuclei (^{23}Na, ^{19}F) met een lage MR gevoeligheid.

LIST OF PUBLICATIONS

PAPERS IN INTERNATIONAL JOURNALS

- J.S. van Gorp, P.R. Seevinck, A. Andreychenko, A.J.E. Raaijmakers, P.R. Luijten, M.A. Viergever, M. Koopman, V.O. Boer, D.W.J. Klomp; ^{19}F MRSI of capecitabine in the liver at 7T using broadband transmit-receive antennas and dual-band RF pulses, *NMR in Biomedicine 2015, 28(11):1433-1442*

- J.S. van Gorp, C.J.G. Bakker, J.G. Bouwman, J. Smink, F. Zijlstra, and P.R. Seevinck; Geometrically undistorted MRI in the presence of field inhomogeneities using compressed sensing accelerated broadband 3D phase encoded turbo spin-echo imaging, *Physics in Medicine and Biology 2014, 60(2):615-631*

- C.J.G. Bakker, J.S. van Gorp, J.J. Verwoerd, A.H. Westra, J.G. Bouwman, F. Zijlstra, P.R. Seevinck; Multiple single-point imaging (mSPI) as a tool for capturing and characterizing MR signals and repetitive signal disturbances with high temporal resolution: The MRI scanner as a high-speed camera, *Magnetic Resonance Imaging 2013, 31(7):1037-1043*

- C.J.G. Bakker, H. de Leeuw, G.H. van de Maat, J.S. van Gorp, J.G. Bouwman, P.R. Seevinck; On the utility of spectroscopic imaging as a tool for generating geometrically accurate MR images and parameter maps in the presence of field inhomogeneities and chemical shift effects, *Magnetic Resonance Imaging 2013, 31(1):86-95*

- V.O. Boer, J.C.W. Siero, H. Hoogduin, J.S. van Gorp, P.R. Luijten and D.W.J. Klomp; High-field MRS of the human brain at short TE and TR, *NMR in Biomedicine 2011, 24(9):1081-1088*

MANUSCRIPTS SUBMITTED FOR PUBLICATION

- J.S. van Gorp, R. Nizak, J.G. Bouwman, D.F.B. Saris, P.R. Seevinck; Multispectral 3D phase-encoded turbo spin-echo for imaging near metal: Limitations and possibilities

- J.S. van Gorp, P.W. de Bruin, A.G. Webb, M.A. Viergever, P.R. Seevinck; Bi-exponential transverse relaxation mapping of sodium with high temporal resolution using 3D ultrashort TE spectroscopic imaging at 7T

Conference Abstracts

- J.S. van Gorp, P.W. de Bruin, P.R. Seevinck. Ultrashort TE 3D spectroscopic imaging for high SNR imaging and bi-exponential signal decay characterization of sodium; *International Society for Magnetic Resonance in Medicine, 2016*

- J.S. van Gorp, P.R. Seevinck, A. Andreychenko, A.J.E. Raaijmakers, P.R. Luijten, M. Koopman, V.O. Boer, D.W.J. Klomp; ^{19}F MRSI of capecitabine in the liver using broadband TxRx antennas and dual-frequency excitation pulses at 7T, *International Society for Magnetic Resonance in Medicine, 2015*

- J.S. van Gorp, C.J.G. Bakker, J.G. Bouwman, J. Smink, F. Zijlstra and P.R. Seevinck; Compressed sensing accelerated broadband 3D phase encoded turbo spin-echo imaging for geometrically undistorted imaging in the presence of field inhomogeneities, *International Society for Magnetic Resonance in Medicine, 2015*

- J.S. van Gorp, P.W. de Bruin, and P.R. Seevinck; Time efficient and quantitative sodium imaging at 7T using compressed sensing accelerated FID spectroscopic imaging, *International Society for Magnetic Resonance in Medicine, 2015*

- J.S. van Gorp, C.J.G. Bakker, F. Zijlstra, J. Smink, J.G. Bouwman, P.R. Seevinck; Geometrically undistorted imaging of orthopedic implants using compressed sensing accelerated phase encoded imaging, *International Society for Magnetic Resonance in Medicine, 2014*

- J.S. van Gorp, C.J.G. Bakker, P.R. Seevinck; A hybrid multi-spectral approach for near metal imaging: combining the best of phase and frequency encoding, *International Society for Magnetic Resonance in Medicine, 2014*

- J.S. van Gorp, J.G. Bouwman, C.J.G. Bakker, and P.R. Seevinck; Prospective compressed sensing accelerated spectroscopic imaging for use in geometrically accurate in vivo imaging**,** *International Society for Magnetic Resonance in Medicine Salt lake City and Benelux, 2013*

- J.S. van Gorp, S.P.M. Crijns, J.G. Bouwman, B.W. Raaymakers, C.J.G. Bakker, P.R. Seevinck; Compressed sensing accelerated spectroscopic imaging to obtain geometrically accurate water-fat images and field maps for use in MR-guided interventions, *International Society for Magnetic Resonance in Medicine, 2012*

- J.S. van Gorp, J.G. Bouwman, C.J.G. Bakker, and P.R. Seevinck; Towards compressed sensing accelerated geometrically undistorted Single Point Images under 10 seconds. *International Society for Magnetic Resonance in Medicine, 2012*
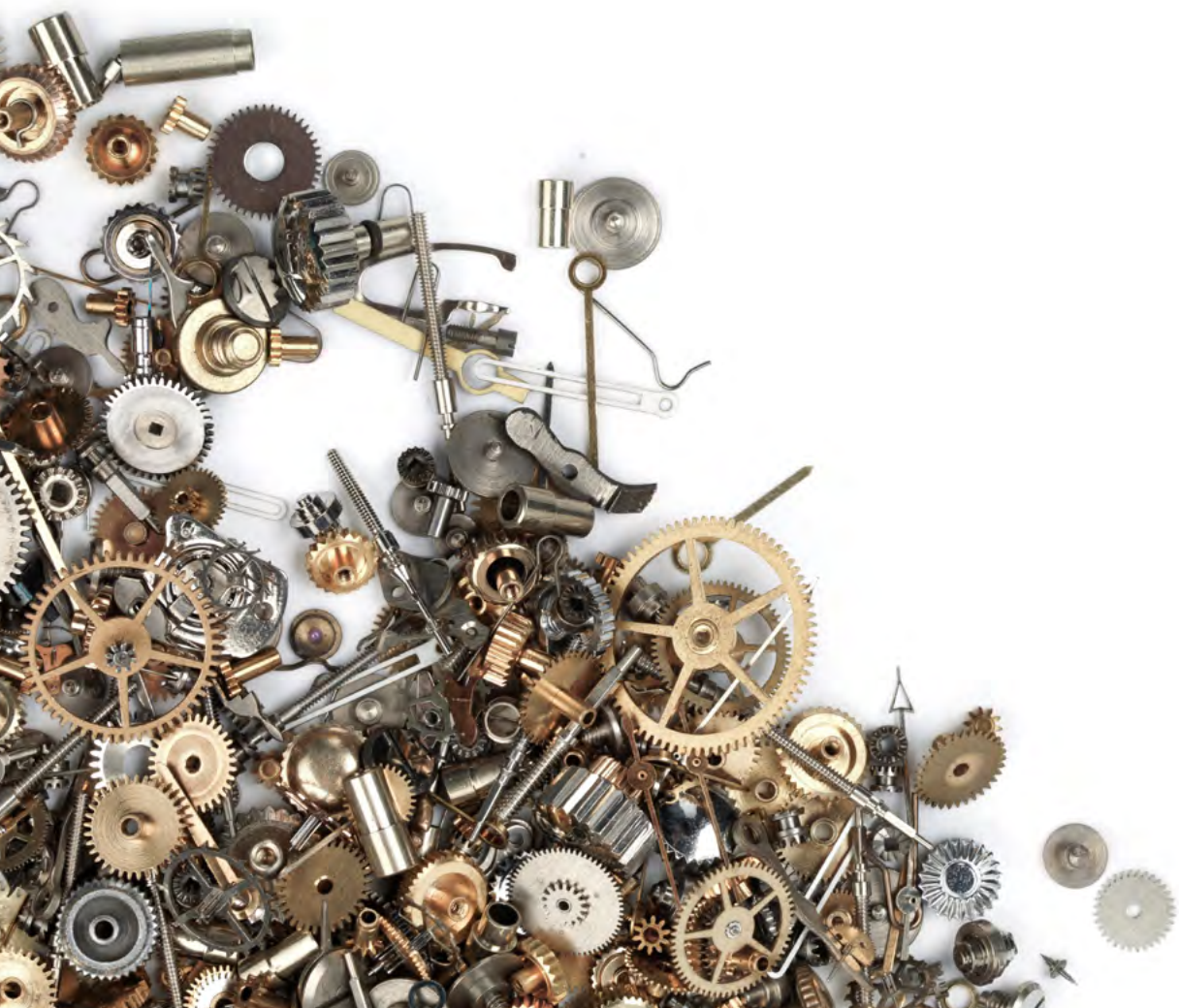
DANKWOORD

No matter what accomplishments you make, somebody helped you.

ALTHEA GIBSON

Het tot stand komen van dit proefschrift was niet mogelijk geweest zonder alle support van de mensen om mij heen, zowel binnen het UMC Utrecht als daarbuiten. Ik zie dit werk dan ook als een gezamenlijk behaald resultaat en wil al mijn coauteurs, collega's en in het bijzonder mijn begeleiders bedanken voor de input, positieve afleiding, vele inhoudelijke discussies en het wikken en wegen van elk geschreven woord.

Peter, je enthousiasme voor het vakgebied van MRI werkt aanstekelijk en kwam altijd goed van pas om een tandje bij te schakelen wanneer de voortgang haperde. Het is mooi om te zien dat we onze eigen weg hebben weten te vinden binnen het kader van dit project. Je was altijd beschikbaar als de situatie daarom vroeg en de ontspannen en persoonlijke manier van werken was super. Ik zal onze discussies tot in de late uurtjes met een glimlach blijven herinneren. Veel succes met het uitbouwen van je onderzoekslijn en daarnaast natuurlijk alle goeds voor de dames thuis.

Chris, bedankt voor alle inzet in de jaren dat je mijn begeleider was en daarna. Ik vond het erg prettig om met je te mogen werken! Je interesse en kennis op het gebied van MRI zijn onomstreden, maar desondanks blijf je altijd de bescheidenheid zelve. Je inzicht in tekstuele opbouw en argumentatie helpt me dagelijks om kritisch naar mijn eigen teksten te blijven kijken. Hopelijk ben je met volle teugen aan het genieten van je pensioen.

Max, erg bedankt voor de goede sfeer binnen het ISI en de vinger aan de pols met de voortgang van het promotietraject. Ondanks de grootte van de groep weet je toch altijd het overzicht te bewaren en bij te sturen waar nodig. Ik waardeer je betrokkenheid bij je promovendi en ben dankbaar dat ik bij het ISI heb mogen promoveren. Hopelijk kun je een mooie vorm vinden om nog lang betrokken te blijven bij het veld van de medische beeldvorming.

Geachte leden van de leescommissie, bedankt voor het beoordelen van mijn proefschrift.

Dennis, Vincent en Wybe, ik heb de samenwerking op het gebied van fluorspectroscopie als erg prettig ervaren. Het was een eer om deel uit te mogen maken van het spectroteam. Ik ben blij dat het fluorproject een mooi vervolg kan krijgen in de toekomst.

Paul, ik heb met veel plezier in Leiden aan het natriumproject gewerkt. De ontspannen sfeer, je creatieve natriummetingen en experimentele know-how hebben een mooie samenwerking opgeleverd. Hopelijk krijgt deze nog een mooi vervolg de komende jaren.

Razmara, bedankt voor alle orthopedische materialen, klinische vraagstellingen en gezellige scansessies. Hopelijk leiden onze eerste bevindingen uiteindelijk tot klinisch toepasbare producten.

Waarde collega's en mede-promovendi, promoveren is natuurlijk een serieuze aangelegenheid met vele mores, tradities en eigenaardigheden. Gelukkig kon ik dit proces met al zijn ups en downs uitvoerig bespreken tijdens vele diners, borrels, conferenties,

sinterklaasvieringen, Ardennen weekenden, emergency meetings in de koffiekamer, of met een stuk taart na een gepubliceerd artikel. Hier zitten vele gedenkwaardige momenten bij waarvoor ik iedereen bij het ISI en in het UMC Utrecht wil bedanken, waaronder een aantal personen in het bijzonder:

Mijn paranimfen, Job en Miekee. Job, je interesse in andere personen en het willen creëren van een goede sfeer op de afdeling was altijd erg welkom. Het was mooi om met je te brainstormen over nieuwe futuristische ideeën, die zo nu en dan te herleiden waren tot het werk van wetenschappers die hun tijd blijkbaar ver vooruit waren. Daarnaast wil ik je natuurlijk ook nog heel erg bedanken voor al je hulp met Matlab, data processing, wiskundige onderbouwingen en de mooie borrels buiten werktijd! Miekee, heel erg bedankt voor alle gezelligheid en goede gesprekken gedurende het promotietraject. Ik waardeer je eerlijkheid en je vrolijke expressieve karakter, het werkt erg aanstekelijk! Ik voel me vereerd dat jullie aan mijn zijde willen staan tijdens de verdediging!

Yinghe, thank you for being such a nice and understanding roommate. It must be hard to work with two loud Dutch guys in one room. Thank you for always being so helpful whenever I was stressing out about something minor. Hopefully you'll have less distractions now so you can finish your own dissertation.

Frank, bedankt voor je hulp met het bedenken van gerichte oplossingen als ik weer eens in de knoop zat met het maken van de benodigde patches. Succes met de laatste loodjes!

ISMRM conferentiegenoten, het was elk jaar een hoogtepunt om met jullie uitstapjes over de hele wereld te mogen maken. Naast de inhoudelijke discussies heb ik erg genoten van de vele netwerkborrels tot in de late uurtjes en de early morning sessions die daarop volgden.

Naast de bijdrage van alle collega's zijn er natuurlijk nog vele anderen die een belangrijke rol spelen in mijn leven en daardoor ook bij het tot stand komen van dit proefschrift. Dankzij hen heb ik voldoende ontspanning, relativering en focus kunnen houden om dit proefschrift tot een goed einde te brengen.

Lieve pap, mam en Wil, ik vind het geweldig dat jullie mij altijd steunen bij mijn keuzes in het leven. Tot de dag van vandaag helpt mij dit om kansen te signaleren en ten volle te benutten. Het is een geweldige luxe om een veilige basis te hebben, waardoor ik altijd de rust en ruimte heb om weloverwogen beslissingen te maken. Dank jullie wel voor alle vrijheid en mogelijkheden, dit proefschrift is voor jullie.

En als laatste, maar zeker niet de minste: Gerline, lief, we did it! Dit proefschrift was er niet gekomen als jij er niet was geweest om mij te steunen gedurende het hele traject. Naast de emotionele ondersteuning heb je ook erg veel bijgedragen als mantelzorger, proefpersoon en testlezer. Je bent geweldig! Ik kan mij geen groter geluk wensen dan samen met jou het leven te mogen beleven.

CURRICULUM VITAE

Jetse Sigiward van Gorp was born in Eindhoven, the Netherlands on August 18th 1985. In 2003 he finished his high school education at Rythovius College in Eersel followed by the Molecular Life Sciences program at Wageningen University. In 2009 he received his Master of Science degree with a specialization in physical chemistry. During his master thesis work he got acquainted with MRI and spectroscopy at the 7T group in the University Medical Center Utrecht and continued working in the field of MR spectroscopy during an internship in Yale University, New Haven, USA. After obtaining his master degree he started as a Life Sciences and Health technology equity analyst at Kempen & Co in Amsterdam before returning to the University Medical Center Utrecht to work on a PhD project in the MR physics group under the supervision of dr. ir. P.R. Seevinck, dr. ir. C.J.G. Bakker and prof. dr. ir. M.A. Viergever. The results of this work are described in this thesis.